North Carolina Agricultural and Technical State University
Aggie Digital Collections and Scholarship

Dissertations | Electronic Theses and Dissertations

2014

Magnetic Properties And Structure Of Iron-Nickel Nanoparticles And Thin Films Synthesized By Pulsed Laser Deposition

Sally Ahmed Ibrahim
North Carolina Agricultural and Technical State University

Follow this and additional works at: https://digital.library.ncat.edu/dissertations

Recommended Citation

Ibrahim, Sally Ahmed, "Magnetic Properties And Structure Of Iron-Nickel Nanoparticles And Thin Films Synthesized By Pulsed Laser Deposition" (2014). *Dissertations*. 78.
https://digital.library.ncat.edu/dissertations/78

This Dissertation is brought to you for free and open access by the Electronic Theses and Dissertations at Aggie Digital Collections and Scholarship. It has been accepted for inclusion in Dissertations by an authorized administrator of Aggie Digital Collections and Scholarship. For more information, please contact iyanna@ncat.edu.

Magnetic Properties and Structure of Iron-Nickel Nanoparticles and Thin Films Synthesized by Pulsed Laser Deposition

Sally Ahmed Ibrahim

North Carolina A&T State University

A dissertation submitted to the graduate faculty

in partial fulfillment of the requirements for the degree of

DOCTOR OF PHILOSOPHY

Department: Mechanical Engineering

Major: Mechanical Engineering

Major Professor: Dr. Dhananjay Kumar

Greensboro, North Carolina

2014

The Graduate School
North Carolina Agricultural and Technical State University
This is to certify that the Doctoral Dissertation of

Sally Ahmed Ibrahim

has met the dissertation requirements of
North Carolina Agricultural and Technical State University

Greensboro, North Carolina
2014

Approved by:

Dr. Dhananjay Kumar
Major Professor

Dr. Abebe Kebede
Committee Member

Dr. Trisha Sain
Committee Member

Dr. Kunigal Shivakumar
Committee Member

Dr. Samuel Owusu-Ofori
Department Chair

Dr. Mufeed Basti
Committee Member

Dr. Sanjiv Sarin
Dean, The Graduate School

© Copyright by

Sally Ahmed Ibrahim

2014

Biographical Sketch

Sally Ahmed Ibrahim was born in Torrance, California to Ahmed Mohammed Elhassan Ibrahim and Sittana Babiker Abd Elraheem. She received her Bachelor of Science in Mechanical Engineering from University of Khartoum in Sudan in 2003. Her senior project was presented in the Common Market for Eastern and Southern Africa (COMESA). She worked as a teaching assistant for the Mechanical Engineering Department at University of Khartoum.

Ms. Ibrahim received her Master of Science degree in Mechanical Engineering from North Carolina Agricultural and Technical State University in 2008. In fall of 2008 she joined the Mechanical Engineering doctoral program at North Carolina Agricultural and Technical State University.

She received a 4.0 Certificate of Academic Achievement North Carolina Agricultural and Technical State University. She was also awarded Title III fellowship in 2008. While pursuing her degree Ms. Ibrahim worked as a teaching assistant in Dynamics, Strength of Materials and Material Sciences courses. She also worked as a research associate for the ERC in summer 2013 and summer 2014. Ms. Ibrahim has presented her research at the 2014 MRS Spring Meeting & Exhibit.

Ms. Ibrahim's dissertation, *Magnetic Properties and Structure of Iron-Nickel Nanoparticles and Thin Films Synthesized by Pulsed Laser Deposition,* was supervised by Dr. Dhananjay Kumar.

Dedication

I dedicate my dissertation to my husband Eisar who supported me along the way, and to my son Omer who is my greatest motivation. I also dedicate this work to my brothers, my family and friends and to the souls of my parents *(may Allah give them an easy and pleasant journey and shower blessings on their graves. Ameen)*

Acknowledgments

First of all, I would like to express my deepest appreciation to my committee chair Dr. Dhananjay Kumar for his guidance and his patience; he continually conveyed a spirit of adventure in regard to research and excitement in regard to teaching. Without his guidance and persistent help this dissertation would not have been possible.

I would like to thank my committee members Dr. Abebe Kebede for his invaluable support and contribution, Dr. Trisha Sain, Dr. Kunigal Shivakumar, and Dr. Mufeed Basti for the guidance and support I received from them throughout my graduate studies.

I sincerely thank Dr. Sergey Yarmolenko, for his technical input and contribution to the work, Dr. Zhigang Xu for training me and for his expert. I also wish to extend my heartfelt gratitude to my colleagues Dr. Kwadwo Mensah-Darkwa, Dr. Svitlana Fialkova, Dr. Suhaila Abdalla, Eric Craven, Hiba Ahmed, Dr. Ruben Kotoka, Seyram Gbordzoe, Dr. Yongjun Chen, Mr. Eric Norman and Nana K. Yamoah for their encouragement, help and support.
I sincerely thank Dr. Samuel Owusu-Ofori and the Mechanical Engineering department faculty and staff for their valuable guidance and help. I also appreciate the ERC staff for their technical support.

This work was financially supported by the National Science Foundation Engineering Research Center for Revolutionizing Metallic Biomaterials (ERC-RMB). This support is greatly appreciated.

Finally I am grateful to my husband, and son for your love and sacrifice; family and friends for your support and encouragement.

Table of Contents

List of Figures

List of Tables

List of Symbols

AFM	Atomic Force Microscopy
AMLD	Alternate Monatomic Layer Deposition
APB	Anti-Phase Boundary Energy
Au	Gold
B	Boron
BD	Blu-ray
BN	Boron Nitride
B_s	Saturation Flux Density
CD	Compact Disc
Co	Cobalt
Cr	Chromium
Cu	Copper
DVD	Digital Versatile Disc
EDX	Energy Dispersive X-ray
Fe	Iron
Ga	Gallium
HDD	Hard Disk Drive
H_c	Coercive Force
KrF	Krypton Fluoride
La	Lanthanum
M_r	Remanent Magnetization
M_s	Saturation Magnetization

Ni	Nickel
Oe	Oersted
Pd	Palladium
PLD	Pulsed Laser Deposition
PPMS	Physical Properties Measurement Systems
Pt	Platinum
RHEED	Reflection High Energy Electron Diffraction
RE-TM	Rare Earth Transmission Metals
SEM	Scanning Electron Microscopy
Sm	Samarium
SQUID	Superconducting Quantum Interference Device
Sr	Strontium
SUL	Soft Under Layer
Ta	Tantalum
T_B	Blocking Temperature
T_c	Curie Temperature
TEM	Transmission Electron Microscopy
Ti	Titanium
XRD	X-ray Diffraction
Y	Yttrium

Abstract

The study of new combinations of self-assembled magnetic materials in nanoparticle and thin film form is becoming increasingly important with the continuous shrinking of data storage device size with higher densities. The work presented in this dissertation is focused towards synthesis, structural characterizations, and magnetic properties of an $L1_0$ iron-nickel ($Fe_{50}Ni_{50}$) phase that has a potential to replace noble metals based $L1_0$ magnetic materials, such as Ni-Pt, Fe-Pt, being used as recording media. $Fe_{50}Ni_{50}$ was fabricated using a pulsed laser disposition (PLD) method under various deposition conditions, the most important among which was the substrate temperature. The substrate temperature was varied all the way from liquid nitrogen boiling temperature of 77K (-196 ºC) to high temperatures up to 600 ºC. In order to understand and optimize the formation of $L1_0$ phase, the PLD method was used to fabricate FeNi in three distinct ways: (i) FeNi films were prepared using a FeNi composite (alloy) target, (ii) FeNi films were fabricated in a multilayered structure using sequential ablation of Fe and Ni targets, and (iii) FeNi thin films were fabricated in alumina (Al_2O_3)/FeNi/Al_2O_3 sandwich structures.

To promote the stabilization of $L1_0$ FeNi phase, a thin film layer of gold catalyst was deposited prior to the deposition of FeNi films. FeNi films deposited in the presence or absence of gold catalyst were annealed at 600°C for 1 hour to study effect of annealing that has been found to bring about significant alterations in structural and magnetic properties. The substrate materials such as silicon and sapphire were also found to play a significant role in the microstructural and magnetic properties of the FeNi films. The FeNi samples deposited at liquid nitrogen temperature were found to be completely glassy (amorphous), and they exhibited a perfect superparamagnetic behavior, making them good candidates for magnetic biomedical devices.

CHAPTER 1

Introduction

In this research Iron-Nickel thin films fabricated by pulsed laser deposition (PLD) method have been investigated for their possible use in data storage devices. Intensive research have been conducted to increase storage density to produce smaller efficient data storage devices and to reduce the price per storage unit in $/G byte [1]. In this chapter, an overview of data storage, the $L1_0$ Iron –Nickel structure, research objectives and approach, as well as a brief outline of the dissertation chapters are presented.

1.1 Overview and Development of Data Storage Devices

Date storage devices are used to record and process information [2]. A recording medium is the material that is used to store data in, such as the surface of a compact disc (CD). Data storage can be classified into primary, secondary, tertiary and off-line storage. The primary storage is the main memory in a computer known as RAM, ROM and cache. The secondary storage is the hard disk which is considered the largest device in the computer and it can be either internal or external. Tertiary storage is a computer storage system used to archive data that is not accessed frequently such as magnetic tapes, and optical discs (Blu-ray (BD), compact disc (CD), and digital versatile disc (DVD)). Off-line storage is a removable device that is controlled and connected by a human user, such as floppy disks, USB flash drive and memory cards.

Data storage devices may also be categorized depending on their memory volatility, accessibility to reading and writing data, mutability of the storage and last the location, file and content addressability. Magnetic storage devices include floppy disks, hard disks, disk cartridges and magnetic tapes. The recording medium contains magnetic particles that can be polarized by

applying a magnetic charge in two different directions (which represent bits 1 (on) or 0(off)). The magnetic charges are created by electromagnets in the read and write heads.

The first experiments on magnetism were conducted by William Gilbert (1540-1603). In 1820 Han Christian Oersted (1777-1820) discovered that an electric current produces a magnetic field. These discoveries and many more opened the door to industrial revolution and development of a large number of applications. Valdemar Poulsen (1869-1942) invented the telegraphone in 1898. Then he invented an oscillator that replaced the on-off transmitters in 1910. Germans took the lead in production and development of magnetic recording in the 1920s. The German magnetophone was invented in 1928. Audio recorders surfaced in 1948 [3]. The first magnetic hard drive was manufactured by IBM in 1956. This was followed by a series of interesting techniques [4]. In 1970 again IBM introduced the diskette for data storage. Major work have been conducted to improve data storage devices and to increase its areal density (bits/area). A dead end is now facing this development as physical limitations of nano-magnetism has been reached.

1.2 Materials in Data Storage and Relevance of $L1_0$ Structures

The disk drive consists of the read head, write head and the recording media. Each component requires the magnetic material they are made of to have specific magnetic properties. For example the write of HDD are made of iron-cobalt (FeCo) alloys because they have very high saturation flux density B_s. Audio tape recorders write heads are made of the Permalloy (nickel-iron (NiFe) alloy with 80% nickel (Ni) composition); which have high specific permeability and B_s up to 0.8T [5]. Magnetic materials used for fabricating recording media are the cobalt-chromium-platinum (Co-Cr-Pt) alloys. Ruthenium (Ru) (a non-magnetic material) is used as an intermediate layer between the soft under layer (SUL) and the recording layer to break

the magnetic coupling between layers and to induce perpendicular orientation of the magnetic alloy. Fabrication techniques of data storage components are mainly physical, top-down processes such as vacuum-deposition and gas –phase evaporation processes and recently solution-phase chemical synthesis.

For recording media stability depends on the amount of the anisotropy energy E_A needed to demagnetize the material; the higher energy the more stable the media. Magnetic anisotropy depends on the effective anisotropy constant K and also its positively proportional to coercivity. Since coercivity is much easier to evaluate for a specific material than the effective anisotropy constant, coercivity is the main parameter to consider when investigating possible candidates for recording media.

Recent studies recommend materials with $L1_0$ structure for recording media because of their large magneto-crystalline anisotropy energy and high coercivity values. Extensive research is now been conducted to improve the synthesis of $L1_0$-ordered FePt alloys [6-10]. In this work we are investigating the fabrication of $L1_0$ –ordered FeNi thin films using PLD. In this section basic information about the $L1_0$ structure is provided.

The $L1_0$ structure (shown in Figure 1.1) is an alloy crystal structure that relate to the FCC structure; i.e. a derivative structure (ordered variants) of the parent structure [11]. The parent cubic structure FCC is distorted in the $L1_0$ ordered alloys which are tetragonal in symmetry because of the different atom sizes. L is a Strukturbericht symbol given for an alloy. L1 illustrates that the alloy structure is derived from the first of the elemental structures (A1).

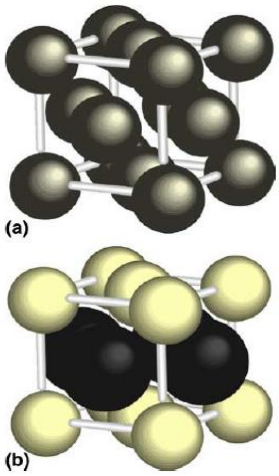

Figure 1.1. a) The parent FCC atomic structure, b) The $L1_0$ atomic structure of an alloy

$L1_0$ is a tetragonal structure and it is found in ordered AB alloys (binary alloys); A and B atoms order on alternate (0, 0, 1) planes. The A atoms occupy (0,0,0) and (½, ½, 0) positions in the crystal, whereas the Ba atoms occupy (0, ½, ½) [12]. Alloys known to form the $L1_0$ structure are CuAu, FePt, FePd and CuTi. $L1_0$ FeNi was only found naturally in meteorites. The $L1_0$ structure might also be noted using Pearson symbols as tP4 (P stands for primitive, t for tetragonal, etc.). The space group is P4/mmm.

In $L1_0$ structures the atoms have eight opposite near neighbors and 4 similar near neighbors and 6 next-near neighbors. The change from disordered FCC to ordered $L1_0$ produces translational domains and orientational domains as shown in Figures 1.2 and 1.3. The transformation from paramagnetic to ferromagnetic produces the magnetic domains illustrated in Figure 1.4.

Translational domains in Figure 1.2 show the atomic ordering that can take place in $L1_0$ structure. The energy between the two phases is called anti-phase boundary (APB) energy. Only transmission electron microscopy (TEM) can show these translational domains.

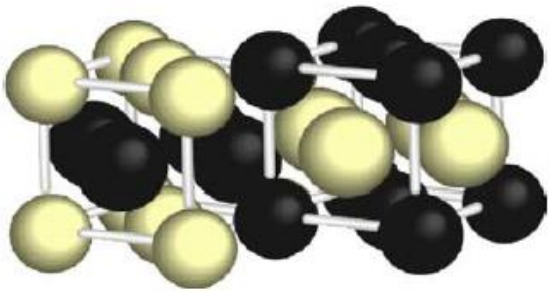

Figure 1.2. Atom orientation in translational domains

Orientational domains as shown in Figure 1.3 are caused by the decrease in symmetry during ordering. Three variants or structural domains can be formed and each variant have two translational domains; i.e. six domains can be formed. It is important to note that the interface also have higher energy between these domains.

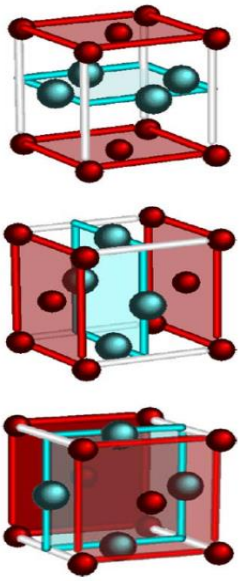

Figure 1.3. The three possible orientational domains in $L1_0$ structures

Ferromagnetic domains shown in Figure 1.4 result from symmetry breaking due to magnetic ordering when an external field is applied. This will be discussed in detail in Chapter 2. For the $L1_0$ structure magnetic phases, the magnetization vector is along [001] axis of the crystal. The magnetization can be directed along [001] and [00-1] directions. Embedding a gold catalyst

in some of the experiments in this work was done based on this characteristic of the $L1_0$ structure. The two magnetic domains along with the translational and orientational domains form 12 possible different domains. It is also important to note that $L1_0$ structure can be created from a high temperature disordered FCC structure. More of the magnetic behavior of this structure will be studied in Chapter 2.

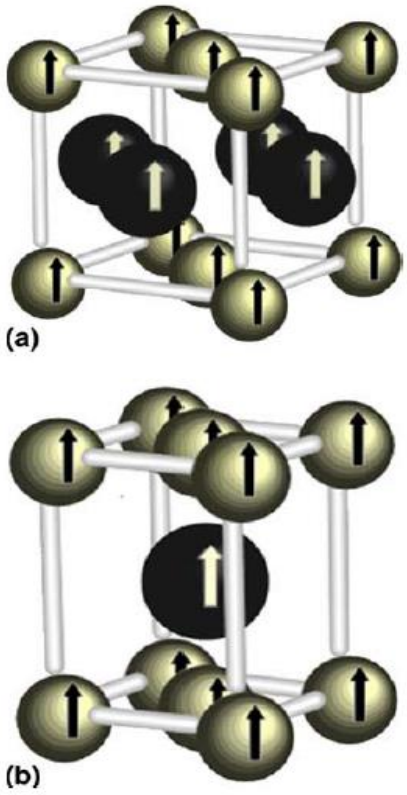

Figure 1.4. One of the two possible magnetic domains in 4 and 2 atoms $L1_0$ structure

1.3 Research Justification

The recording media in data storage devices are usually made of combinations of noble materials (such as Platinum (Pt)) and Iron. The industrial market is demanded to deliver cheaper miniaturized technologies everyday but physical limitations for example due to grain size reduction to increase the areal density is a problem. As a result, researchers are working on new technologies to replace the longitudinal recording by perpendicular recording. $L1_0$ ordered FeNi

is one solution to produce more affordable devices. $L1_0$ ordered alloys are known to have high magnetic anisotropy which is a fundamental property of materials used in high density magnetic storage devices.

1.4 Research Objective and Approach

The goal of this research is to employ the PLD technique to fabricate $L1_0$ FeNi thin films on Silicon substrates for data storage devices. The $L1_0$ structure of the FeNi alloy will enhance its magnetic properties and transform it from a soft magnetic material to a hard magnetic material. In this work, magnetic properties of thin films deposited at low temperatures (near liquid N_2 temperature) are investigated since it has not been reported in literature. The approach followed to achieve these objectives is as follows:

- Optimize PLD parameters such as deposition temperatures and repetition rate to synthesize the FeNi thin films deposited from $Fe_{50}Ni_{50}$ target and multilayer thin films from Fe and Ni targets.
- Employ the multi-target characteristics of PLD to imbed gold nanoparticles to promote the L10 structure formation.
- Fabricate (Al_2O_3 –FeNi) multilayers to study the influence of the AFM-FM coupling on magnetic properties of FeNi thin films.
- Analyze and characterize the structural and magnetic properties of the FeNi thin films developed by PLD under different conditions.

1.5 Dissertation Organization

This dissertation is divided into seven chapters. Chapter 1 is an introduction to the research subject. It also outlines the research objectives and the approach to achieve them. A brief introduction to magnetic data storage devices and $L1_0$ ordered structures is included.

Chapter 2 is devoted to understanding some of the basic concepts of magnetism related to data storage devices and applications of magnetic materials. Types of magnetism are discussed briefly. The material under investigation FeNi is considered a soft magnetic material; the goal of this work is to fabricate the $L1_0$ structure of this material which is a hard magnetic material. The difference between these magnetic material classifications is reviewed. The chapter also covers the literature published in the field of magnetic materials and data storage devices in general. The recent advances in fabricating $L1_0$ FePt and $L1_0$ FeNi will also be addressed.

Chapter 3 describes the experimental procedures employed in this dissertation work. This chapter starts with a description of deposition processes. Then it summarizes the Laser and PLD history, the PLD operating theory, and a brief discussion of the nucleation and growth modes is also incorporated. The chapter also describes the characterization methods (PPMS, XRD, AFM and SEM) used to analyze the samples. The experimental parameters of the fabricating technique along with the analyzing processes mentioned above are listed. Results obtained and discussions of those results are presented in Chapter 4, Chapter 5, and Chapter 6. More specifically, Chapter 4 presents and discusses in detail the results and data collected from the FeNi films prepared from FeNi alloy (composite) target. Chapter 5 discusses the influence of depositing a gold layer under FeNi thin films to catalyze uniform small grains. The effect of post annealing the FeNi thin films on magnetic properties is studied in Chapter 6. Chapter 7 reviews the dissertation and summarizes the main findings. A proposal for future work is also considered.

CHAPTER 2

Basics of Magnetism and Literature Reviews

The main objective of this chapter is to explore the magnetic properties of materials used in recording media. The chapter briefly reviews magnetism and some of the important concepts and terms associated with it. The way materials exhibit attraction and repulsion between them is called magnetism [13]. Some of the known magnetic materials are Iron, some steels, and the naturally occurring mineral such as lodestone (Fe_3O_4).

2.1 Applications of Magnetic Materials

Some of the general applications of magnetic materials are electrical power generators and transformers, electrical motors, radio, television, telephones, computers, and components of sound and video reproduction systems. Magnetic materials have been used in magnetic recording for a long time; also they have been used as sensors in computers, airplanes, automobiles, and factory machines.

Magnetic recording is the common technology for the storage of electronic information, since audio tapes, VCRs, disk storage media, credits cards, etc. are of great importance. Magnetic disks serve as secondary memory for their capacity of storing large amounts of information at low cost. Computer bytes, sound or visual images can be recorded on very small segments of the magnetic storage medium, tape or disk using an inductive read-write head by an electrical signal within the head coil which generates a magnetic field across the gap in the magnetic core for writing. This field then magnetizes a very small area of the disk, and when the field is removed the magnetization stays and the signal is stored. For reading, a voltage is induced by the change in field as the tape passes by the head coil gap and then this will be amplified and transformed back into its original form.

Also magnetoresistive heads which have higher sensitivities and higher data transfer rates read when the electrical resistance of the magnetoresistive thin film element is changed due to magnetic field changes when the tape passes by the read head. There are two types of magnetic media: particulate and thin film. Particulate: are made of very small needle like acicular particles which are attached to a polymeric film in magnetic tapes or to a metal or polymer disk. Examples are γ-Fe_2O_3 ferrite or CrO_2. The storage density is of the order ($1X\ 10^8$ bit/in^2; i.e.$1.5\ X\ 10^5$ bit/mm^2). B_s range from 0.4 to 0.6 tesla. Thin film consists of a multilayer structure and is employed on rigid disk drives. Examples are CoPtCr or CoCrTa alloy with thicknesses in the range 10-50nm. Substrates are usually pure chromium or a chromium alloy. The storage densities are $5\ X\ 10^{10}$ bit/in^2 ($8\ X\ 10^7$ bit/mm^2). B_s range from *0.6 to1.2 tesla*. Coercivity desired for data storage devices range from *(2000 to 3000 Oe).* The thin film is polycrystalline with an average grain size in the range 10-30 nm and each grain is a single magnetic domain. It is important for the thin film grains to be uniform in shape and size. The hysteresis loop for magnetic storage media should be large and square to ensure the storage and magnetization reversal should be over a narrow range of applied field strengths.

Magnetic sensors are preferred because of their reliability and ability to provide maintenance free technology. Examples of magnetic sensors are SQUID, Hall-effect, anisotropic magnetoresistance, giant magnetoresistance, magnetic tunnel junctions, giant magnetoimpedence and microelectromechanical systems based sensors [14]. Magnetic sensors are energy conversion devices that transform input mechanical energy such as position or velocity via magnetic field energy into an electrical signal. This electric signal is an induced voltage with low current. Magnetic sensors usually detect very small amounts of energy. Sensors are used in several applications such as proximity sensors to detect presence and location of objects as in factory

automation; also in microphones to sense air motion; again in linear variable- differential transformers to detect object position; as velocity sensors for antilock brakes and stability control in automobiles.

Magnetic actuators are also an important application of magnetic materials; they are considered energy conversion devices since they convert input electrical energy in a form of voltage and current into magnetic energy which creates a magnetic force that produces limited mechanical motion.

Magnetic actuators are used in: electrohydraulic valves in airplanes, tractors, robots, automobiles and other mobile or stationary equipment; also in fuel injectors in automobiles engines, trucks and locomotives; for biomedical prosthesis devices for artificial hearts, limbs, ears, and other organs; as head positioners for computer disk drives and for loudspeakers; as well as contactors, circuit breakers and relays to control electric motors; and switchgear and relays for electric power transmission and distribution. [15]. Magnetic materials are also used for secondary storage applications such as hard drives, CDs, DVDs, and USB flash drives, which hold data and information that, can be loaded into the RAM when needed. Data Storage devices are reliable, convenient, provide more space and is a better economic choice.

2.2 Basic Magnetic Concepts

Magnetic Fields: is the magnetic force produced by the movement of electrically charged particles

Magnetic Dipoles: are the north and the south poles of a small bar magnet, and the force of a magnetic field will produce a torque that orient the dipoles with the field.

Magnetic Field Vectors: are characterized by magnitude and direction in space.

The magnetic field strength (H): is the externally applied magnetic field. *H* units are ampere-turns per meter or ampere per meter. A field of unit strength has an intensity of one oersted (Oe)[16]. For a magnetic field generated using a cylindrical coil consisting of *N* closely spaced turns, with length *L* and a current of magnitude *I*, then

$$H = \frac{NI}{L} \qquad (2.1)$$

The magnetic induction or magnetic flux density (B): is the magnitude of the internal field strength in a substance that is exposed to an *H* field. The *B* units are teslas or webers per square meter (Wb/m^2). The relation between magnetic field strength and flux density is

$$B = \mu H \qquad (2.2)$$

μ is the permeability and it is a property of the medium with flux density *B* and through which an external field is applied. SI. units of permeability are webers per ampere-meter (Wb/A-m) or henries per meter (H/m). B_0 is the vacuum flux density and μ_0 is the permeability of a vacuum which is a universal constant of $4\pi \times 10^{-7}$ (1.257×10^{-6}) H/m. For vacuum:

$$B_0 = \mu_0 H \qquad (2.3)$$

2.3 Parameters that Describes Magnetic Properties of Solids

Permeability or relative permeability measures the magnetization of the material or the ability of an external field *H* to produce field induction *B*. Magnetization can also be described as the vector sum all magnetic moments. The relative permeability μ_r (unit less) as expressed in equation 2.4, is the ratio of permeability in a material to the permeability in a vacuum. The magnetization of the solid *M* is described in equation 2.5

$$\mu_r = \frac{\mu}{\mu_0} \qquad (2.4)$$

$$B = \mu_0 H + \mu_0 M \tag{2.5}$$

$$M = \chi_m H \tag{2.6}$$

Emu is the electromagnetic unit of magnetic moment (magnetization) which is equivalent to erg/oersted. χ_m is the magnetic susceptibility (unit less) and its relation to relative permeability as shown in equation 2.7

$$\chi_m = \mu_r - 1 \tag{2.7}$$

2.4 Origins of Magnetic Moments

Magnetic moment of an electron in an atom has two sources (demonstrated in Figure 2.1): The orbital motion of the electron around the nucleus and the electron spin around an axis. The spin magnetic moment of an electron is $\pm \mu_B$; where μ_B is the Bohr magneton which is equal to 9.27 x 10^{-24} A-m^2. The moments due to orbital motion around nucleus are typically very small compared to the electron spin and are thus neglected in reference to the magnetization of materials [17]. The moments due to orbital motion play a much important role in nuclear magnetic resonance (NMR) and magnetic resonance imaging (MRI) [17].

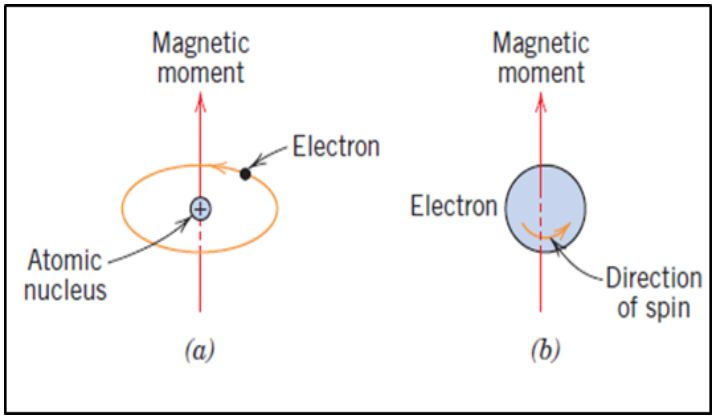

Figure 2.1. Origin of magnetic moment [13]

2.5 Types of Magnetism

Diamagnetism: shown in Figure 2.2; is a temporary weak form of magnetism that exists only when an external field is applied. The change in the orbital motion of electrons prompts the diamagnetism. The magnetic moment in a diamagnetic material is significantly small and opposite to the direction of the applied field. Materials such as Copper, Gold, Silver, Aluminum oxide are examples of Diamagnetism.

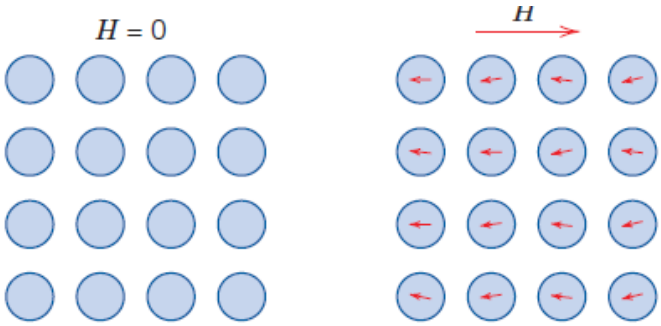

Figure 2.2. A schematic illustrating the influence of applying a magnetic field on the direction of the atomic dipoles in a diamagnetic material [13].

Paramagnetism: shown in Figure 2.3; is the magnetic state of some solid materials with atoms that have permanent dipole moment because of the partial cancellation of electron spin and/or orbital magnetic moments. The orientation of these magnetic moments is random so when they align by rotation in the presence of a magnetic field paramagnetism occurs. Materials such as Aluminum, Chromium, Sodium and titanium are examples of paramagnetism.

Ferromagnetism: This phenomenon (shown in Figure 2.4) occurs in materials that have very large permanent magnetic moment without the presence of an external field. The magnetic moment results from electron spin magnetic moments and uncancelled electron spins due to the electron configuration. Ferromagnetic materials has unpaired electrons, but these electrons have the tendency to align themselves parallel to each other to maintain a lowered energy state [17].

Materials such as Iron, cobalt, nickel and some rare earth metals are examples of Ferromagnetism.

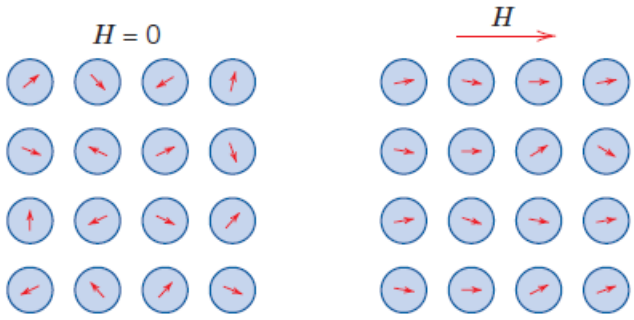

Figure 2.3. The paramagnetic behavior of atomic dipoles due to an applied magnetic field [13]

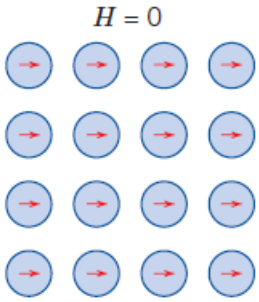

Figure 2.4. A schematic of the atomic dipole in a ferromagnetic material [13]

Saturation magnetization M_s of a ferromagnetic material takes place when all the magnetic dipoles in the material are all aligned with the applied field.

Antiferromagnetism: is the magnetic moment coupling between adjacent atoms or ions in an antiparallel alignment. In antiferromagnetic materials, the cancellation of opposing magnetic moments results in the solid having no net magnetic moment as shown in Figure 2.5. An example of an antiferromagnetic material is Manganese oxide which is a ceramic material.

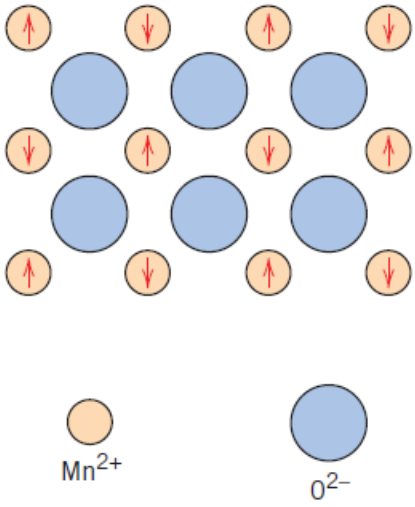

Figure 2.5. A schematic of the atomic dipoles in the antiferromagnetic material MnO [13]

Ferrimagnetism: is permanent magnetization that is similar to ferromagnetism in macroscopic magnetic characteristics but the source of the net magnetic moments is different. The net ferromagnetic moment is due to the incomplete cancellation of spin moments as shown in Figure 2.6. Examples of the ferrimagnetic materials are cubic ferrites, hexagonal ferrites, garnets and some ceramic materials which are good electrical insulators. For some magnetic applications such as high-frequency transformers, electrical insulating is desirable.

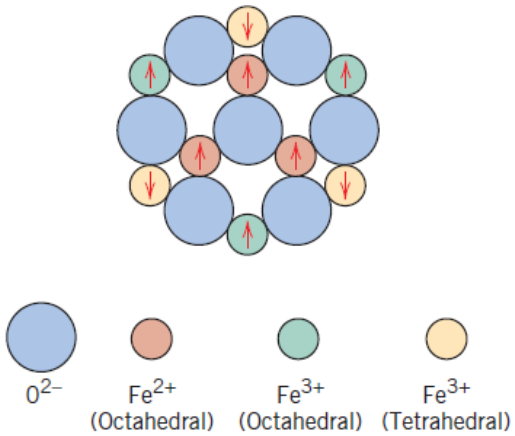

Figure 2.6. A schematic showing the atomic dipole in Fe_3O_4 which is a ferrimagntic material [13]

The Influence of Temperature on Magnetic Behavior: Raising the temperature of a solid will increase the thermal vibrations of atoms, and the increased motion of the atoms will randomize the direction of any magnetic moment that was aligned.

The increase in temperature will counteract the coupling forces between adjacent atomic moments and this means it will also decrease the saturation magnetization for ferro- and ferrimagnets. The saturation magnetization is maximum at 0 K. The saturation magnetization drops to zero at a temperature called Curie temperature T_C. At T_C ferromagnetic and ferrimagnetic materials become paramagnetic. Temperature influence on antiferromagnetism vanishes at a temperature called Neel temperature. But above that temperature antiferromagnetic materials are also paramagnetic.

2.6 Magnetic Domains and Hysteresis

Domains are the large volume regions of the crystal where the coupling interactions cause net spin magnetic moments of adjacent atoms to align with one another. Ferromagnetic and ferrimagnetic materials at temperatures below Curie temperature T_C are composed of small volume regions called domains with all magnetic moments mutually aligned as shown in Figure 2.7. Each domain is magnetized to its saturation magnetization. In a macroscopic piece of material the magnitude of the *M* field is the vector sum of the magnetizations of all domains.

It is important to note that the concept of a magnetic domain is different than grains that make crystalline materials; though a magnetic domain might consist of one grain with the same spin direction or several grains having the same spin direction.

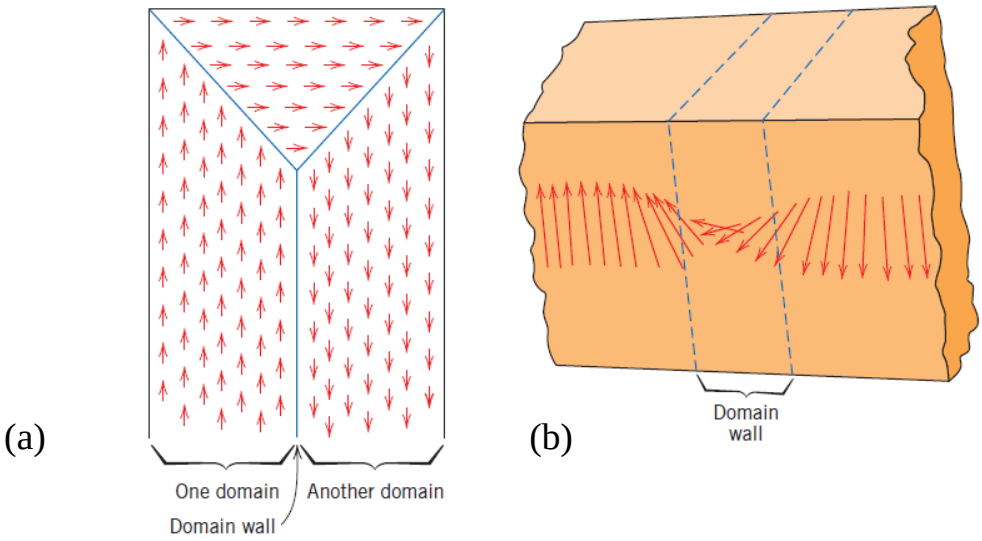

Figure 2.7. (a) A diagram of the spin alignment in magnetic domains, (b) The transition of the directed spins from one domain to another through the domain wall [13]

The hysteresis loop of a ferromagnetic material is shown in Figure 2.8. When a varying external field is applied on a ferromagnetic material, *B* varies as a function of *H* increasing slowly then more rapidly until saturation is reached. Saturation occurs when *B* is no more dependent on *H.* As the *H* field is being reduced by reversal of field direction, the path B-H curve will follow is symmetrical to the original path and the *B* decreases at a lower rate producing a hysteresis effect and a residual *B* field called the remanence at the zero *H* field. The resistance of domain walls to shifting happens due to the increase of the magnetic field in the opposite direction and causes the lag of *B* with *H* and the hysteresis shown in Figure 2.8. The hysteresis sometimes can also be produced from the *M* versus *H* curve. More *H* field should be applied in the opposite direction of the original field to get the *B* field to zero; this amount is called the coercivity or coercive field H_C.

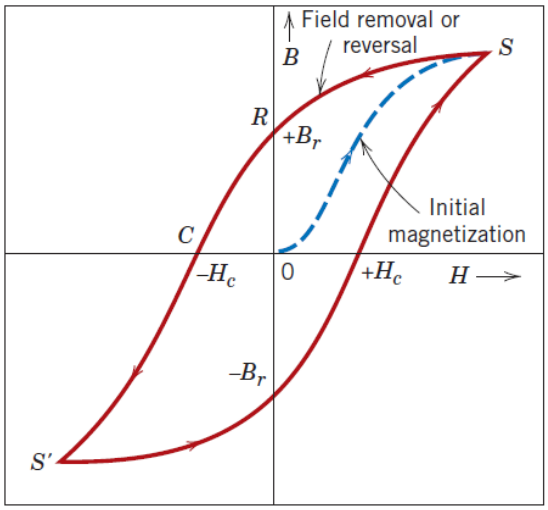

Figure 2.8. The hysteresis loop (B versus H). [13]

The magnetic domains in a ferromagnetic material originally have no net magnetization and the moments are randomly oriented as shown in Figure 2.9. The moments start to align themselves with the external applied field changing in shape and size. Usually the domains that were already aligned with the field increase in size including other domains with different orientations until they unite and the material reaches saturation.

Applying an external field with the same magnitude but on the opposite direction reverse the hysteresis. As the field *H* reaches zero the magnetization (or *B*) will not reach zero, instead it have some residual value called the remanence magnetization (or B_r); i.e. the material is still magnetized at zero field. The resistance of the domain walls to orient itself with the new direction causes some domains to stay on its former orientation and hence the remanence magnetization is seen in the hysteresis behavior.

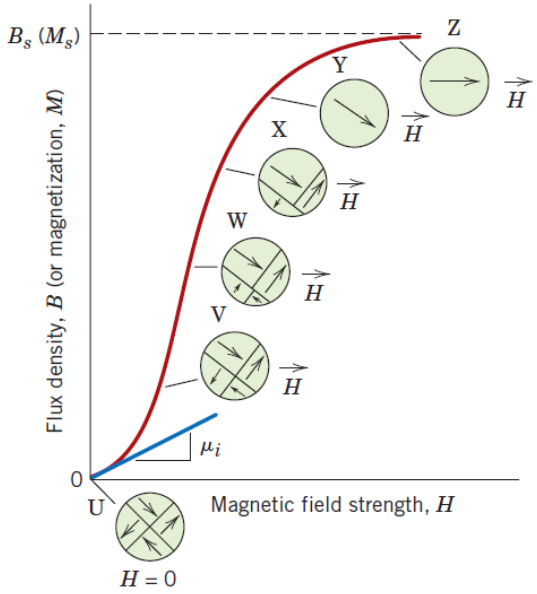

Figure 2.9. Domain transformations due to an external applied field in the related hysteresis [13]

2.7 Magnetic Anisotropy

Magnetic anisotropy is the dependence of magnetic properties on direction. In an anisotropic material, the magnetic moments will align with the easy axis. An easy axis is the energetically preferred direction of the spontaneous magnetization. One of the magnetic anisotropy sources is magneto-crystalline anisotropy which results from the atomic structure of a crystal introducing easy axis of magnetization. The factors that cause hysteresis curves to have different shapes are:

- If the material is a single crystal or polycrystalline
- For polycrystalline the preferred orientation of the grains
- The presence of pores or second-phase particles
- Temperature and mechanical stress state

Different curves are obtained for different crystallographic orientations when the field is applied on these directions; this magnetic behavior dependence on crystallographic orientation is

called magnetic anisotropy. Easy magnetization is the crystallographic direction in which saturation is achieved at the lowest field.

2.8 Soft and Hard Magnetic Materials

The size and shape of the hysteresis curve is important. In a hysteresis loop the area within the curve is the magnetic energy loss per unit volume of material. The energy loss transforms into heat that raises the temperature of the magnetic specimen.

Ferromagnetic and ferromagnetic materials are classified as soft or hard magnetic materials depending on their hysteresis curve. Soft magnetic materials have a small relative area within the hysteresis loop which is thin and narrow. Examples of applications of soft magnetic materials are devices subjected to alternating magnetic fields and in which low energy losses are needed. Soft magnetic materials must have high initial permeability and low coercivity.

- The saturation magnetization is dependent on the composition of the material.
- The susceptibility and coercivity (H_C) depend on the structural variables.

Soft magnetic materials are affected by the electrical resistivity. If a magnetic field that varies in magnitude and direction is applied energy is lost due to electrical currents called eddy currents. To minimize these losses in soft magnetic materials the electrical resistivity should be increased by forming solid solution alloys such as iron-silicon and iron-nickel alloys.

To improve hysteresis characteristics of soft magnetic materials for specific applications heat treatment can be applied accompanied by a magnetic field; then a square hysteresis loop will be achieved and that is helpful in some magnetic amplifier and pulse transformer applications. Soft magnetic materials are also used in generators, motors, dynamos, and switching circuits.

Hard magnetic materials have a high resistance to demagnetization and can be used in permanent magnets. Hard magnetic materials have high remanence, coercivity, and saturation flux density, low initial permeability and high hysteresis energy losses.

Important Characteristics of hard magnetic materials are Coercivity and energy product $(BH)_{max}$. $(BH)_{max}$ is the area of the largest *B-H* rectangle that can be constructed in the second quadrant of the hysteresis curve with units of kJ/m^3 (MGOe) or (10^6gauss-oersted). The energy product $(BH)_{max}$ is the value of the energy required to demagnetize a permanent magnet.

Hard magnetic materials can be categorized into conventional and high energy. Conventional hard magnetic materials have energy product in the range 0.25-10 MGOe; examples are ferromagnetic materials, magnet steels, (Cu-Ni-Fe) alloys, (Al-Ni-Co) alloys. High energy hard magnetic materials have energy product more than 10 MGOe; examples are $SmCo^5$ and $Nd_2Fe_{14}B$. The magnetization and demagnetization is affected by domain wall mobility which is controlled by microstructure size, shape, and orientation of the crystallites or grains and the distribution of any second-phase particles. Applications of hard magnetic materials are motors (cordless drills, screw drivers, in automobiles starting, window winder, wiper, washer, and fan motors and in audio and video recorders and clocks), speakers in audio systems, lightweight earphones, hearing aids, and computer peripherals.

2.9 Application of Pulsed Laser Deposition in Synthesis of Magnetic Materials

PLD has been used to grow films with variety of properties such as ferroelectrics, ferrites, amorphous diamond and other ultra-hard phases, biocompatible and tribological coatings, polymers, compound semiconductors, and nanocrystalline materials [18]. Despite the simplicity of the PLD it is a high versatile technique for thin films and multilayers fabrication [19] Pulsed Laser deposition proved its convenience in depositing thin films from complex targets to

preserve the stoichiometry of the target. Adjusting the Laser fluence can also sustain the amorphousness of the materials [20]; where fluence is described as the energy delivered per unit area. It is found that at lower fluence the film elemental composition is almost the same as the target[21]. Another advantage of using PLD for multilayer thin growth is the significant improvement of growth of simple metallic thin films/ multilayers through managing the deposition rate and kinetic energy opening the door for promising artificial thin films structures with good physical properties [22]. Williams et al. in 1994 examined the magnetic and structural properties of MnZn-ferrite films produced by PLD, they have concluded that the magnetic properties of the films are in god agreement with those of the bulk material [23]. A comparison between PLD and dc (direct current) sputtering was conducted by Mozhaev et al. They fabricated YBa_2Cu_3O thin films on $NdGaO_3$ substrates at similar deposition conditions. The dc sputtering produced better crystal quality because of the low deposition rate allowing time for recrystallization. However the dc sputtering increased the Ba deficiency in the films because of the low deposition rates which increase the influence of resputtering and re-evaporation of Ba. The PLD produced smooth surface on the c-oriented areas (where the film is oriented with the c-axis normal to the substrate surface) due to the high mobility on the film surface [24]. Chemical processes are widely used for manufacturing recording media for data storage devices but PLD is superior in fabricating nanoparticles and thin films composites in a multilayered geometry [25-27]. A chemical technique to synthesize FePt nanoparticles for data storage devices is been under investigation but it's a very complicated time consuming process [4, 28-32]. An epitaxial growth occur when a single crystal film grow relatively on a crystalline substrate. The epitaxial grown $Nd_2Fe_{14}B$ by PLD have coercive fields up to 2 Tesla due to the high crystallinity of the film [33].

PLD also proved successful in obtaining $Nd_2Fe_{14}B$ and $SmCo_5$ nanoparticles which were then post processed (annealed) to achieve the desired crystal structure [34].

2.10 Important Magnetic and Structural Properties for Recording Media

Studying the nanostructure morphology of magnetic thin films is important because the particle and grain size have great influence on magnetic properties of materials [35]. As particle sizes are reduced from bulk materials to nanoparticles their magnetic behavior changes. This is correlated to change in the size of magnetic domains; as the particle size is scaled down the exchange length converges stabilizing the state of the single domain from a multi-domain state. The coercivity of a material was studied as a function of particle size as shown in Figure 2.10 [36, 37]. The increase in energy caused by domain wall formation is much more than the decrease in energy due to formation of domains. Subsequently domain walls will not form below a critical particle size because of energy limitations and the single domain particles will stay stable.

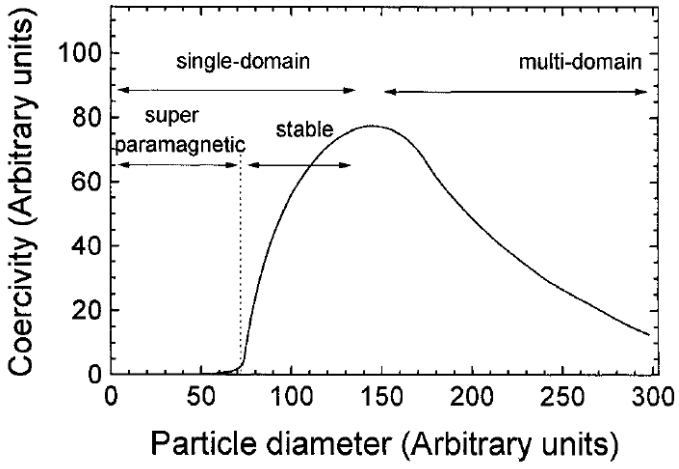

Figure 2.10. The magnetic behavior due to particle size reduction.

Several conditions affect the morphology of the films; the deposition temperature for instance changed the particle morphology from single particles to clusters [38]. Magnetic

materials are characterized by their hysteresis loop [39]. When applying an external magnetic field H_{app}, the magnetization M would reverse back when the field is applied in the negative direction. But magnetization will not reverse until more field is applied; this resistance is defined as coercivity H_c which is the amount of the extra applied field to reverse the magnetization. At the point where the applied field reaches zero the magnetization left is the remanent magnetization M_r. For hard magnets $\mu_0 M_r$ ranges from 0.5 to 1 Tesla and $\mu_0 H_c$ is $\geq$ 1Tesla. The reason behind remanent magnetization is the existence of an energy barrier caused by the magnetic anisotropy. A model called Stoner-Wohlfarth assume that the reversal occur by in-phase rotation of magnetic moments [40]. According to Stoner and Wohlfarth model the coercivity of non-interacting single domain particles is described by equation 2.8.

$$H_c = \frac{2K_u}{M_s} \qquad (2.8)$$

In the equation K_u is the anisotropy constant and M_s represents the saturation magnetization.

2.11 $L1_0$ Structure of FePt

In the data storage devices market FePt, CoPt and rare earth transition materials (RE-TM) are the main materials used as recording media. FePt thin films were embedded in different nonmagnetic layers of Ag [41], C [42], BN [43], SiO_2 [44], and Si_3N_4 [45] by magnetron sputtering to exchange decoupled hard magnetic materials. Based on the result of these studies it can be argued that coercivity depends on layer thickness, annealing temperature and on nonmagnetic materials added as well as parameters that determine particle size and interparticle separation. There are various phases of FePt such as Fe_3Pt, FePt, and $FePt_3$ that exist in ordered and disordered states. The most important phase is an $L1_0$ FePt ordered phase that has significant magnetic properties. FePt thin films fabricated by sputtering and PLD resulted in the growth of

high textured films with island morphology; very high coercivities were obtained ($\mu_0 H_c$>4T) [46, 47]. Another process utilizes a particle gun to deposit clusters directly was used to obtain FePt nano-particles with $\mu_0 H_c$ = 0.3 T [48]. Also to produce FePt nano-clusters a gas-aggregation process is studied by employing magnetron sputtering at the source [49]. To improve the extremely high density magnetic recording from 645 Gb/cm^2 to 6.45 Tb/cm^2, extremely uniform grain sizes with sizes less than 8 nm are needed [50-53]. To overcome the instability due to small grain sizes (superparamagnetism) high magneto-crystalline anisotropy is needed a barrier to switching of magnetization thermally [54]. FePt and CoPt clusters with high anisotropy L10 phase after annealing have been under investigation [55, 56]. A comparison between the hysteresis loop of as-deposited and after annealing loop is shown below in Figure 2.11.

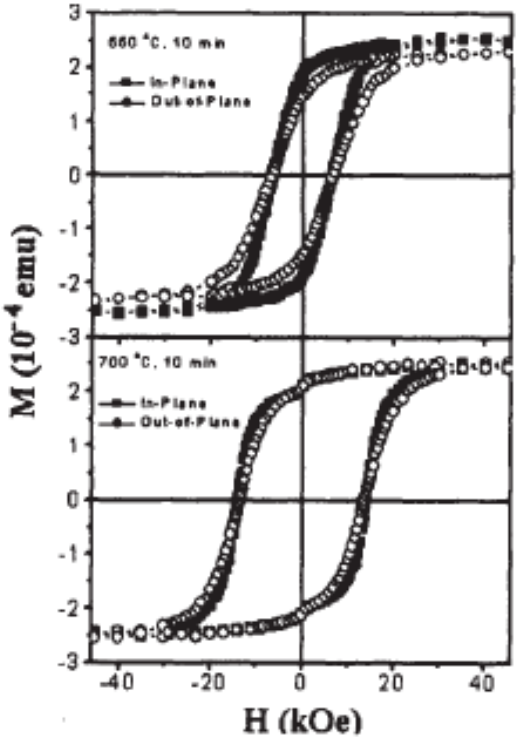

Figure 2.11. FePt hysteresis before and after annealing [57].

A study of the coercivity versus annealing temperature and annealing duration is proposed for future work, based on the results obtained by studies of FePt thin films as shown on

figure 2.12. The coercivity and annealing temperature followed a linear relationship for FePt thin films.

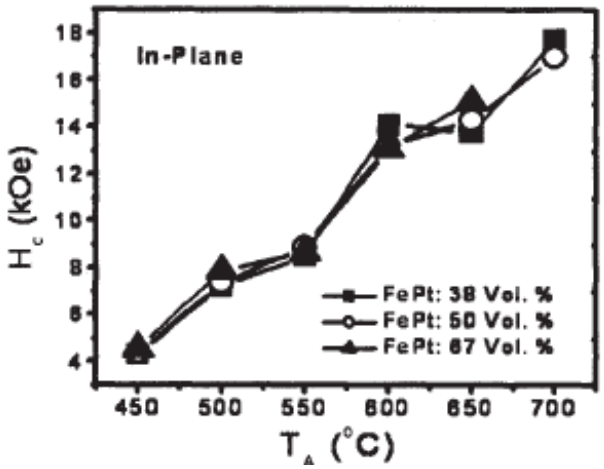

Figure 2.12. Coercivity versus annealing temperature [57].

2.12 Studies on $L1_0$ Structured FeNi Thin Films

The $L1_0$ ordered FeNi alloy is an important material that have been proposed as a magnetic recording media in data storage devices. It's a relatively new field; and researchers need to explore the possibilities of different fabrication techniques to develop the $L1_0$ structured thin films of FeNi. Shima et al. reported an attempt to prepare the $L1_0$ ordered FeNi films by alternate monatomic layer deposition (AMLD) at different substrate temperatures [58]. They also described the availability of the $L1_0$ FeNi alloys as scarce and that it's only found naturally in meteorites. AMLD employs expensive complicated e-guns to deposit the monolayers of Fe and Ni. The structure analysis Shima et al. performed revealed the formation of $L1_0$ FeNi structure indicated by a broad peak at $2\theta = 24°$. The peak was a maximum at substrate temperature of 280°C. As a result of the previous work, the use of Cu (001) over Au (001) as a buffer layer to induce the growth of $L1_0$ FeNi thin films were investigated by Mizuguchi et al. [59]. L10 structures have lattice constants close to Cu (001). Non-magnetic materials are preferred as buffer layers to prevent them from influencing measured magnetic properties. Mizuguchi et al.

concluded that a 6.37% lattice mismatch between $AuCu_3$ and $L1_0$ FeNi film occurred which led to the distortion of the $L1_0$ FeNi multilayer. It was noted that the in plane lattice constant (a-axis) of $L1_0$ FeNi is 0.3582 [60]. High uniaxial magnetic anisotropy in materials is reported to increase the thermal stability of magnetization specifically in a nanometer scale making these materials suitable for data storage applications [61-64]. $L1_0$ ordered FeNi alloys have large uniaxial magnetic anisotropy energy (K_u) of 1.3 X 10^7erg/cm [65, 66]. Kojima et al. fabricated $L1_0$ ordered FeNi films using molecular beam epitaxy over Au-Cu-Ni buffer layer [67]. It was also reported that the buffer layer should satisfy specific requirements such as being non-ferromagnetic, good lattice match to $L1_0$-Feni structure and flat surface for good epitaxial growth of $L1_0$ FeNi films. Ku have been estimated from parallel and perpendicular to plane M-H hysteresis curve by equation 2.9.

$$k_u = \left(\int HdM\right)_{in} - \left(\int HdM\right)_{perp} + 2\pi M_s^2 \qquad (2.9)$$

Another buffer layer which was investigated is Cu-Ni; which was chosen because it does not have a diffraction peak around the $L1_0$ FeNi super lattice peaks [68]. It is important to note that reflection high energy electron diffraction (RHEED) was usefully employed to ensure the epitaxial growth of different layers. According to Kojima et al. $L1_0$ FeNi super lattice peaks were found at $2\theta = 25°$ for (001) and $2\theta = 51°$ for (002). Most of these data were obtained from investigating the structural and magnetic properties of $L1_0$ ordered FeNi alloy extracted from a natural meteorite [69]. The atomic composition of the alloy was found to be 50.47 ± 1.98 % for Fe and 49.60 ± 1.49 % for Ni. The lattice constants estimated were a = b = 3.582Å and c = 3.607Å. The coercivity is more than 500 Oe and range from 500 to 4000 Oe [70-72]. In 1960 $L1_0$ FeNi was constructed by neutron irradiation at high temperature but this technique is not ideal for industrial application [65].

CHAPTER 3

Fabrication and Analysis Techniques

Single and multi-layers of thin films and nanoparticles were synthesized using PLD. The process parameters as well as the sample and chamber preparations are explored below. A brief introduction is also included for each of the characterization techniques implemented to analyze the samples. The experimental parameters for each system are specified in detail.

3.1 Pulsed Laser Deposition

Pulsed laser deposition (PLD) is the main technique utilized in fabricating the magnetic thin films and nanoparticles in this study. In this chapter a brief background of LASER and PLD is presented, as well as the growth mechanisms associated with this process.

3.1.1 Laser background and basic principles. After Theodor Maiman and his team operated the first Laser (Light amplification by simulated emission of radiation) in 1960, it has been utilized in many applications such as machining, military and medical applications. It also paved the way to more specific material science applications such as pulsed laser deposition, localized melting during optical fiber pulling, laser annealing of semi-conductors, surface cleaning by desorption and ablation.

Laser is described as monochromatic, coherent and directional. This is because it consist of one wavelength, emits light in a specific direction, and its wavelength are consistent in space and time. Light is defined as electromagnetic radiation with wavelength that range from 1 nm to 1000 μm; whereas Laser operate in the infrared and visible ultraviolet (200-400 nm) radiation of the electromagnetic spectrum. Light is made of quantum packets of energy called photons which behave as particles and waves at the same time. The intrinsic energy of photons is implemented in equation 3.1.

$$E = h\nu \tag{3.1}$$

Where ν is the frequency of light and h is Planck's constant. Also for waves the speed of light is described as a function of wavelength and frequency in equation 3.2.

$$\lambda\nu = c \tag{3.2}$$

Where λ is the wavelength of light and c is the speed of light in vacuum. Substituting equation 2 in equation 1 energy can also be expressed as

$$E = \frac{hc}{\lambda} \tag{3.3}$$

From this equation it is apparent that the photon energy is inversely proportional to wave length. Lasers are in the ultraviolet range which has a shorter wavelength than the infrared light; as a result photons making up Laser have higher energies than those of visible light. Stimulated emission occurs when atoms are stimulated by photons (from light) to transfer electrons from one energy state to another generating more photons with the same wavelength as the stimulating ones in the process. In a Laser system the Laser medium is pumped continuously to excite electrons into upper energy levels, and then they decay to lower levels producing more photons, at this point of the process population inversion is formed and photons will be amplified coherently. A system of mirrors reflects the off-axis photons out of the system and reflects the on-axis photons back into the population so it can be amplified by exciting more atoms; and this is how Laser is created. This process is shown in Figure 3.1and 3.2.

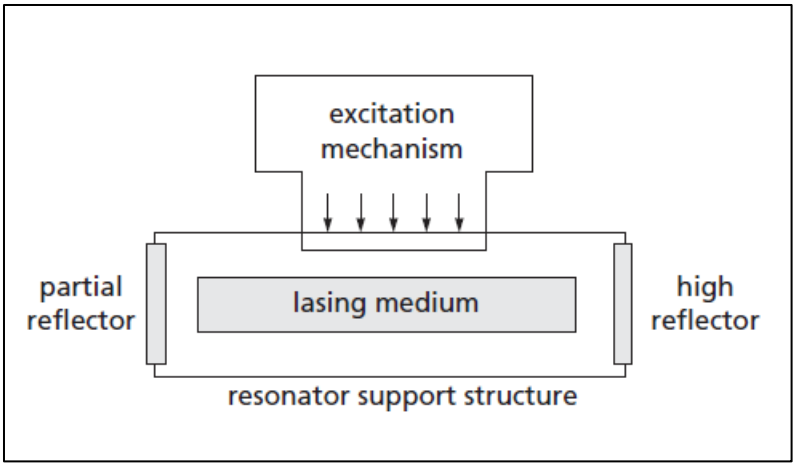

Figure 3.1. A basic illustration of Laser components.

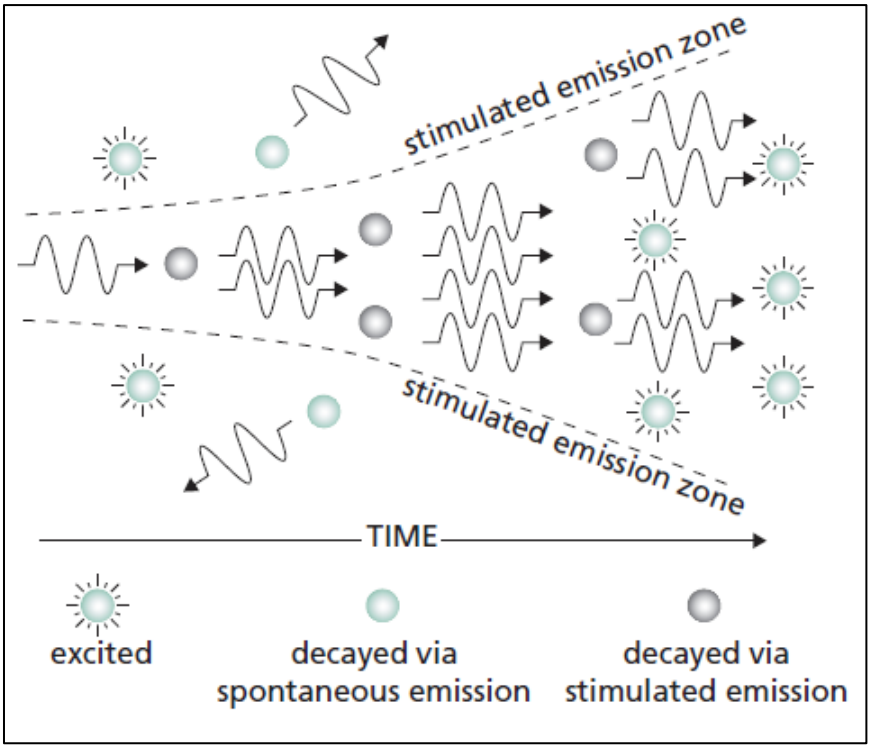

Figure 3.2. Creation of Laser by excitation of atoms to generate photons.

Laser can be incorporated in many applications based on its specific beam properties such as direction, divergence, and wavelength or frequency. These properties can be adjusted by controlling the size of the gain medium, location, separation and reflectivity of mirrors in the

optical cavity. There are many types of laser according to their operation techniques such as optically pumped solid-state Lasers, Liquid (dye) Lasers, gas Lasers (shown in Figure 3), semiconductor lasers, free electron Lasers, x-ray Lasers, and chemical Lasers.

The krypton fluoride (KrF) Laser utilized in this research falls in the gas Lasers class. The light amplifying substance in this case is a gas or mixture of gases. The gas molecules contained in a quartz tube are excited with an electric glow discharge. A subdivision of gas Lasers are the excimer Lasers which are pulsed Lasers. The medium in this case is a mixture of a rare gas and a halogen such as argon fluoride, Xenon chloride, and krypton fluoride. KrF has a wavelength of 248 nm. The excimer Lasers emit short 10-20 KW power pulses and it can reach repetition rates up to 1000 pulses/seconds. A pressure of 2-4 atm is maintained by adding helium to the Laser gas. Excimer Lasers are utilized in Laser surgery, metal holes drilling, in dye laser pumping, lithography and Pulsed Laser Depositions.

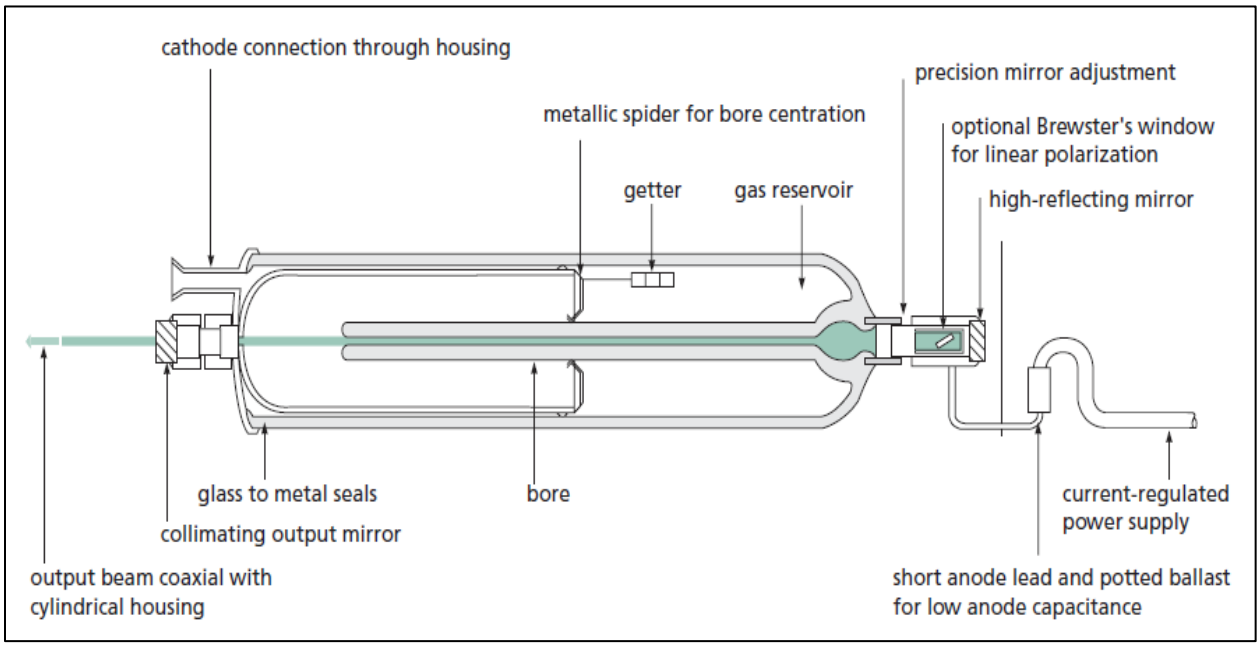

Figure 3.3. A diagram showing components of a gas Laser.

3.1.2 Classification of deposition technologies. There are many deposition technologies for material formation. These processes can be classified by the forming layer thickness from a few nanometers to about ten micrometers. These methods are either purely physical (e.g. evaporated methods) or purely chemical (e.g. gas-liquid-phase chemical processes) or processes classified as physical-chemical methods. These processes are listed on Table (3.1).

Table 3.1

A list of some deposition technologies

Evaporative Methods	
Vacuum Evaporation	
Conventional vacuum evaporation	***Molecular-beam epitaxy (MBE)***
Electron-beam evaporation	***Reactive evaporation***
Glow-Discharge Processes	
Sputtering	***Plasma Processes***
Diode Sputtering	Plasma-enhanced CVD
Reactive sputtering	Plasma oxidation
Gas-Phase chemical Processes	
Chemical Vapor Deposition (CVD)	***Thermal Forming Processes***
CVD epitaxy	Thermal oxidation
Atmospheric-pressure CVD (APCVD)	Thermal nitridation
Liquid-phase Chemical techniques	
Electro Processes	***Mechanical Techniques***
Electroplating	Spray pyrolysis
Electroless plating	Spray-on techniques

3.1.3 Criteria for selecting a method for an application. Some considerations should be taken into account; but there are no general guidelines for the selection. Thin-film Applications can be categorized as follows:

- Electronic Components
- Electronic Displays
- Optical Coatings
- Magnetic /films for Data Storage
- Optical Data Storage Devices
- Antistatic Coatings
- Hard Surface Coatings

3.1.4 Background of PLD. Pulsed laser deposition is one of the most important and simple techniques to grow nanoparticles and thin films. It's a physical vapor deposition (PVD) method that utilizes the laser beam which is intense enough to vaporize the hardest and most heat resistant materials. Also polycomponent materials can be ablated and deposited onto substrate to form stoichiometric thin films; this procedure is called pulsed laser deposition (PLD). The interaction of laser radiation with solid surfaces was under investigation from as early as 1962, when Breech and Cross analyzed the emission spectrum of material vaporized by laser pulses. The first demonstration of PLD, in 1962, did not produce significant interest, as the films deposited were inferior to those obtained via other deposition techniques, such as chemical vapor deposition (CVD) or molecular beam epitaxy (MBE). The technique remained dormant for approximately the next twenty years until Dijkamp and Venkatesan used PLD to grow a film of the high temperature superconducting material $YBa_2Cu_3O_7$ (YBCO). The films obtained were

found to be superior in quality to those previously grown using other deposition methods and triggered worldwide interest in the technique. Present day research applications include growing films for magnetic storage devices, developing multilayer devices for x-ray optics, depositing diamond films on components for protection and insulation and coating of nano-particles to increase the ignition properties of materials [8].

3.1.5 PLD systems. In PLD, a pulsed laser beam is focused onto the surface of a solid target, Figure 3.4. The target is rapidly evaporated due to the strong absorption of electromagnetic radiation by its solid surface. If ablation is carried out in vacuum, the glowing plasma plume in front of the target surface will consist of highly excited and ionized species. [9]

The principle of pulsed laser deposition, in contrast to the simplicity of the system set-up, is a very complex physical phenomenon. It does not only involve the physical process of the laser-material interaction of the impact of high-power pulsed radiation on solid target, but also the formation plasma plume with high energetic species and even the transfer of the ablated material through the plasma plume onto the heated substrate surface. Thus the thin film formation process in PLD generally can be divided into the following four stages:

- Laser radiation interaction with the target
- Dynamic of the ablation materials
- Deposition of the ablation materials with the substrate
- Nucleation and growth of a thin film on the substrate surface

At sufficiently high flux densities and short pulse duration, all elements in the target are rapidly heated up to their evaporation temperature. The instantaneous ablation rate is highly dependent on the fluencies of the laser shining on the target. The ablation mechanisms involve many complex physical phenomena such as collisional, thermal, and electronic excitation,

exfoliation and hydrodynamics. In the second stage the emitted materials tend to move towards the substrate according to laws of gas dynamics. Laser fluence is described by the following equation.

$$\text{Fluence } [J/cm^2] = \text{Laser pulse energy (J) / effective spot size } (cm^2) \quad (3.4)$$

During the interaction between an incident laser beam and a metal target, part of the laser beam energy is reflected to the ambient and the rest of it is absorbed within a short penetration depth in the metal. A liquid pool is formed on the surface when the laser pulse energy is sufficient to reach the melting temperature. At low intensities skin depth absorption and surface heating eventually drive heat conduction into the material. At higher intensities, the liquid metal vaporizes. The generated vapor consist of neutrals, excited species, dissociated, and ionized atoms or molecules, thus creating a high-density plasma which further absorbs incident laser light [10].

The laser-plasma-target interactions may strongly affect the energy delivered to the target surface. The coupling of the laser radiation with the target may be substantially different from that due to surface absorption alone. This phenomenon is called “thermal coupling”. Energy can be transferred from the plasma to the target by one or combinations of any two, or possibly all of the following three mechanisms:

- Normal electron heat conduction
- Short wave-length thermal plasma radiation which is absorbed by the metal surface
- Condensation of vapor forced back to the target surface by the plasma pressure

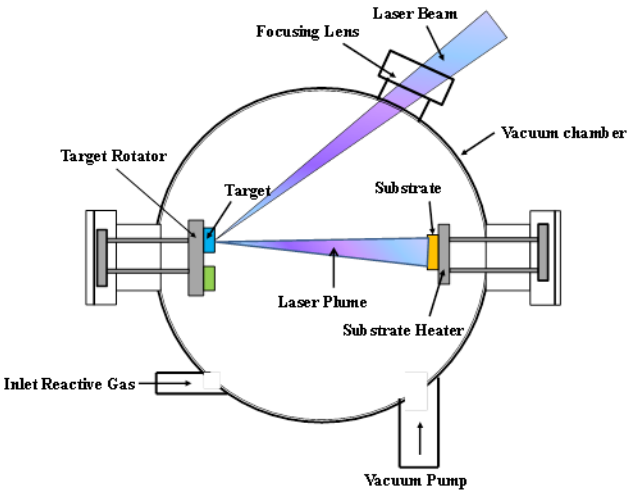

Figure 3.4. A PLD schematic illustration

These three mechanisms provide additional heat flux contributions to the target surface, which may or may not exceed the loss of the incident laser light flux due to plasma absorption. When the vapor becomes slightly ionized, it absorbs some of the incident laser radiation. The energy is converted to internal energy of the plasma. Increasing plasma temperature, the degree of ionization of the vapor is also increased, allowing further enhancing absorption of the incident radiation. As the plasma density and temperature rise, the vapor phase progressively behaves like an optically thick medium. The plasma effectively shields the target surface from the trailing part of the laser pulse. The energy in the plasma is then transferred away by thermal radiation or converted into hydrodynamic motion. Due to lateral expansion of the plasma, the energy radiated from the plasma to the target is often distributed over an area significantly larger than the laser beam spot. The gas dynamics of the plume have been discussed in more details in literature [73-75].

3.1.6 Film nucleation and growth. Atoms evaporated from target arrive either at the substrate surface directly or at formed cluster of atoms. The atom might condense or reevaporate

to condense again at a different spot. Greene's total free energy equation (equation 3.5) governs the growth process and three modes of growth are then identified.

$$\Delta G = a_1 r^2 \Gamma_{c-\upsilon} + a_2 r^2 \Gamma_{s-c} - a_2 r^2 \Gamma_{s-\upsilon} + a_3 r^3 \Delta G_V \qquad (3.5)$$

In equation 3.5 r is cluster radius, Γ's are interface energies, ΔG_V is the change in volume free energy due to condensation, a's are constants depending on nuclei's shape. The substrate – film system most likely will follow one of the growth modes based on these factors:

- The thermodynamics of the film and substrate surface energies.
- The film-substrate interface energy.

The nucleation and growth modes are:

Volmer-Weber mode: (shown in Figure 3.5) the crystalline films grow from 3D nuclei, interactions of atoms to atoms are in favor of the atoms to substrate surface interaction, as a result 3D cluster or islands will form.

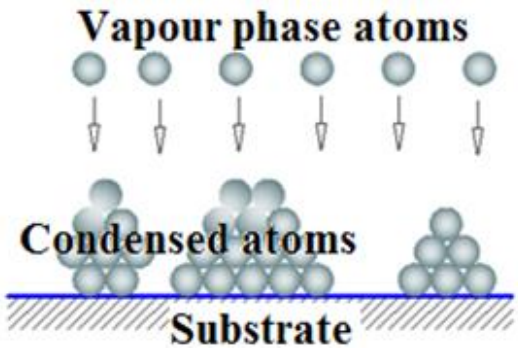

Figure 3.5. Formation of 3D clusters on substrate surface.

Frank-Van der Merwe mode: In this mode the evaporated atoms are more likely to grow as full complete monolayers on substrate surface before secondary layers start growing as shown in Figure 3.6.

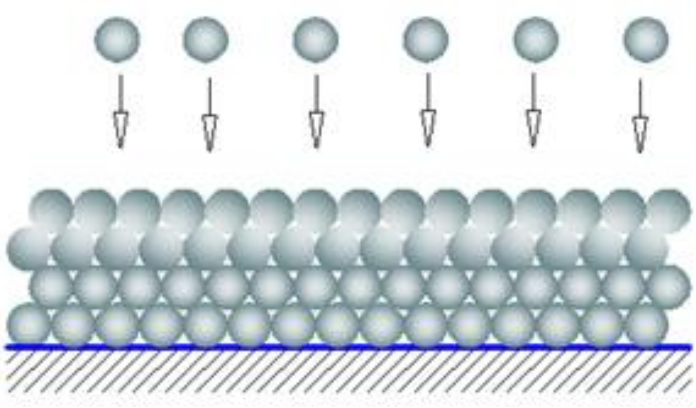

Figure 3.6. Complete layer by layer growth on substrate surface.

Stranski-Krastinov mode: The evaporated atoms form full monolayers on the bare substrate surface first; subsequently 3D clusters and islands will start growing on the following layers. This is illustrated in Figure 3.7.

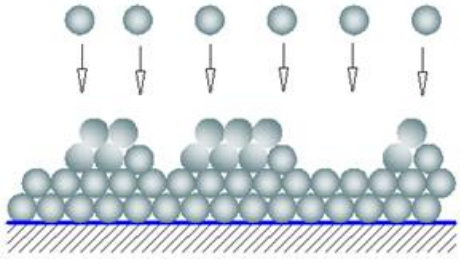

Figure 3.7. The growth of several complete monolayers before formation of clusters.

However these modes assume homogeneous nucleation at random spots on the substrate surface, whereas in real experiments there will be some substrate defects such as atomic steps, point defects, and dislocation intersections which will create low energy sites. As a result heterogeneous nucleation will occur.

3.1.7 Advantages and disadvantages. Advantages of PLD method over other deposition techniques such as molecular beam epitaxy and metallorganic vapor phase epitaxy include the unique process of source material transfer which limits the amount of heated material virtually only to that which is liberated; its pulsed nature, which affords high controllability of the

deposition thickness, plus the potential of synchronizing the high flux/short duration pulses with pulsed reactive gas sources; the high kinetic energy of the ablation plume, which promotes surface mobility on the growing film; and the ease of source material replacement. With respect to other process such as chemical-vapor deposition or ion implantation, PLD allows for easy handling, since the laser source is placed outside the reaction chamber. Another important characteristic of PLD is its multi-target carousel allowing easy fabrication of composite multilayers thin films. However, there are some disadvantages of PLD method, like the production of laser droplets, inhomogeneties of deposition rates resulting from the profile of the ablation plume; pulse to pulse fluctuations in the laser intensity; and possible nonstoichiometric material transfer of multi-element targets such as in the case of ceramic high-temperature superconductors. These problems arise not only from material specific properties, but also from technological limitations and incomplete understanding of the control parameter space. Those are defined, among others, the laser fluence, pulse duration, wavelength, the laser pulse's spatial profile, the ablation target absorption properties, target geometry, and the erosion characteristics of the target material.

3.2 PLD Experimental Setup

A picture of the PLD systems used in this research is shown in Figure 3.8. The Laser is a KrF excimer Laser (Lambda Physik, LPX 300). KrF emits Laser at a wavelength of 248 nm and pulse duration up to 30 ns. The pulse energy of the Laser system is 1.2 J measured at low repetition rate. The maximum repetition rate is 50Hz and average power is 50 W. The system is equipped with a remote controller. The gas used as a lasing medium is a mixture of Krypton, Helium, Fluorine and Neon. One of the important characteristics of this Laser system is the adjustability of the pulse energy and repetition rate.

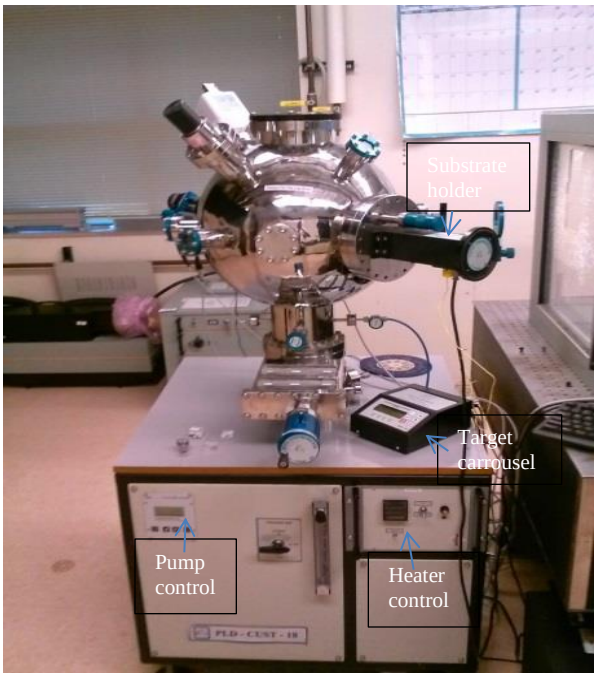

Figure 3.8. The PLD Chamber

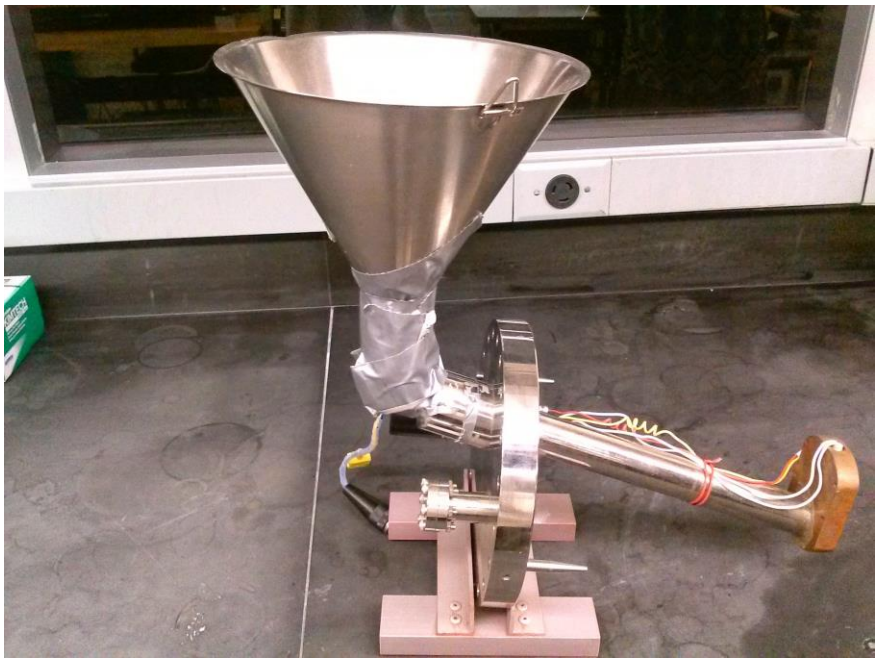

Figure 3.9. Liquid N_2 substrate holder

The depositions were conducted in an Excel Instruments vacuum chamber. The chamber is spherical facilitated with an automated target carrousel with controller. The stepper motor on the target carrousel is a rectangular motor with an indexing knob at the back of the motor. The

indexing knob indicates the angular position of the motor shaft and hence the position of the targets. A set of gears enables the positioning and rotation of targets. The target holder can carry up to 6 targets at once; and the Laser can be controlled to hit the desired target for the specific duration with the controller. The substrate heater (or holder) can be heated up to 800 °C with the temperature controller for the specified period of time. The heater is a circular flat plat resistive heater armed with a radiation shield to prevent heat loss and increase uniformity of the heated surface. The substrates can be glued to the heater using Silver paint or a Copper tape. For continuous measurement of heater temperature a K type thermocouple is connected to the heater. Substrate to target distance can be adjusted by the x-y-z assembly attached to the heater. The substrate can also be shielded from the pre-ablation evaporated material with a shutter. Another important fixture used to replace the substrate holder is a Liquid N_2 substrate cooler which is designed and fabricated at North Carolina A&T State University by Dr. Kumar's team. The substrate temperatures can be as low as 86 K.

The PLD system is equipped with a gas flow assembly and a gate valve to allow for chamber flushing and for deposition to be carried in a gas reactive environment. A lens holder is mounted at the Laser gate to focus the beam on the target to get the required energy density by adjusting the lens x-y-z assembly.

A turbo molecular pump coupled with a roughing pump was used to vacuum the chamber to pressures as low as 10^{-8} Torr. In our experiments the vacuum was in the order of 10^{-6}-10^{-7} Torr.

3.2.1 PLD chamber preparations. Before each deposition the surface of the substrate heater was sanded using a grade 400 SiC paper to remove any deposited film from previous experiments and then wiped using Isopropanol. The chamber walls and windows were also

cleaned to prevent dirt and residue from deposition build up, the cleaning is important specifically for windows to prevent beam diffraction due to unclean glass.

3.2.2 Target preparation. $Fe_{50}Ni_{50}$ alloy was prepared at University of Nebraska. Fe and Ni metal powders with 50% weight were milled for 30 minutes in a sealed ball milling container. The powders were then melted using a vacuum arc melting system. The resulting melt was machined to produce the $Fe_{50}Ni_{50}$ target. Other targets used in the depositions are 2.56 cm in diameter and 0.32 cm thick 99.9% pure Fe, 99.99% pure Ni, 99.999% pure Au, and 99.999% pure Al_2O_3. The target surfaces smoothed by isopropanol wet sanding by a grade 800 SiC paper. This step is very important to reduce particulates depositing on the film [76]. The target is then ultrasonically cleaned in Isopropanol for five minutes. The targets were mounted to a target holder by applying Silver paste. The target holder would then be heated at 80°C for 30 minutes to help the Silver paste dry. The targets were mounted on the target carrousel. In the case of using more than one target they were placed at 0° and 180° to minimize target to target contamination during depositions.

3.2.3 Substrate preparations. Two types of substrates were used in this study. One was 5x5x5 mm Sapphire (single crystal glass Al_2O_3) and highly polished Silicon (100). Silicon and sapphire were chosen as substrates for two reasons; in the first place because of their preference as substrates in electronic devices such as transistors, diodes, semiconductors and integrated circuits (ICs), secondly because of their availability. The Silicon substrates were cut using a diamond cutter into 5x5 mm and 10x10 mm pieces. The bigger Silicon substrates were needed to perform the x-ray diffraction analysis. The sides of the Silicon substrates were mechanically polished under water with a grade 400 SiC paper. The Silicon substrates were cleaned in an ultrasonic bath of Windex for 5 minutes, followed by ultrasonic bath in distilled water, Ethanol

and Acetone for 10 minutes each. Then the samples were submerged in Hydrofluoric Acid (HF) to remove any oxide that may have formed on the silicon surface. The samples were then immediately mounted to the substrate holder using Silver paint. The holder was heated to 100°C for 5 minutes prior to installation on the chamber. After it cooled it was ready to be mounted to chamber.

Figure 3.10. Ultra sonic cleaner

3.2.4 Deposition parameters. Controlling the deposition parameters is essential for fabricating good quality films. Close attention is needed when determining a specific parameter. For example the deposition temperature and the thermodynamic nature of the substrate affect the nucleation and growth modes and hence the crystallinity of the film [77]. In this research, depositions were carried at room temperature, 200°C, 400°C, 600°C and Liquid N_2 temperature. The Laser energy also affects the amount that can be ablated from the target (plume). Three different set of experiments were carried in this research. 3.2, 3.3 and 3.4 states the parameters used for each sample. For example, in Table 3-3, first column mentions the sample's code, second column describes the material configuration, and third and fourth columns list the pressure and temperature used during the film deposition. Laser energy, no of laser pulses and pulse repetition rate are tabulated in last three columns. Similarly, the laser parameters used for three types of samples that were subjected to annealing are listed in Table 3-3. The sample code

and laser parameters for gold experiments are presented in Table 3-4. $Fe_{50}Ni_{50}$ thin film was deposited from 40000 pulses. Fe/Ni multilayers were deposited by 1000 pulses each for 20 repetitions. Al_2O_3 spacer layer was deposited by 1000 pulse and then alternate $Fe_{50}Ni_{50}$ of 1000 pulses and Al_2O_3 of 500 pulses were repeated for 26 times. The number of pulses and repetition was determined according to literature and also from growth rate study using the profilometer. It's very important to note also that structural analysis require films thicker than 100 nm in order to fit with the beam alignment.

Note: In accordance with the commonly used practice of expressing high temperatures in degree Celsius (°C) and low temperatures in Kelvin (K), two units have been employed for temperature in this dissertation. The deposition temperatures are expressed in °C and magnetic measurement temperature are expressed in K.

Table 3.2

$Fe_{50}Ni_{50}$ thin films, Fe/Ni multilayers and $Fe_{50}Ni_{50}/Al_2O_3$ multilayer thin films

Sample ID.	**Material**	**Vacuum Pressure Torr**	**Substrate Temperature ° C**	**Laser Energy mJ**	**Pulse rate Hz**
47	$Fe_{50}Ni_{50}$	6.3×10^{-7}	25°	500	20
48	$Fe_{50}Ni_{50}$	5.4×10^{-6}	200°	500	20
49	$Fe_{50}Ni_{50}$	3.0×10^{-6}	400°	500	20
50	$Fe_{50}Ni_{50}$	3.0×10^{-6}	600°	500	20
51	$Fe_{50}Ni_{50}$	8.6×10^{-8}	-196°	500	20
52	Fe/Ni	2.2×10^{-6}	25°	500	20
53	Fe/Ni	8.6×10^{-7}	200°	500	20
54	Fe/Ni	1.4×10^{-6}	400°	500	20
55	Fe/Ni	8.6×10^{-7}	600°	500	20
56	Fe/Ni	6.3×10^{-7}	-196°	500	20
57	$Fe_{50}Ni_{50}$ Al_2O_3	1.9×10^{-7}	25°	500	20
58	$Fe_{50}Ni_{50}$ Al_2O_3	1.4×10^{-6}	200°	500	20
59	$Fe_{50}Ni_{50}$ Al_2O_3	1.0×10^{-6}	400°	500	20
60	$Fe_{50}Ni_{50}$ Al_2O_3	4.6×10^{-7}	600°	500	20
61	$Fe_{50}Ni_{50}$ Al_2O_3	6.3×10^{-8}	-196°	500	20

Table 3.3

$Fe_{50}Ni_{50}$ single layers for annealing testing

Sample ID.	**Material**	**Vacuum Pressure Torr**	**Substrate Temperature ° C**	**Laser Energy mJ**	**No. of pulses**	**Pulse rate Hz**
32	$Fe_{50}Ni_{50}$	4.6 X 10^{-7}	25°	500	20,000	20
35	$Fe_{50}Ni_{50}$	3.4 X 10^{-7}	600°	500	20,000	20
37	$Fe_{50}Ni_{50}$	1.0 X 10^{-7}	-196°	500	20,000	20

Table 3.4

Samples with a gold layer as a catalyst

Sample ID.	**Material**	**Vacuum Pressure Torr**	**Substrate Temp. ° C**	**Laser Energy mJ**	**Target**	**No. of pulses**	**Repet. no**	**Pulse rate Hz**
70	Au/$Fe_{50}Ni_{50}$	2.5 X 10^{-7}	25°	300	Au	200	1	10
					$Fe_{50}Ni_{50}$	40000	1	
73	Au/$Fe_{50}Ni_{50}$	5.7 X 10^{-7}	600°	300	Au	200	1	10
					$Fe_{50}Ni_{50}$	40000	1	
74	Au/Fe/Ni	1.6 X 10^{-6}	25°	300	Au	200	1	10
					Fe	42	480	
					Ni	33	480	
75	Au/Fe/Ni	4.2 X 10^{-7}	600°	300	Au	200	1	10
					Fe	42	480	
					Ni	33	480	

3.3 Film Thickness Measurement

To obtain the growth rate for thin films deposited under different PLD parameters, separate depositions were conducted. The substrates were cut of Silicon (100) in dimensions of 15 x 15 mm. They were masked by 10 x 15 mm Silicon pieces to shade half of the substrate from the deposition as shown in Figure 3.11. This process would allow the stylus sensor to measure the step created by the grown thin film on half the substrate.

The measurements were taken using a KLA Tencor Alpha-Step IQ® stylus surface profiler. The process was conducted under 13 mg stylus tracking force with a sensor range of 20 μm / 1.19 pm. The scanned distance over the sample surface was set at 500 μm with scan speed of 20 μm/s and sampling rate of 50 Hz.

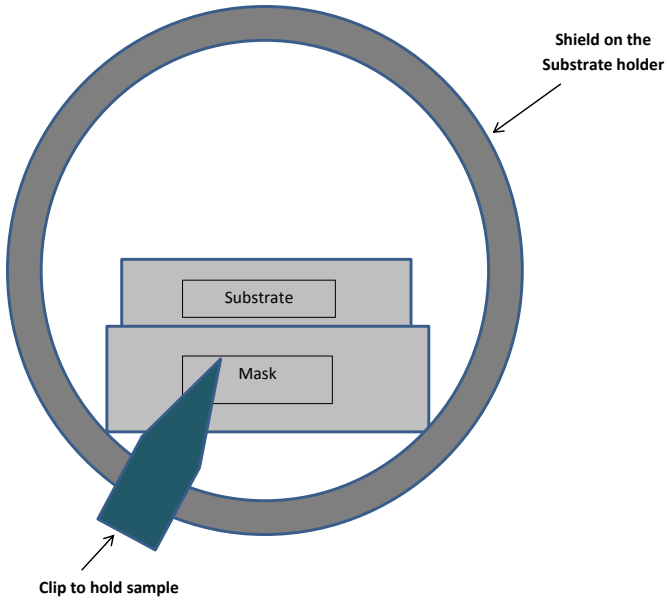

Figure 3.11. A schematic of the masked substrate for film thickness measurement

Stylus profilometers are superior compared to other contact profilometers because they are easy to use and can take measurements in the nanoscale; Alpha Step profiler has an 8 Å step height repeatability. However they are not suitable to measure soft or easy damageable surfaces because the hard tip contact the measured sample and may damage it. The profilometer main components are a measurement head with a stylus tip (shown in Figure 3.12) and a scan table. A photo of the system is also provided in Figure 3.13. A beam of light is used to adjust the positioning of the film and to read the surface. The stylus traces the surface and read the step caused by surface topography. The data are collected using the stylus profiler software which can be controlled to automatically level and display results in an Excel compatible format.

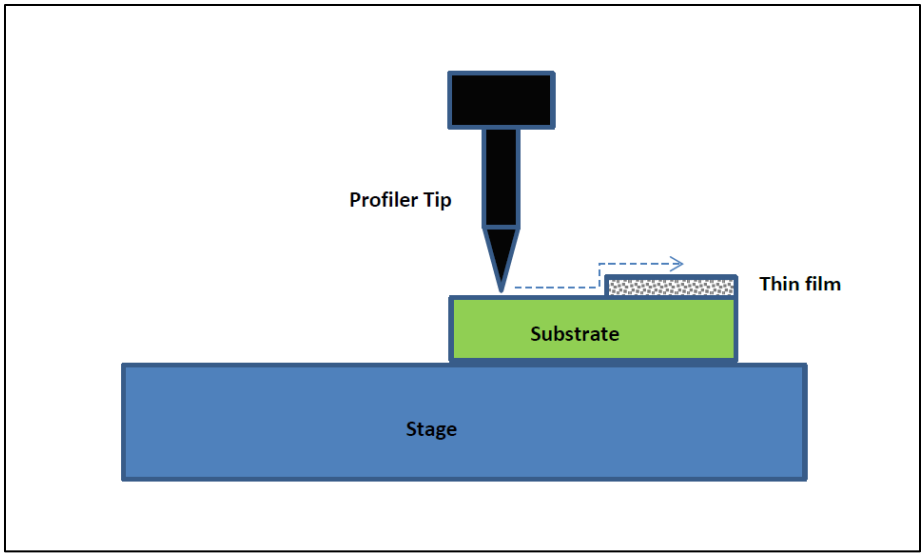

Figure 3.12. Surface Profile

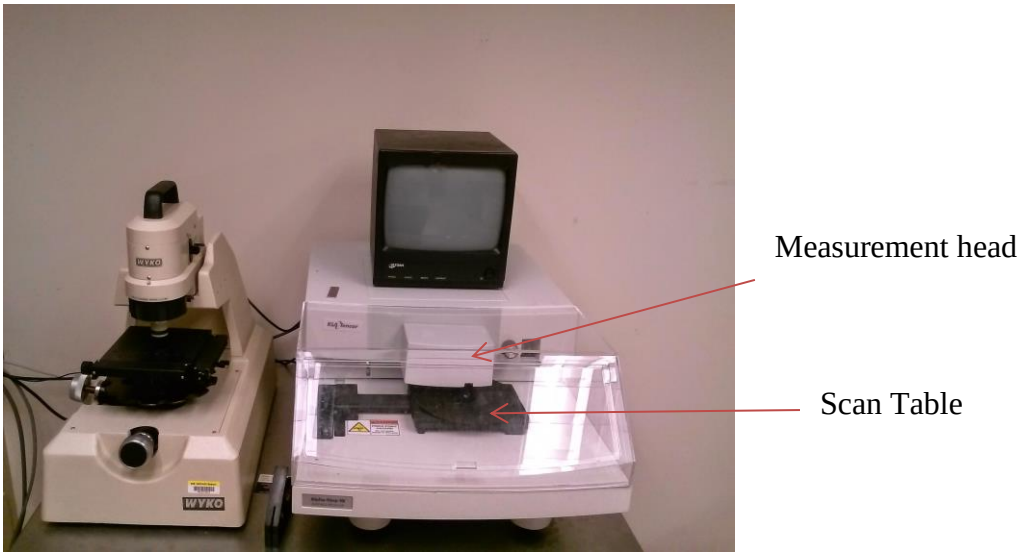

*Figure 3.13.*A photo of the profilometer

3.4 Atomic Force Microscopy

Atomic force microscopy (AFM) is member of the scanning probe microscopy (SPM) [78]. In AFM, the working mechanism is based on the interatomic forces that displace the sharp stylus tip on the sample surface to measure surface morphology. Previously the tip is mounted on an electrically conductive cantilever beam which was used to detect motion by means of a tunneling junction. Recently an optical interferometry is used instead. The system was invented

by G. Binning in 1986. His main theory stated that the attractive and repulsive forces between the atoms of the tip and atoms at the surface will cause small movements of the cantilever beam and these movements can be measured as mentioned before by a tunneling microscope. A schematic of an atomic force microscopy system is shown in Figure 3.14.

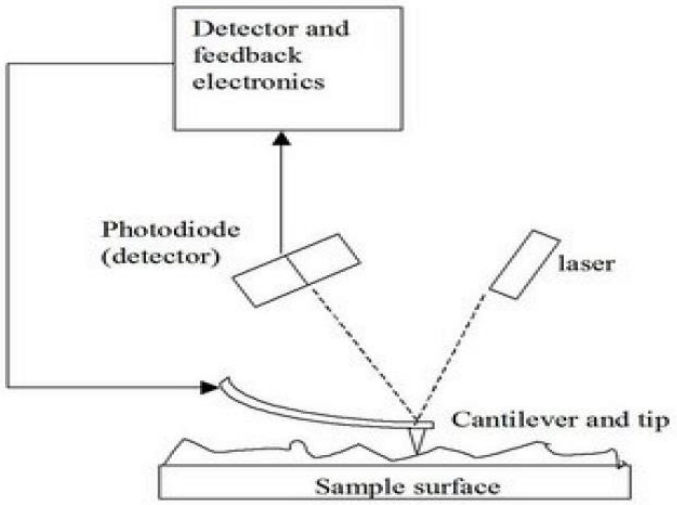

Figure 3.14. Atomic force microscopy.

The analysis using AFM can be carried under vacuum, air or liquid environments. AFM is also capable of scanning large surface areas [79, 80]. AFM can also provide measurements in three dimensions x, y, and z (normal to sample surface). The images resolution range from 0.1 to 1.0 nm [81].

In this work, the surface morphology was analyzed by using a NTEGRA Prima Modular scanning probe microscope from NT-MDT. The system was configured with the scanning by sample piezo-sensor (range 10x10 micron), and super sharp diamond-like carbon (DLC) tip with a typical spring constant of about 11.5 N/m ,a resonance frequency around 255 kHz and a typical curvature radius 1 nm (K-Technano model no. NSG10-DLC) was used for scanning. The images were recorded in ambient conditions (25 °C and 20 % relative humidity) and in soft

intermittent contact (semi-contact) mode. Tapping force was controlled by the ratio between set point amplitude (A_{sp}) and the free air amplitude (A_0). Several topographical images with areas 1.2x1.2 μm^2 and 0.6x0.6 μm^2 were recorded for each sample was, each scan area contains 512x512 (scan steps 2.35 nm and 1.1 nm). The scan rate was 0.5Hz. During acquisition of surface morphology, height images and amplitude error were recorded at the same time. Prior measurements the samples were cleaned in ultra-sonic bath with acetone (grade XXX) and methanol (grade XXX) and then blow-dried with nitrogen gas.

All off line image processing (flattening) and particles analyses were conducted at the software environment provided by the AFM manufacturer (Nova v1.1.0.1913 and IA-P9).

3.5 X-ray Diffraction

XRD is a nondestructive technique used to provide qualitative and quantitative analysis of materials' crystal structures [82]. In an XRD the x-ray beam directed on an atom might be absorbed (electrons will be ejected) or scattered [83]. The x-ray beam is an electromagnetic like light but with much shorter wavelength [84]. X-rays can be produced using an x-ray tube where electromagnetic waves are generated from impacts of high energy electrons with a metal target. Another way to create x-rays by confining high energy electrons in a storage ring; this is called synchrotron. The electrons in Synchrotron are accelerated by moving them in a circular orbit to emit electromagnetic radiation [85]. The orientations of atoms in a crystal in a regular pattern lead to constructive interference in few directions; the in phase waves (x-ray beam) will scatter and exit the sample at different directions. Then a detector sensitive to x-rays will measure the intensity and direction of the scattered beam.

The XRD system used in this research employed a position sensitive detector (PSD) which can measure the intensity of the diffracted beam in multiple points. The XRD system used

was a Bruker® AXS D8 Discover diffractometer. The radiative source was a CuKα. The CuKα have a wave length of 1.5 Å and run on 40 KV and 40 mA. Slits to narrow the beam are provided with different sizes. Tn this work 0.2 nm slits are placed on the source and detector. The samples are aligned with the X-ray beam by a point detector and Z-scan. An area detector is used to scan sample by locked coupled scan. A schematic of the X-ray diffraction system is shown in Figure 3.15.

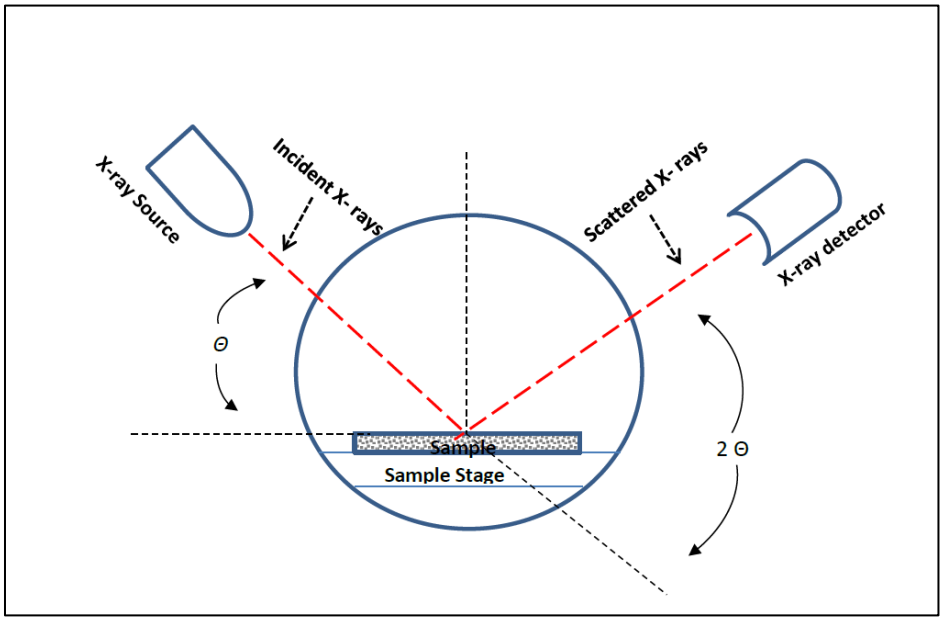

Figure 3.15. A Schematic of a XRD system

3.6 Scanning Electron Microscopy and Energy Dispersive X-ray Analyzer

SEM is a technique highly used by researchers in biological, medical and material sciences to obtain magnified images and chemical information of different types of specimens. It was invented in 1927 by H. Stintzing [86]. In our case it is essential to have these images to investigate the growth on the substrates in micro and nanoscale [87]. The SEM is made of a microscope column and the electronics console. The column consists of an electron gun (cathode, Wehnelt cylinder, anode), condenser lenses, two pairs of beam deflection coils, objective lens and apertures. The system operates in high vacuum and dry environment to

generate high energy beam of electrons for imaging. The image is produced by collecting different signals that are scattered due to high energy beam interacting with the sample. The two main signals from the primary beam that form images are the back scattered electrons (BSE) and secondary electrons as shown in Figure 3.16.

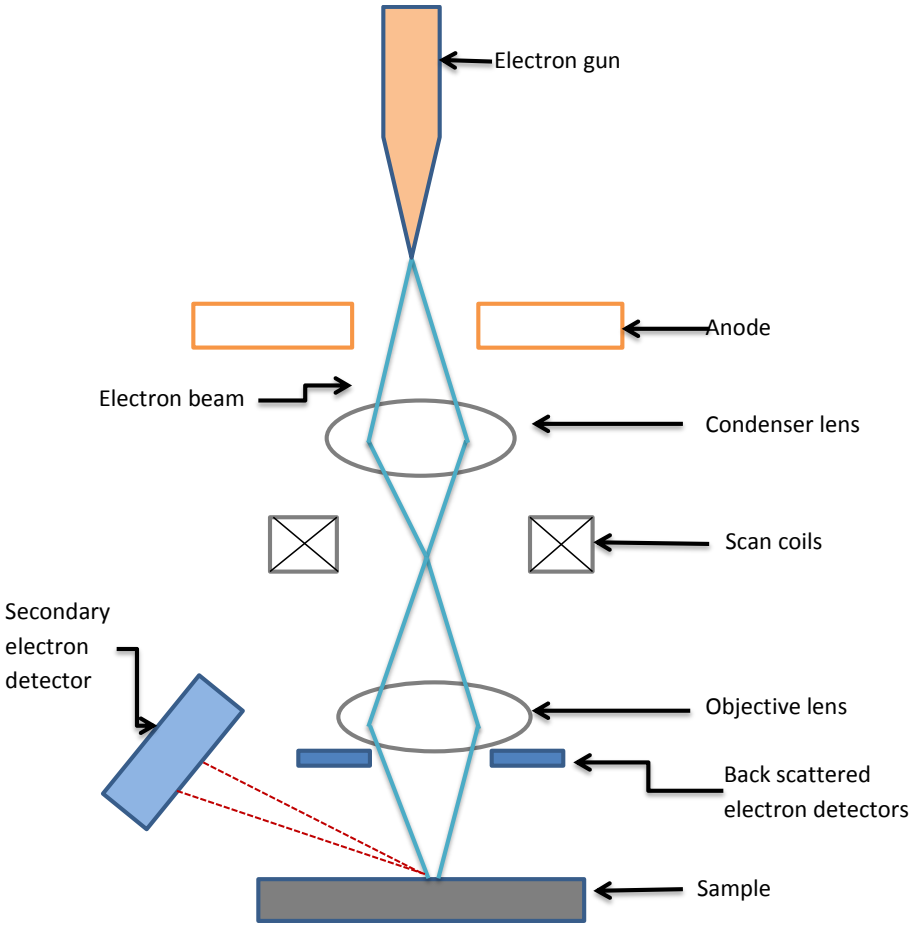

Figure 3.16. A Schematic of SEM

SE detectors are used to collect the needed information about surface morphology and topography [87]. The BSE detectors help in specifying the particles or areas with different average atomic number [88]. The SEM system used to obtain images of deposited thin films of FeNi was a Hitachi® SEM SU8000. In order to acquire high quality images the proper current and voltage have to be determined by trial and error. The chemical compositions were also found

using the energy dispersive x-ray analyzer (EDX) attached to the SEM. The x-ray detector measures the amount of the x-rays emitted and their energy which is a specific value for each element and accordingly the composition is determined [89].

3.7 The Physical Properties Measurement System

The Quantum design PPMS is a unique tool that can be utilized to perform magnetic, electro-transport, and thermo-electric measurements under precise thermal conditions. It also allows the researcher to use different automated modes of operations such as the alternating current (AC) measurement system, heat capacity measurement system and ultra-low field mode. The magnetic field can be applied up to ± 16 Tesla and temperatures range form 1.9-400 K with ± 0.5 % accuracy. The change in temperature can of rates that range from 0.01 K/min up to 12 K/min. Stability for temperatures ≤ 10 K is ≤ 0.2% and for temperatures ≥ 10 K is ≥ 0.2 %. The PPMS system consists of Dewar, probe, top-plate assembly, probe lifting assembly, electronics cabinet, PPMS controller and a vacuum pump. The system's probe is shown in Figure 3.6. The probe is one of the most important parts in the system because it is home for the basic temperature-control hardware, the superconducting magnet, the Helium-level meter, the gas lines and various electrical connections as well as the sample chamber. The probe is also immersed in the liquid Helium bath inside the Dewar.

The sample chamber connects to the heater and thermometers; it is constructed from copper to attain the temperature uniformity. There is a space between the inner vacuum and the sample chamber called the cooling annulus where Helium can be pulled in and out to cool or warm the sample chamber. For magnetic measurement a sensitive vibrating sample magnetometer is used to vibrate the sample mechanically via piezoelectric motor inside an inductive coil. The induced current in the coil is measured to and interpreted into magnetic

properties. The main software associated with the PPMS system is MultiVu which is a Windows-based application used to obtain data and to operate the PPMS controller. Command sequences that suits each measurement can be edited and executed through the software.

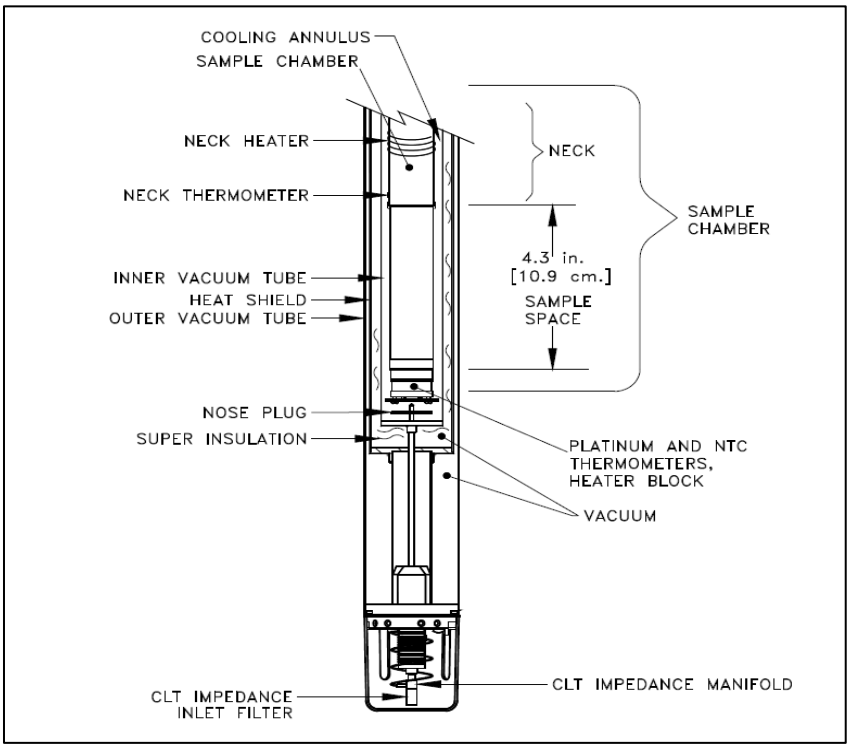

Figure 3.17. A Cross sectional of PPMS Probe

CHAPTER 4

Study of FeNi Films Prepared from Alloy Target

This chapter presents all the results and data collected. The results are also interpreted and discussed in detail. More information on the characterization processes is provided along with the results. The film thickness and growth rates were estimated by a profilometer and SEM was used to verify the results. A study of the topography of the films was provided by the aid of an AFM technique. The magnetic properties were performed on a Quantum design PPMS. The film structure was evaluated by XRD. The principal goal of this research is to form $L1_0$ ordered FeNi thin films/ nanoparticles with high coercivities. Accordingly, this work can be divided into three main stages. The start point was a target made by ball milling with a Fe and Ni 50-50% composition. In $L1_0$ structure, if the thin film consists of only $L1_0$ phase the composition will be 50-50% because of the way atoms place themselves in the subsequent layers. To take advantage of the PLD stoichiometric ability to transform the target structure into the substrate, this target was used to promote the $L1_0$ growth of the FeNi on the substrate. All the parameters involved in the PLD processes affect the resulting thin films and their structure. To optimize these parameters, depositions were conducted by varying one parameter at a time and keeping the others fixed. The deposition temperature is of great importance as it plays a big role in the resulting structure of the thin films as mentioned before in Chapter 3. In the first stage, depositions were carried under substrate temperatures of room temperature (about 25°C), 200°C, 400°C, 600°C and Liquid N_2 temperature (about -196°C). A single layer of $Fe_{50}Ni_{50}$ was deposited on bare Silicon and Sapphire substrates. Fe/ Ni multilayers were also deposited from Fe and Ni separate targets under the same temperatures and same PLD parameters; the multi-

target characteristic of the PLD system was employed in these depositions. Schematics of layers of the Fe/Ni multilayers and $Fe_{50}Ni_{50}$ single layer are illustrated in Figure 4.1.

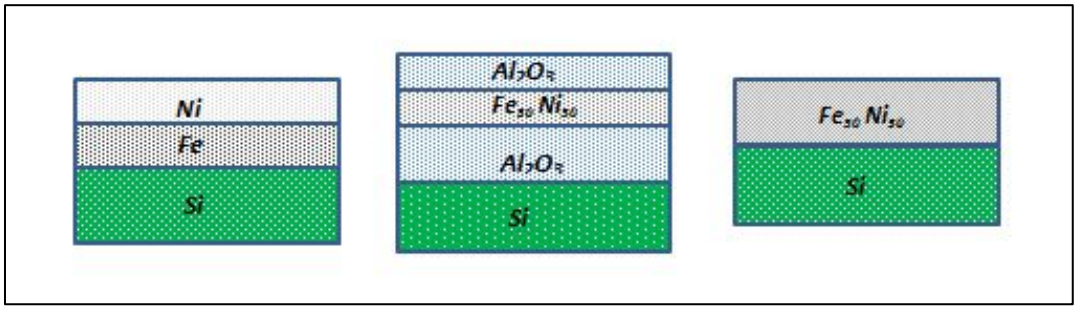

Figure 4.1. Samples Structures

It is very important also to study the magnetic properties of materials when embedded in non-magnetic matrices. The $Fe_{50}Ni_{50}$ nanoparticles were embedded in Al_2O_3 non-magnetic matrix as shown in Figure 4.1. These samples were analyzed using SEM, EDX, AFM and PPMS.

4.1 Film Thickness Estimation

The thickness of the films was estimated by SEM images of the sample cross-sectional perpendicular to the surface as shown in Figure 4.2 and 4.3. Samples deposited at different substrate temperatures did not show a significant change in film thickness.

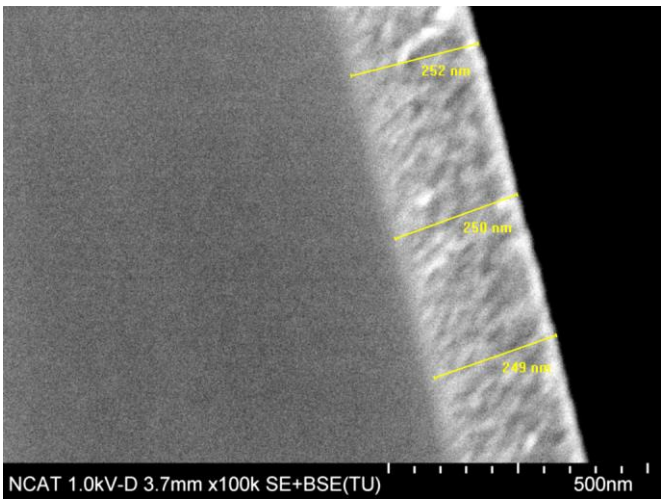

Figure 4.2. SEM Image of Film Thickness

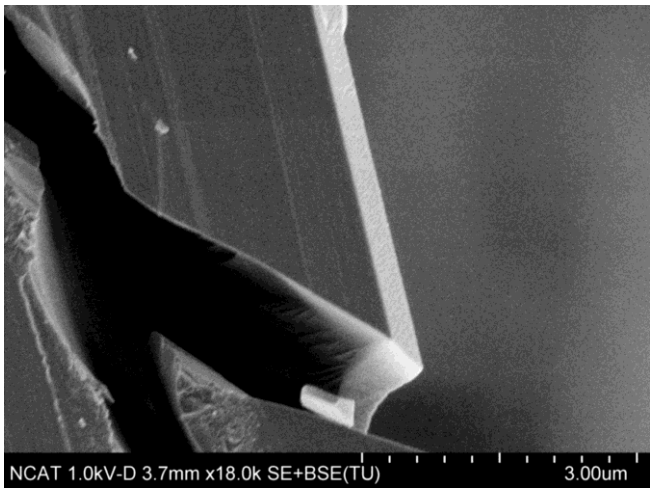

Figure 4.3. Cross sectional view perpendicular to the sample surface SEM image

4.2 Scanning Electron Microscopy

The morphology and microstructure of the films fabricated by PLD were studied by scanning electron microscopy. Figure 4.4 shows the sample surface at a very low magnification of the $Fe_{50}Ni_{50}$ single layer deposited at room temperature. The formation of particle droplets on the film is a typical behavior of the PLD system.

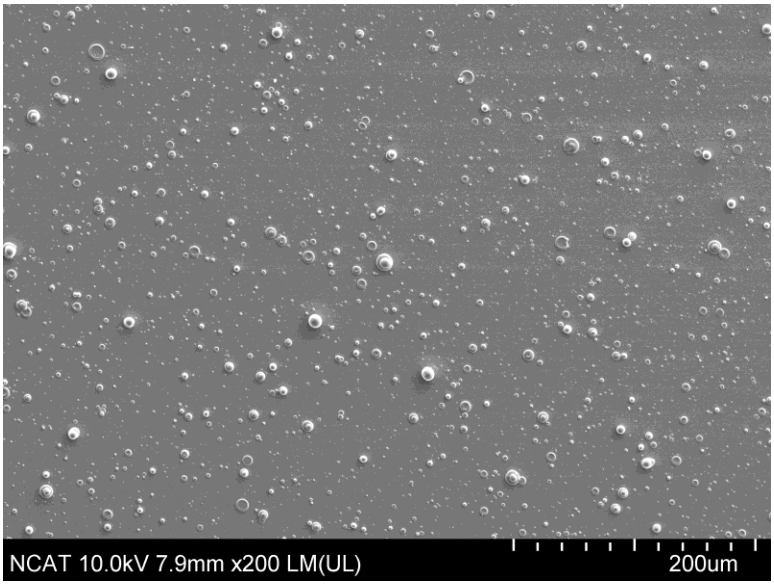

Figure 4.4. Sample 47 $Fe_{50}Ni_{50}$ deposited at room temperature on Silicon.

The SEM images taken at high magnifications show smooth amorphous films for samples deposited at liquid N_2 temperature and room temperature versus those deposited at higher temperatures as shown in Figure 4.5. Samples of $Fe_{50}Ni_{50}$ single layers and Fe/Ni deposited at 200°C show some formation of structure on the surface, although they are not distinguished grains but properly post annealing will result in very small grain sizes. SEM image under very high magnification for sample deposited at 200°C is shown in Figure 4.6.

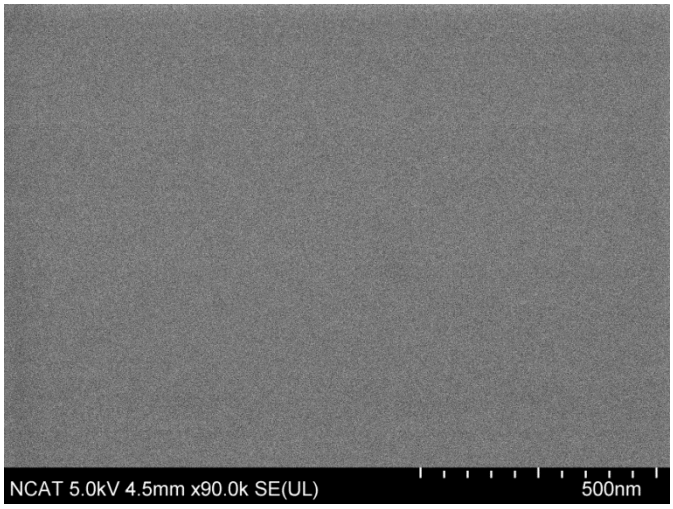

Figure 4.5. SEM image of sample 52 Fe/Ni multilayers deposited at room temperature on Silicon

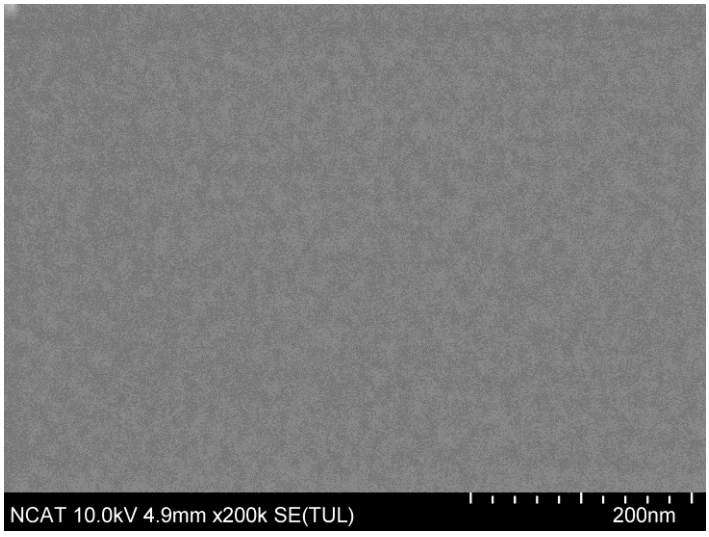

Figure 4.6. SEM image of sample 53 Fe/Ni multilayers deposited at 200°C on Silicon

$Fe_{50}Ni_{50}$ single layers and Fe/Ni multilayers deposited at 400°C showed visible grains at lower magnifications as shown in Figure 4.7. The growth of grains at higher temperatures can be attributed to the mobility of high energized atoms at the surface due to substrate temperature. $Fe_{50}Ni_{50}$ films deposited at 600°C have uniform grain distribution; Fe/Ni films also show uniform grains but the bright and dark grains attributes to the two deposited materials as shown in Figure 4.8. All $Fe_{50}Ni_{50}/Al_2O_3$ samples scanned by SEM showed smooth surfaces.

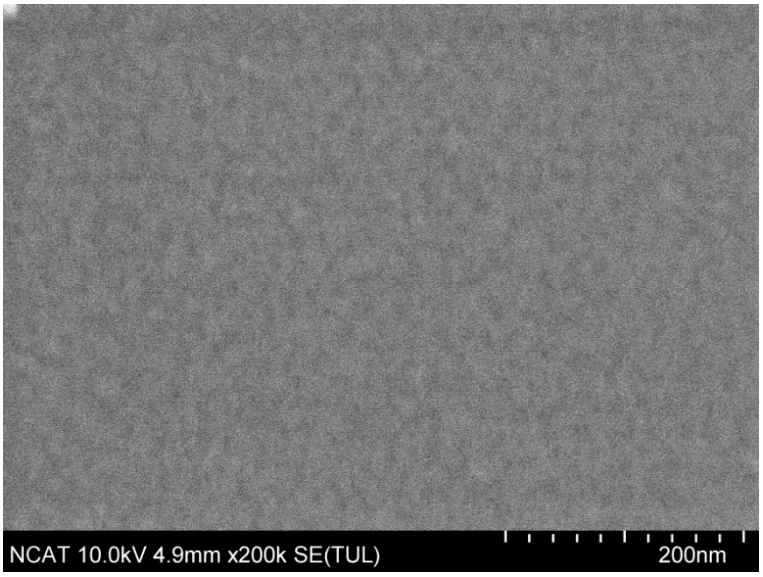

Figure 4.7. SEM image of sample 49 $Fe_{50}Ni_{50}$ deposited at 400°C on Silicon

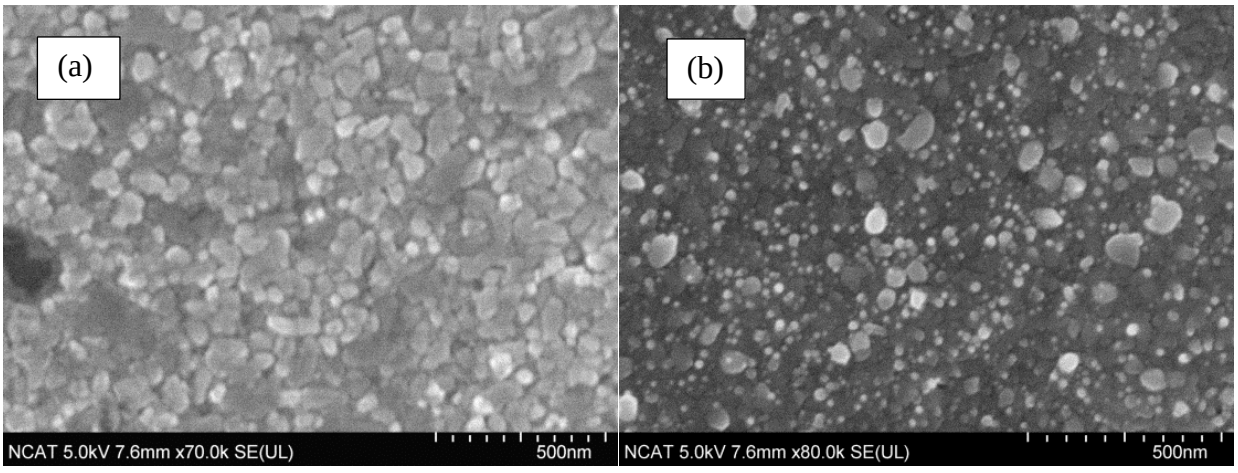

Figure 4.8. SEM of (a) sample 50 and (b) sample 55

The effect of the substrate on grain distribution was also studied by comparing films from the same deposition on Silicon and Sapphire. The SEM image of Sample 55 deposited on Silicon (100) and Sapphire show different grain distribution as shown in Figure 4.9. On the Sapphire, the film shows a crystallized island growth compared to the distinguished grains on Silicon substrates and that might be attributed to lattice matching.

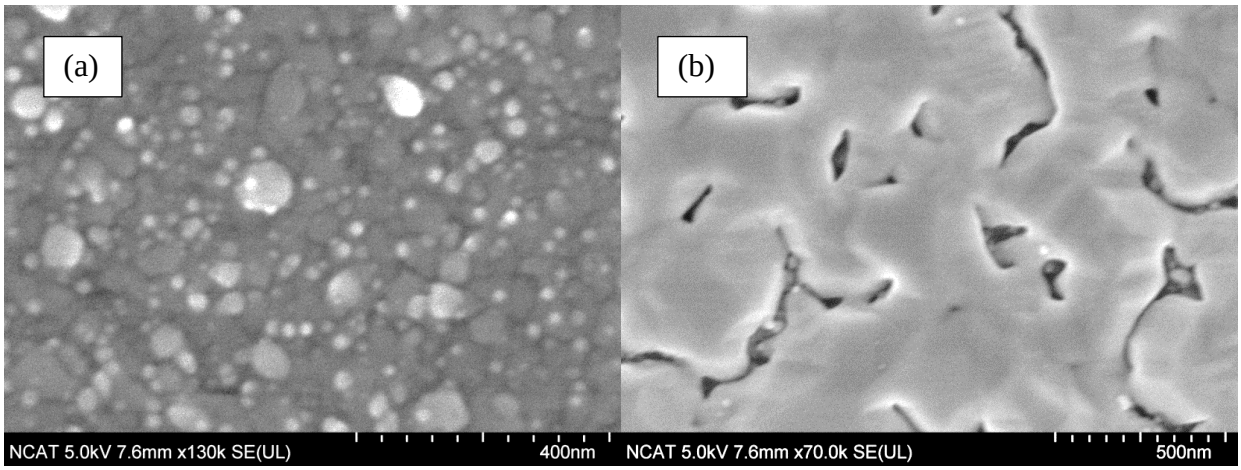

Figure 4.9. SEM images of sample 55 deposited on (a) Silicon and (b) Sapphire

4.3 Atomic Force Microscopy

Surface topography and particle analysis was performed using atomic force microscopy. The Samples chosen for the analysis were deposited at room temperature, 600°C and Liquid N_2 temperature. Figures 4.10-4.12 presents the topographical images with areas 1.2 x 1.2 μm^2 of the $Fe_{50}Ni_{50}$, Fe/Ni and $Fe_{50}Ni_{50}/Al_2O_3$ samples, respectively. The particle size (height and diameter) for samples prior and after heat treatment are presented in Figure 4.13. The AFM images show that some of the films have shinny large particles that are likely to be metal droplets from the target known to be produced by the PLD.

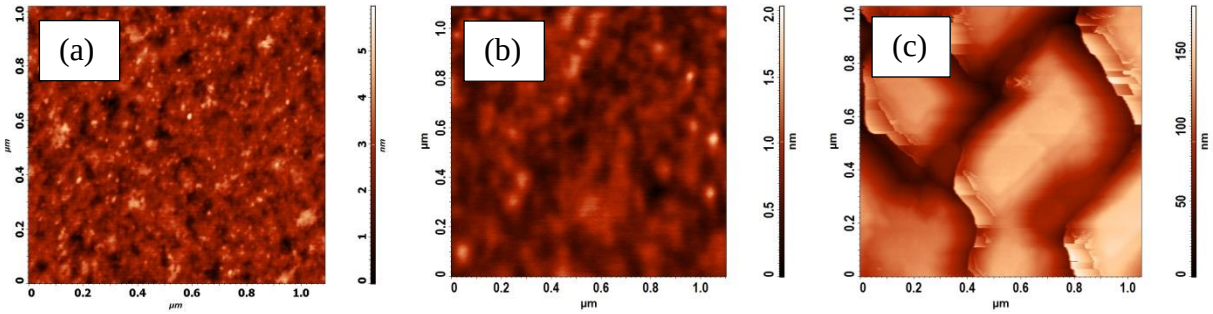

Figure 4.10. AFM images of $Fe_{50}Ni_{50}$ deposited at (a) room temperature, (b) liquid N_2 temperature and (c) 600°C.

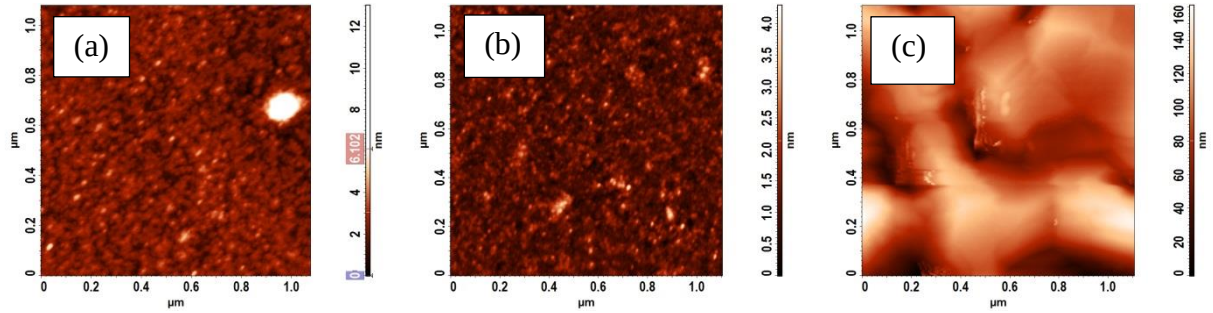

Figure 4.11. AFM images of Fe/Ni deposited at (a) room temperature, (b) liquid N_2 temperature and (c) 600°C.

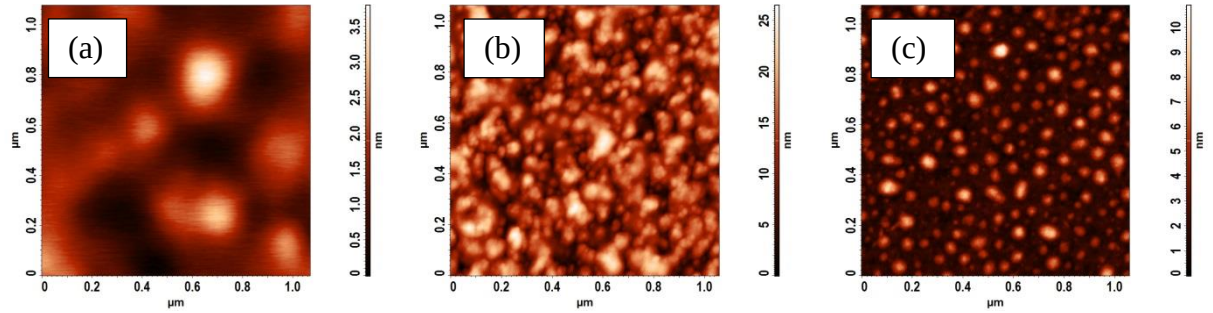

Figure 4.12. AFM images of $Fe_{50}Ni_{50}/Al_2O_3$ at (a) room temperature, (b) liquid N_2 temperature and (c) 600°C.

AFM analysis was performed on samples deposited at liquid N_2 temperature, room temperature and 600°C. Samples deposited at 200°C and 400°C are estimated to follow the same behavior of samples deposited at room temperature and 600°C respectively.

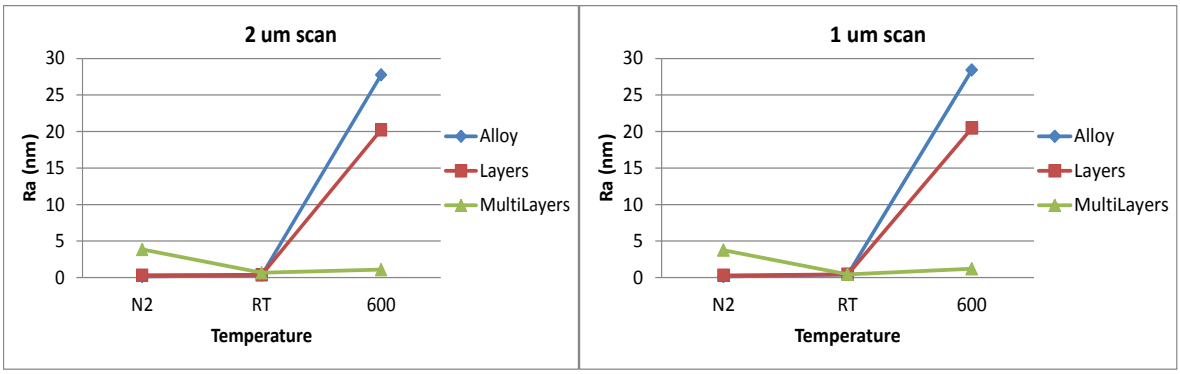

Figure 4.13. The surface roughness versus deposition temperature at (a) 2 μm and (b) 1 μm scan.

The surface roughness calculations verified the positive proportional relationship between the surface roughness and deposition temperatures in $Fe_{50}Ni_{50}$ and Fe/Ni thin films. Films deposited at Liquid N_2 are slightly smoother than those deposited at room temperature. The extreme cooling in the case of $Fe_{50}Ni_{50}/Al_2O_3$ multilayers promoted higher surface roughness compared to depositions at room temperature and 600°C. The presence of Al_2O_3 obviously prevented the growth of $Fe_{50}Ni_{50}$ crystals at high temperatures. Although AFM images are not reliable as an analysis tool for the morphology of the films but they are in good agreement with the SEM images. Samples of $Fe_{50}Ni_{50}$ and Fe/Ni thin films deposited at lower temperatures are amorphous and sample deposited at higher temperature show crystal formations.

4.4 Physical Properties Measurement System

Magnetic measurements were obtained by PPMS. A sequence has been created to automate the PPMS operation and record sample measurement data. In the sequence parameters such as temperature and field were specified for each measurement. The M-H curves of the deposited films were obtained at 10K, 100K, 200K and 300K at an external applied field of 10 Tesla. An example of sequence is shown in Figure 4.14.

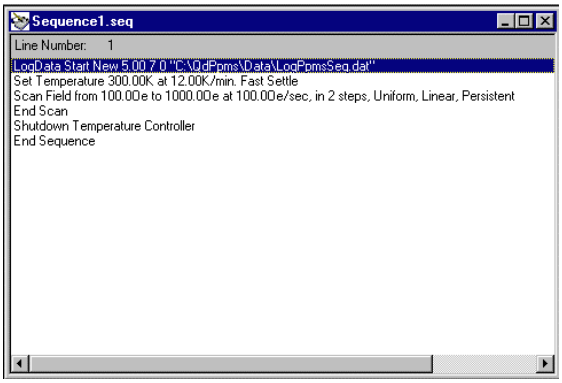

Figure 4.14. A sequence window as it appears in the Multivu software screen

In this dissertation, Ku calculations were not included because the condition of single crystal growth was not met by the FeNi thin films fabricated; the films were either amorphous for samples deposited at low temperatures and polycrystalline for sample deposited at higher temperatures. The M-H curves for $Fe_{50}Ni_{50}$ single layer thin films deposited at room temperature, 200°C, 400°C, and 600°C are obtained and presented in Figure 4.15-4.16. Saturation magnetization and remanent magnetization values were extracted from the hysteresis loop. The coercivity was calculated from loop intersection on magnetic field axis following equation 4.1.

$$H_c = \frac{H_{+c} + |H_{-c}|}{2} \qquad (4.1)$$

The narrow loops in all of them are following the trend of the typical loop of a soft magnetic material. Coercivities of soft FeNi films are as low as several Oersteds. Measured coercivities of $Fe_{50}Ni_{50}$ thin films at different deposition temperatures were from 43.83 to 21.98 Oe. Fe/Ni multilayers have coercivities from 10.92 to 59.15 Oe. Noting that Fe50Ni50 deposited at liquid N2 have coercivity of 0 Oe at all measurement temperatures.

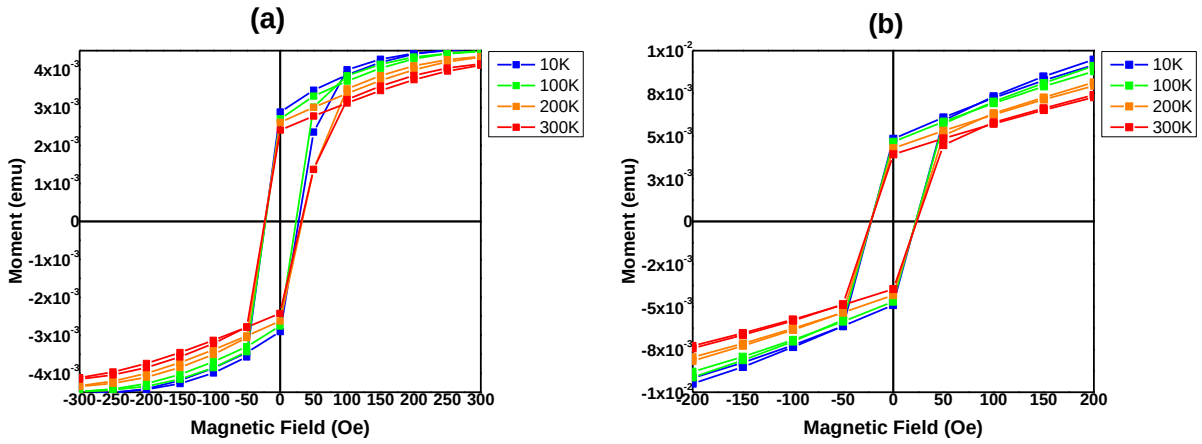

Figure 4.15. M-H hysteresis loops of $Fe_{50}Ni_{50}$ deposited at (a) room temperature and (b) 200°C

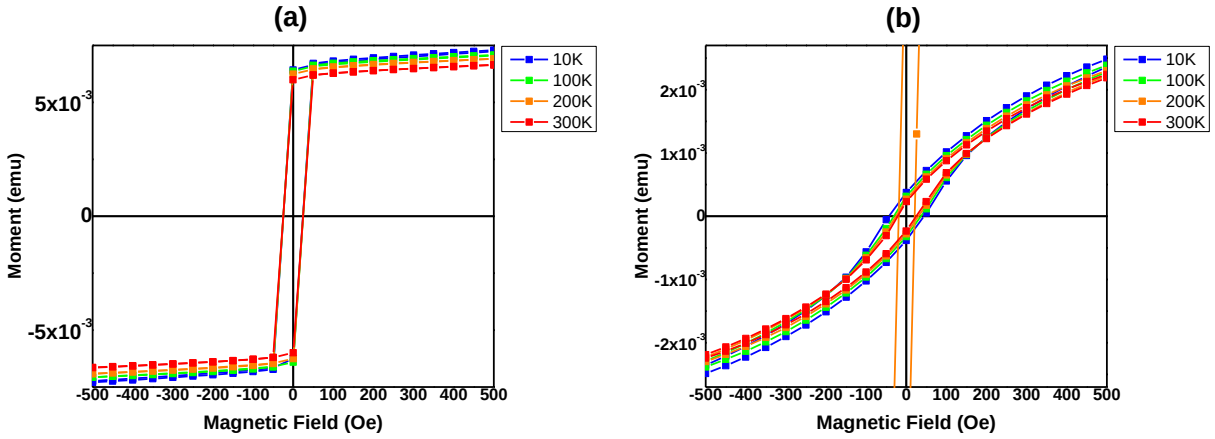

Figure 4.16. M-H hysteresis loops of $Fe_{50}Ni_{50}$ deposited at (a) 400°C and (b) 600°C.

The samples deposited at liquid N_2 are superparamagnetic as shown in Figure 4.17. Based on the definition of a superparamagnetic material, such materials have very small grain sizes (small particles) and the spins are not stable and change direction often. The rapid condensations that occur during this very low temperature allows the material solidify in very small particle sizes 1-2 nm. Magnetic properties of FeNi films deposited at liquid N2 were not reported in previous research. The higher deposition temperatures did not have a significant effect on the coercivity of the films; very slight increase in coercivity was observed. Also films

deposited from $Fe_{50}Ni_{50}$ alloys were not in favor of the films deposited from Fe and Ni targets. In fact, the films exhibited almost the same hysteresis behavior. Although at higher temperatures coercivities of Fe/Ni multilayers are slightly higher; this attributes to the Fe-Ni 50 -50 % atomic composition of the multilayers which were analyzed by EDX versus the $Fe_{50}Ni_{50}$ which exhibited an estimated Fe-Ni of 45-55 %. It was reported in literature that higher Fe content influence magnetic properties of FeNi thin films. M-H hysteresis loops for Fe/Ni multilayers are shown in Figures 4.18-4.20. All coercivities are calculated and presented in Appendix B.

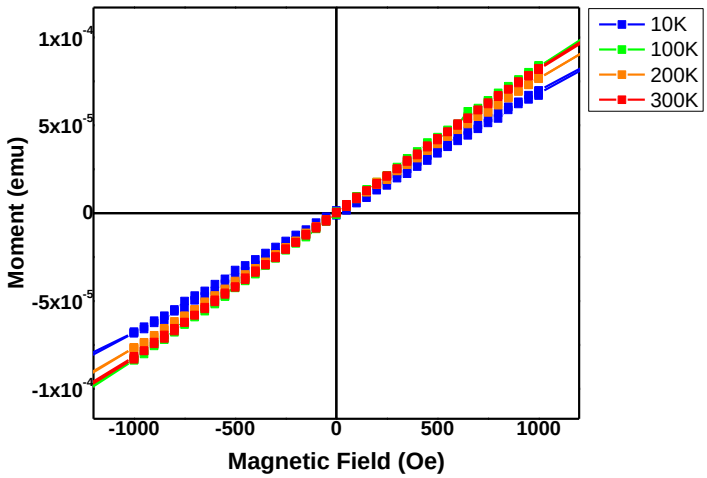

Figure 4.17. M-H hysteresis loops of $Fe_{50}Ni_{50}$ deposited at liquid N_2 temperature (sample 51)

Remanence ratios ($M_r/M_{s)}$ indicate a measure of magnetic interactions between particles in the film. A ratio less than 0.5 indicate magnetostatic coupling between particles while a ratio greater than 0.5 indicate exchange coupling between particles. M_r/M_s extracted from the M-H hysteresis loops of Fe/Ni multilayers are very high compared with $Fe_{50}Ni_{50}$ as shown in Table 4.1.

Table 4.1

Remanence ratio for $Fe_{50}Ni_{50}$ and Fe/Ni thin films

Sample #	Material	Deposition Temperature	M_r/M_s
47	$Fe_{50}Ni_{50}$	RT	0.467
52	Fe/Ni	RT	0.940

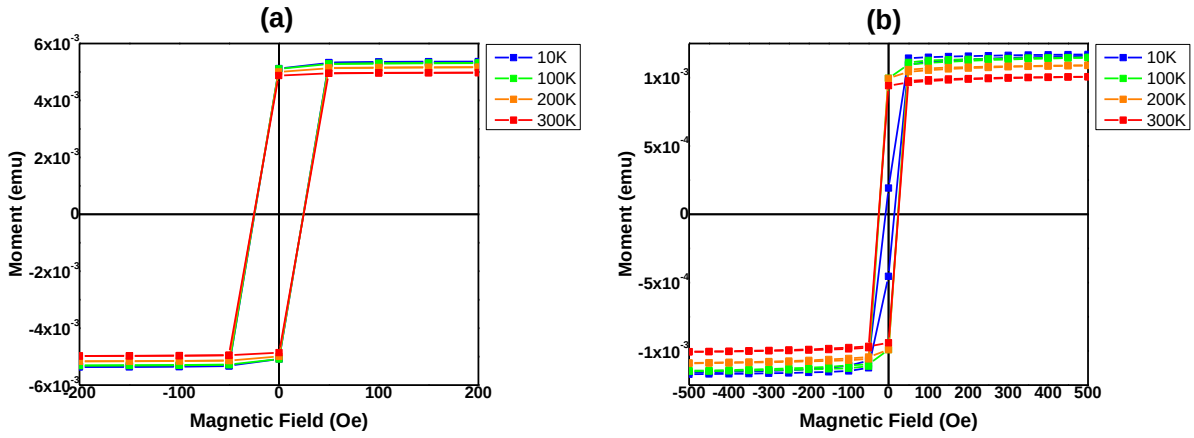

Figure 4.18. M-H hysteresis loops of Fe/Ni multilayer thin films deposited (a) at room temperature and (b) 200°C.

Nonmagnetic spacer layers have been employed in previous studies by Dr. Kumar group to observe the exchange decoupled nanoparticles. In this study Al_2O_3 was used as a spacer layer to study the effect of a nonmagnetic layer on the magnetic behavior of $Fe_{50}Ni_{50}$ nanoparticles. The M-H hysteresis loops for $Fe_{50}Ni_{50}$/ Al_2O_3 multilayers are shown in Figures 4.21 and 4.22. From AFM analysis of the sample deposited at higher temperature it is obvious that the Al_2O_3 acted on separating and restricting the growth of the particles and as result the magnetic interactions were affected. As a result, the film deposited at 600°C show superparamagnetic behavior, which is rather different than the other ferromagnetic films studied in this work. The

nanoparticles deposited at 600°C fall in the superparamagnetic region of the particle size vs coercivity phase diagram shown earlier in Figure 2.10. The hysteresis loops obtained for the films behaved in a very inconsistent way. Only the measurement taken at 10 K show wider loops for samples deposited at room temperature and 400°C. Decreasing the spacer layer thickness have a major effect on magnetic behavior of nanoparticles.

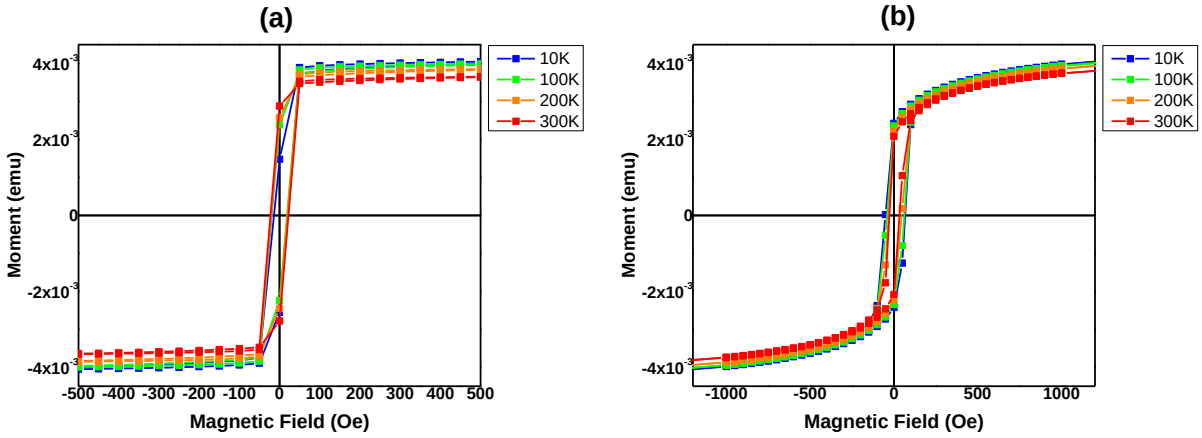

Figure 4.19. M-H hysteresis loops of Fe/Ni multilayer thin films deposited at (a) 400°C and (b) 600°C.

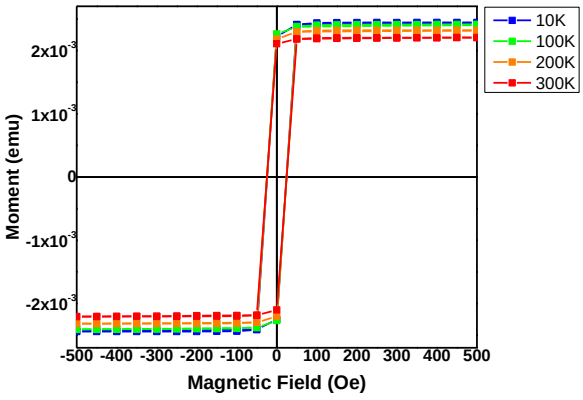

Figure 4.20. M-H hysteresis loops of Fe/Ni multilayer thin films deposited at liquid N_2 temperature

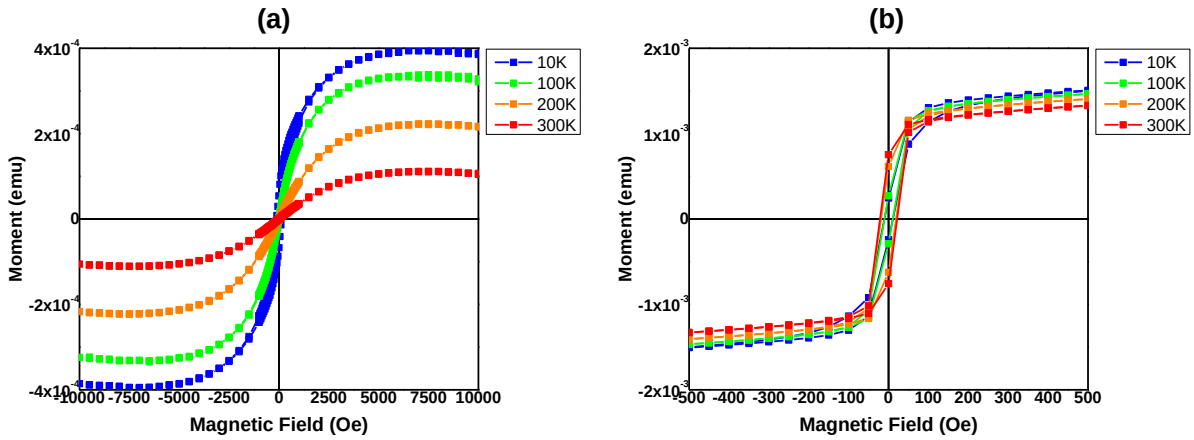

Figure 4.21. M-H hysteresis loops of $Fe_{50}Ni_{50}/Al_2O_3$ multilayers deposited at (a) room temperature and (b) 200°C.

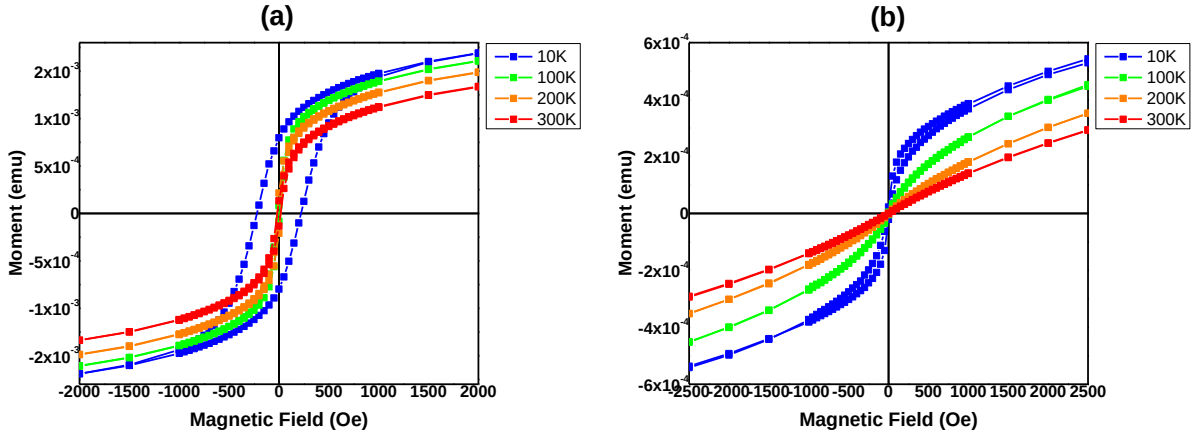

Figure 4.22. M-H hysteresis loops of $Fe_{50}Ni_{50}/Al_2O_3$ multilayers deposited at (a) 400°C and (b) 600°C.

The presence of an $L1_0$ ordered FeNi structure was not detected from these magnetic measurements of the $Fe_{50}Ni_{50}$ thin films and Fe/Ni multilayers at different temperatures. The magnetic behavior was enhanced by adding a gold buffer layer to promote uniform small grain growth and post annealing.

CHAPTER 5

Influence of Gold Catalyst on FeNi Thin Films

After reviewing published literature in thin film magnetic enhancement for data storage devices, Gold was suggested as a catalyst to improve grain distribution and to produce small grain sizes. Two sets of samples were deposited at room temperature and 600˚C; the first set was deposited from $Fe_{50}Ni_{50}$ target with an under layer of Gold, the second was deposited from Fe and Ni targets. All depositions were on Silicon (100) substrates. Before each deposition, experiments were carried with masked substrates to determine the growth rate under the specified PLD conditions. The growth rate depositions were conducted with Au, Fe, Ni and $Fe_{50}Ni_{50}$ targets. Masked samples were then scanned with the profilometer to measure the step caused by the thin film grown on the substrate.

All samples were then analyzed with PPMS, SEM, and XRD. Post annealing was performed in a vacuumed chamber at 600˚C for 1 hour. Sample structures are shown in figure 5.1.

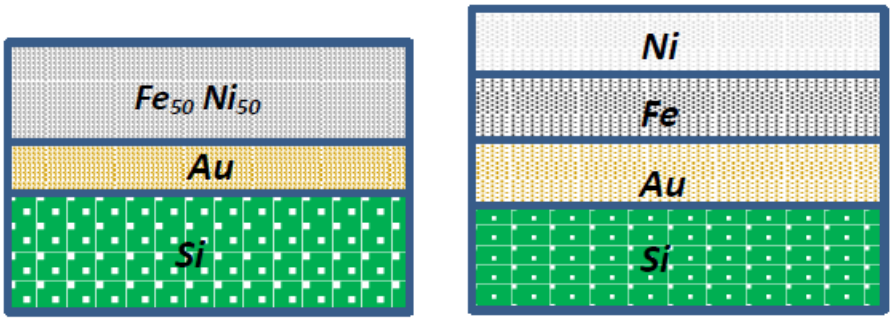

Figure 5.1. A schematic of samples with gold catalyst.

5.1 Film Thickness Estimation

Growth rates for all masked substrates were estimated using the surface profiler; data are used to set the no of pulses for each deposition. The deposition rates were then calculated from the following equation.

$$Deposition\ rate = \frac{Average\ film\ thickness}{No.\ of\ \ laser\ \ pulses} \qquad (5.1)$$

5.2 Scanning Electron Microscopy

The morphology and microstructure of the films with Au catalyst were studied by scanning electron microscopy. Figure 5.2 shows the difference in morphology between $Fe_{50}Ni_{50}$ samples deposited at 600˚C without Au and with Au. Adding Au under layer improved the uniformity of the grain distribution and decreased the grain sizes. In $Fe_{50}Ni_{50}$ sample the grain distribution of the film is more uniform than the sample deposited from Fe/Ni multilayers as shown in Figure 5.3.

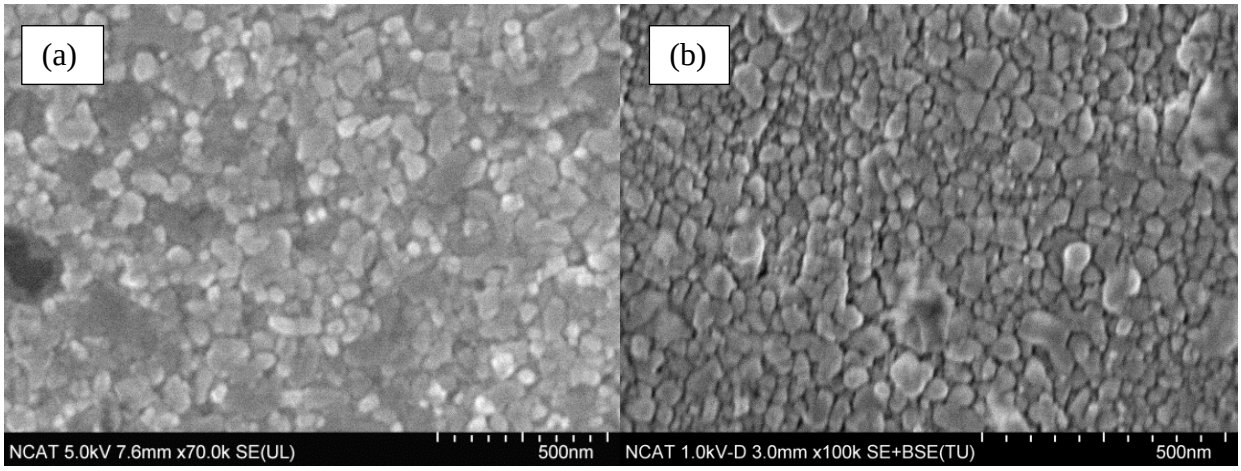

Figure 5.2. SEM images of two samples (a) without and (b) with a gold catalyst.

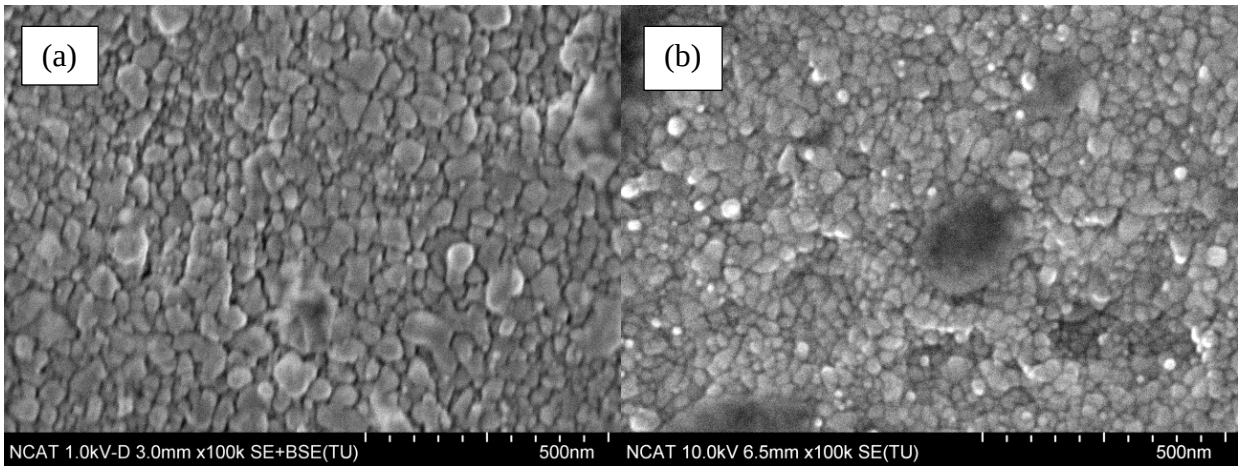

Figure 5.3. SEM images showing the difference between depositing from (a) $Fe_{50}Ni_{50}$ and (b) Fe/Ni.

The effect of annealing is also illustrated by the SEM images in a clear manner. Post annealing changed the microstructure of all samples significantly as shown in Figure 5.4-5.7. Sample 70 of Au/$Fe_{50}Ni_{50}$ deposited at room temperature was showing a structure that was not well clear and higher magnification limit was reached. Annealing promoted grain and island formation. The SEM images of sample 73 Au/$Fe_{50}Ni_{50}$ deposited at 600°C indicate that annealing did not have a big influence on the grain distribution but it enhanced the uniform grain size.

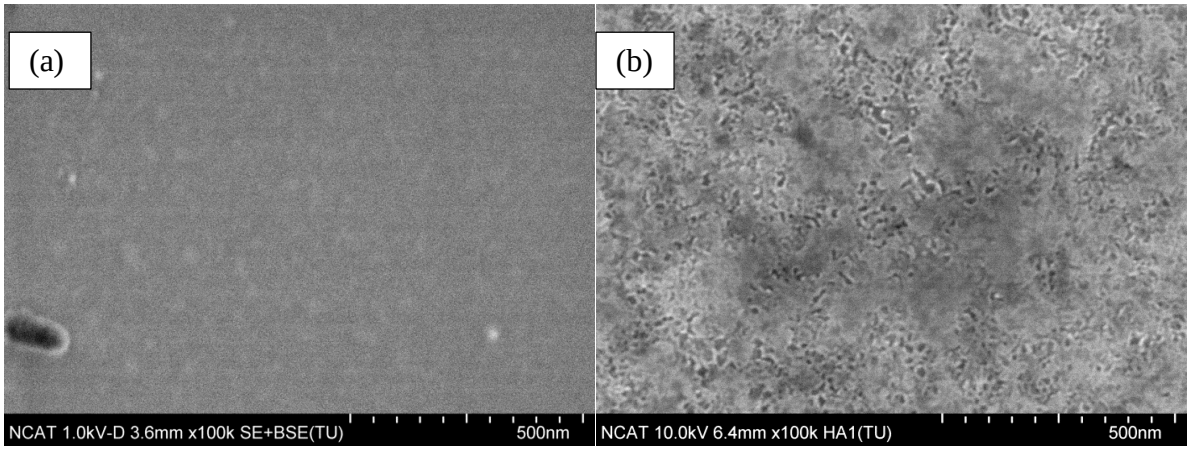

Figure 5.4. Sample 70 $Fe_{50}Ni_{50}$ deposited at room temperature (a) before and (b) after annealing.

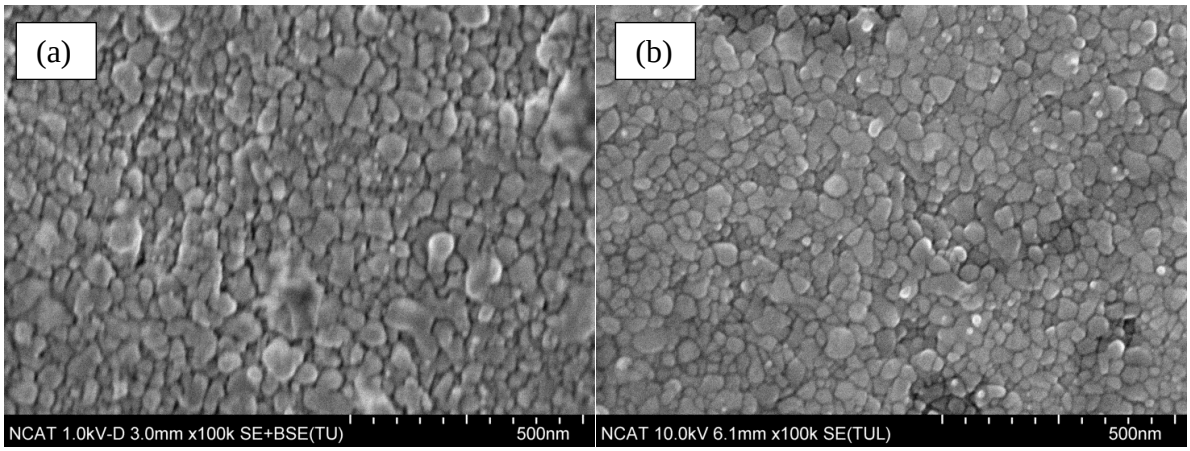

Figure 5.5. Sample 73 $Fe_{50}Ni_{50}$ deposited at 600˚C (a) before and (b) after annealing.

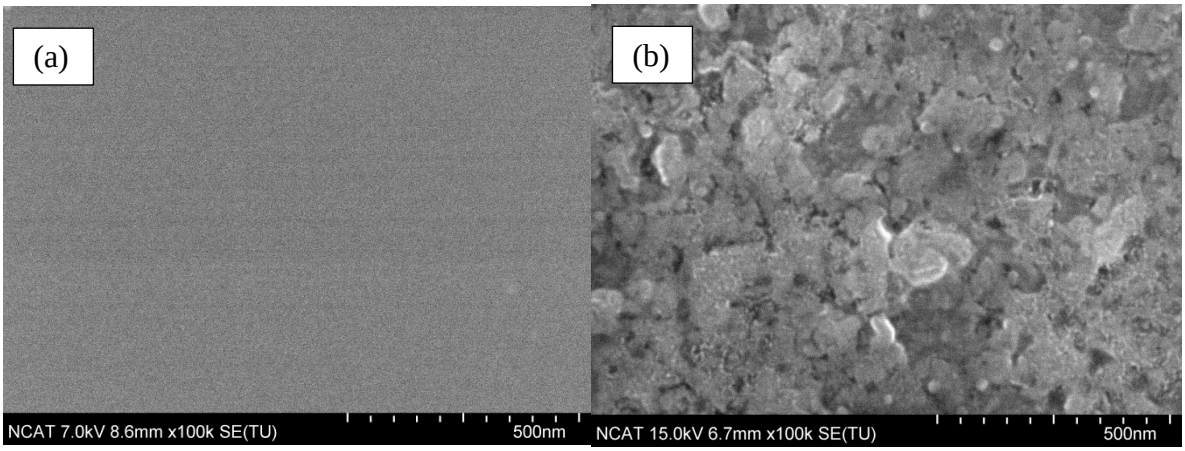

Figure 5.6. SEM image of sample 74 Fe/Ni deposited at room temperature (a) before and (b) after annealing.

In Figure 5.6, Sample 74 Au/Fe/Ni deposited at room temperature shows an enormous change in the film morphology. The as deposited are amorphous films while the post annealed have grain structures. Sample 75 Au/Fe/Ni deposited at 600°C followed the same trend as sample 73, annealing increased the grain size uniformity.

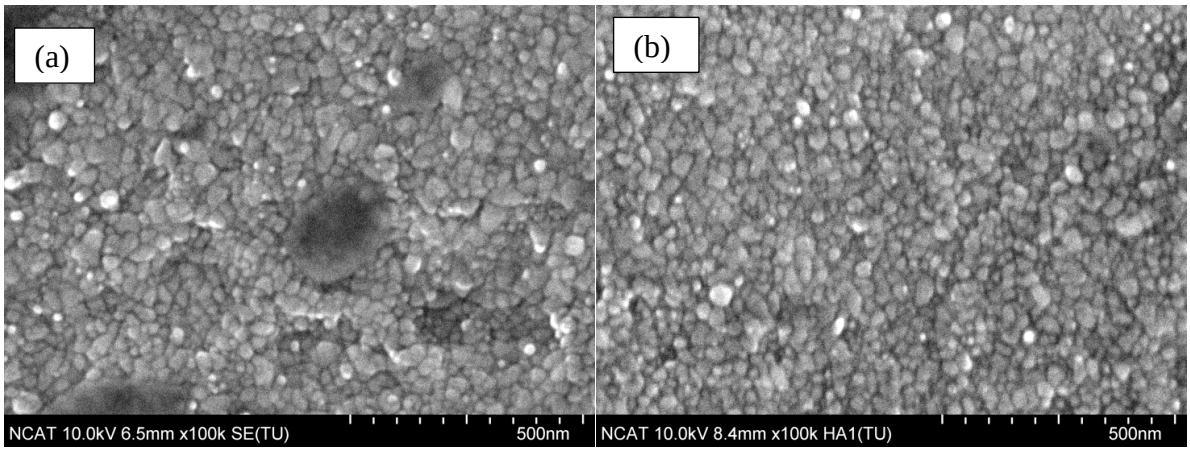

Figure 5.7. SEM image of sample 75 Fe/Ni deposited at 600˚C (a) before and (b) after annealing.

5.3 X-ray Diffraction

XRD patterns for Au/$Fe_{50}Ni_{50}$ thin films and Au/Fe/Ni multilayered films deposited at different temperatures are shown in Figure 5.8. $L1_0$-ordered FeNi alloy are denoted by the red dash lines. As deposited samples showed the fundamental peak of $L1_0$ at $2\theta = 50$ indicating the formation of the $L1_0$ FeNi ordered structure on the films. Sample 73 made of Au/$Fe_{50}Ni_{50}$ have a narrower higher peak of the bulk FeNi (110), as well as the bulk FeNi (002). Sample 74 Au/Fe/Ni and sample 70 Au/$Fe_{50}Ni_{50}$ as deposited show no peaks, implicating an amorphous film. The annealing changed the crystal structure of the films. The fundamental peak of $L1_0$ did not change, suggesting that the samples still have an $L1_0$ formation on their films. 2θ numbers for Fe. Ni, Au and FeNi alloys from the XRD data base are shown in Appendix A. The gold buffer layer was very thin and was not detected by the X-ray beam. The formation of the FeNi (002) indicates epitaxial growth due to the use of Au (001) under layer.

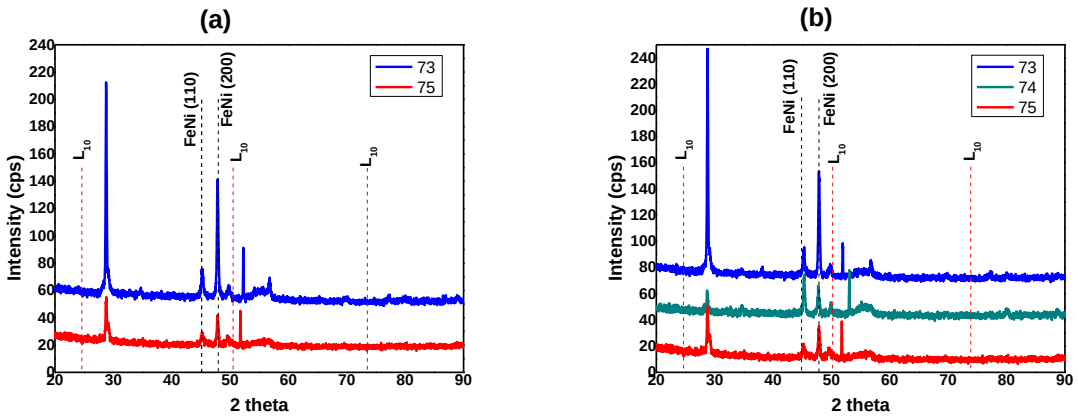

Figure 5.8. X-ray diffraction patterns for (a) as deposited samples and (b) annealed samples.

5.4 Magnetic Measurements

M-H hysteresis loops obtained by PPMS are shown in Figure (5.9-5.12). The coercivities of all the films with Gold under layer enhanced and increased by 200%. This is still not comparable to FePt, but it shows that embedding the Gold catalyst improved the crystallinity of the films and hence the magneto-crystalline anisotropy. Annealing did increase the coercivity of the samples deposited at room temperature. Again, in good agreement with the theory that states uniform grain distribution of small grain sizes increases coercivity.

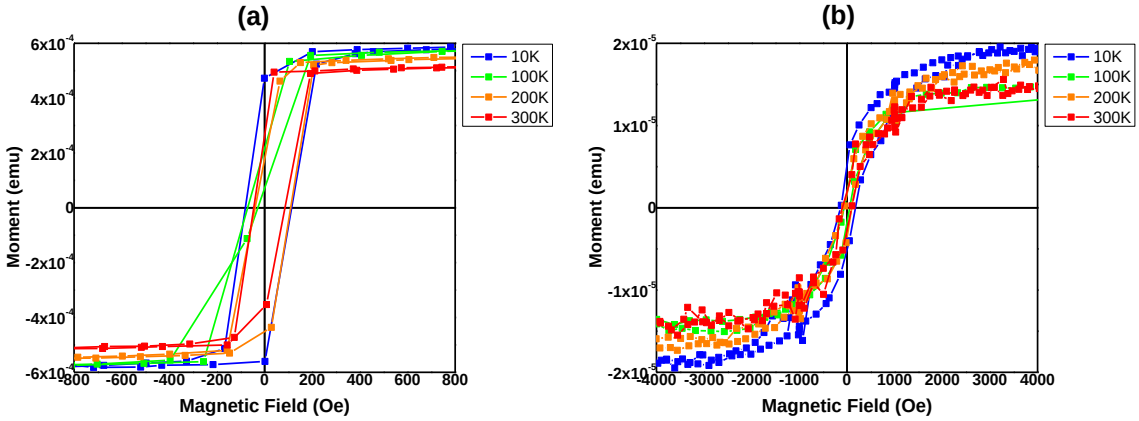

Figure 5.9. M-H hysteresis loop for sample 70 deposited from $Fe_{50}Ni_{50}$ at room temperature (a) before and (b) after annealing

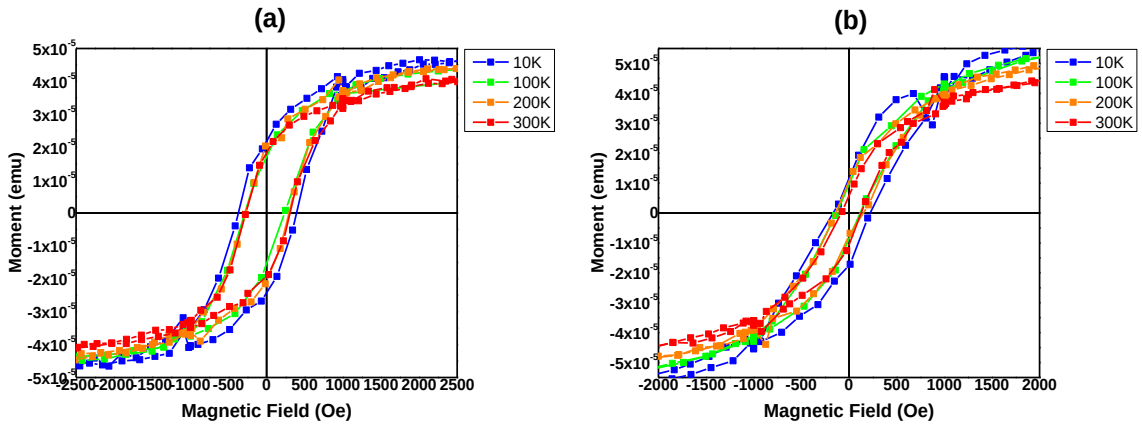

Figure 5.10. M-H hysteresis loop for sample 73 (a) before and (b) after annealing.

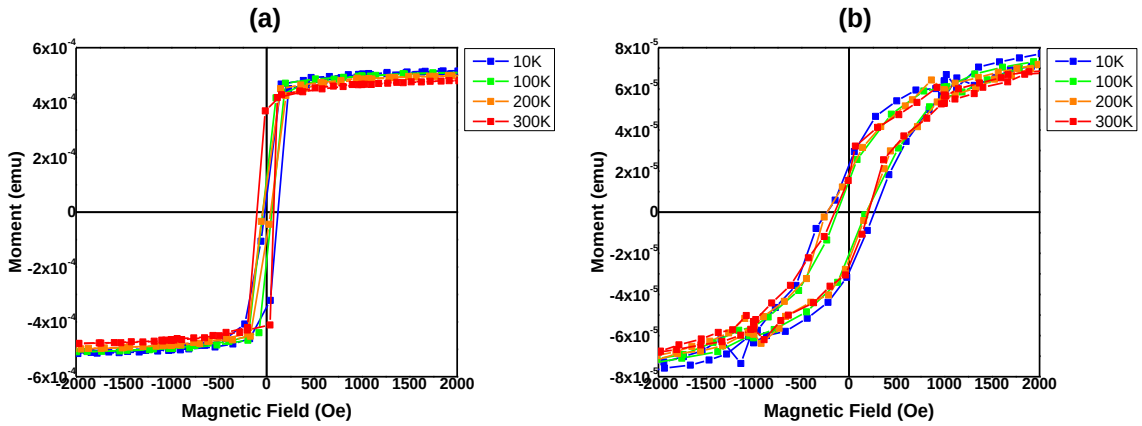

Figure 5.11. M-H hysteresis loop for sample 74 (a) before and (b) after annealing.

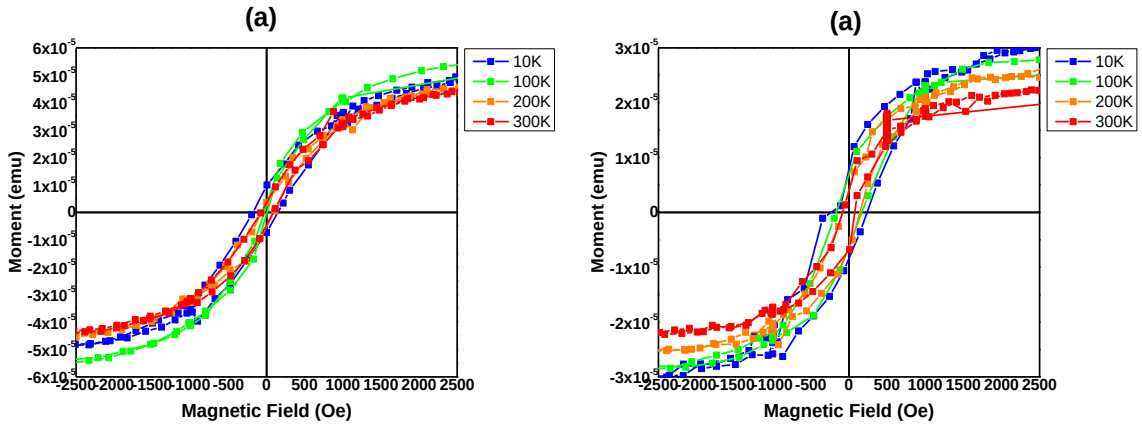

Figure 5.12. M-H hysteresis loop for sample 75 (a) before and (b) after annealing.

A comparison between coercivities deposited from $Fe_{50}Ni_{50}$ alloy target and Fe/Ni bulk targets and the influence of embedding a gold catalyst are shown in the curves obtained from calculation of coercivity from measured hysteresis loops (Figure 5.13 and 5.14).

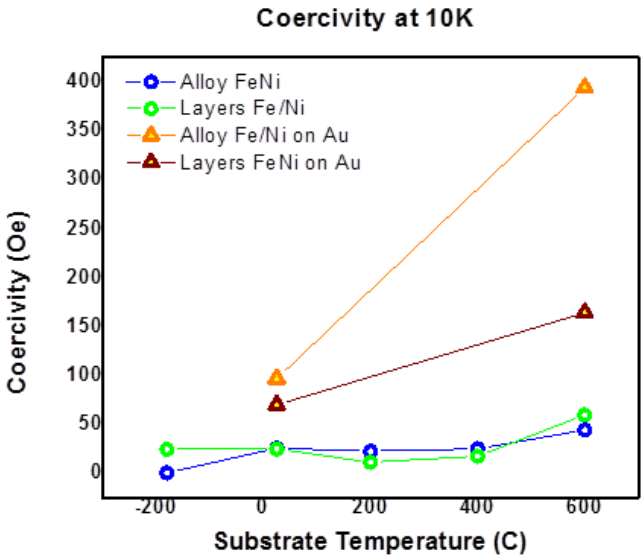

Figure 5.13. Coercivities at 10 K of $Fe_{50}Ni_{50}$, Fe/Ni, Au/$Fe_{50}Ni_{50}$, and Au/Fe/Ni thin films

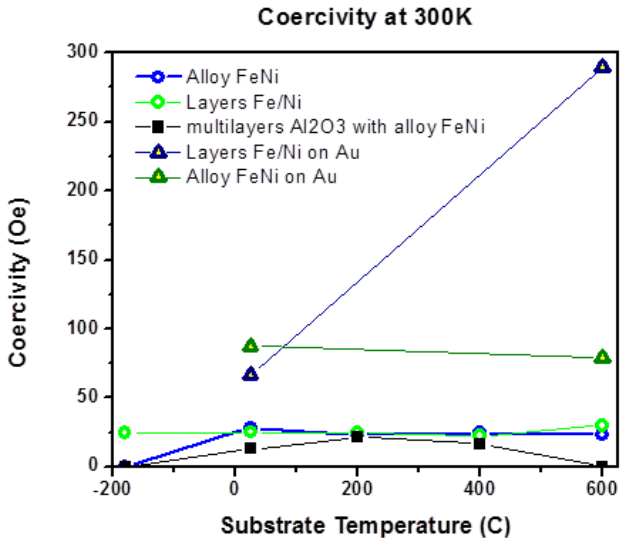

Figure 5.14. Coercivities at 300K of $Fe_{50}Ni_{50}$, Fe/Ni, $Fe_{50}Ni_{50}/Al_2O_3$, Au/$Fe_{50}Ni_{50}$, and Au/Fe/Ni thin films.

CHAPTER 6

Influence of Annealing on Magnetic Properties of $Fe_{50}Ni_{50}$ Thin Films

$Fe_{50}Ni_{50}$ thin films were annealed to examine the influence of annealing on magnetic properties. Annealing was conducted in a vacuumed chamber at 600˚C for 1 hour. As-deposited and annealed samples were characterized using AFM, SEM and PPMS.

6.1 Scanning Electron Microscopy

As-deposited and annealed samples were scanned using the SEM equipment. SEM images of sample 37 deposited at Liquid N_2 did not show any grain formation at high magnification indicating the film is amorphous as shown in Figures 6.1.In Figure 6.2, post annealed samples show very small grains not possible to see with the magnification limit reached. This result confirms the formation of fine grains which means the magneto crystalline-anisotropy is very high.

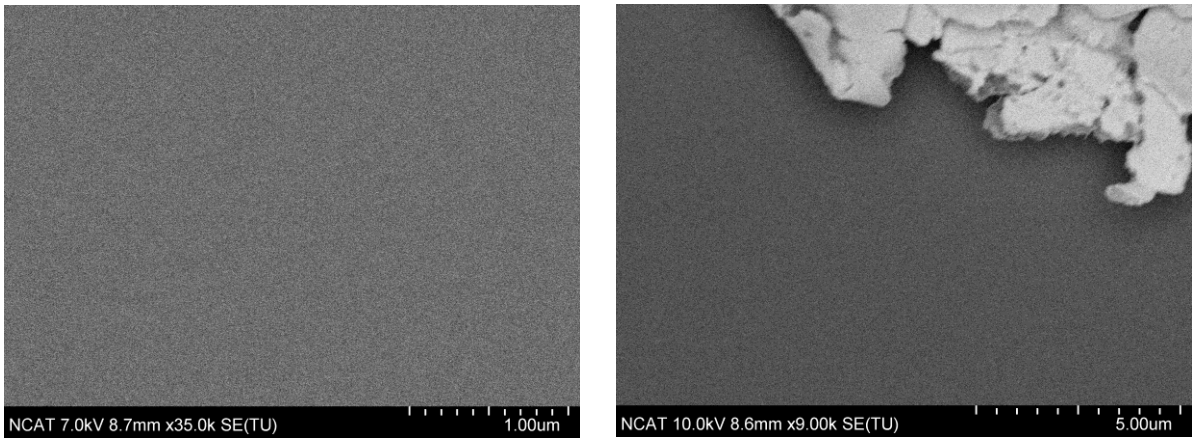

Figure 6.1. SEM images of sample 37 deposited at liquid N_2 at different magnifications.

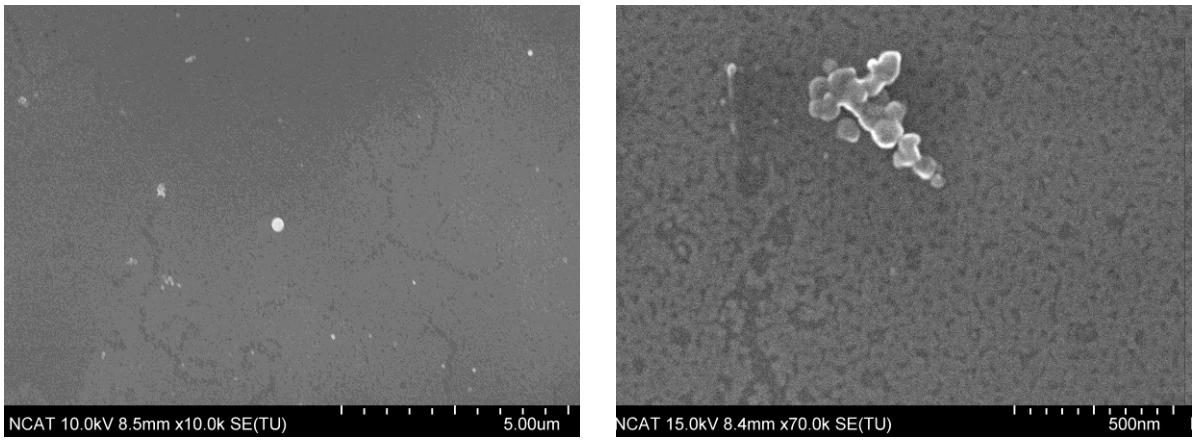

Figure 6.2. SEM image of sample 37 post annealing at different magnifications.

6.2 AFM Particles Analysis

Particles analysis was performed as described in Section 3.4 using Atomic force microscopy. Figure 6.3 present the topographical images with scan areas 0.6x0.6 μm^2 of the samples as -deposited and after heat treatment. The particle size (height and diameter) for samples prior and after heat treatment are presented in table 6.1 and Figure 6.4.

The AFM images show that some of the films have shinny large particles that are likely to be metal droplets from the target known to be produced by the PLD [90]. These droplets can be prevented by smoothing the target surface. Sample 37 deposited at liquid N_2 temperature have a very fine smooth surface but after annealing its average surface roughness increased from 1.471nm to 3.789nm, which is a 160 % increase. This increase is attributed to the Ostwald ripening phenomena during heating. The same behavior is observed for sample 32 deposited at room temperature, its average surface roughness increased from 1.41nm to 7.25nm, which is a 414% increase. The results clearly shown that sample 35 deposited at 600˚C produced stable uniformly sized and distributed particles. The as deposited film had a rough surface compared to the other two samples. Its average surface roughness only increased from 9.046nm to 9.979 with an increase of 10%.

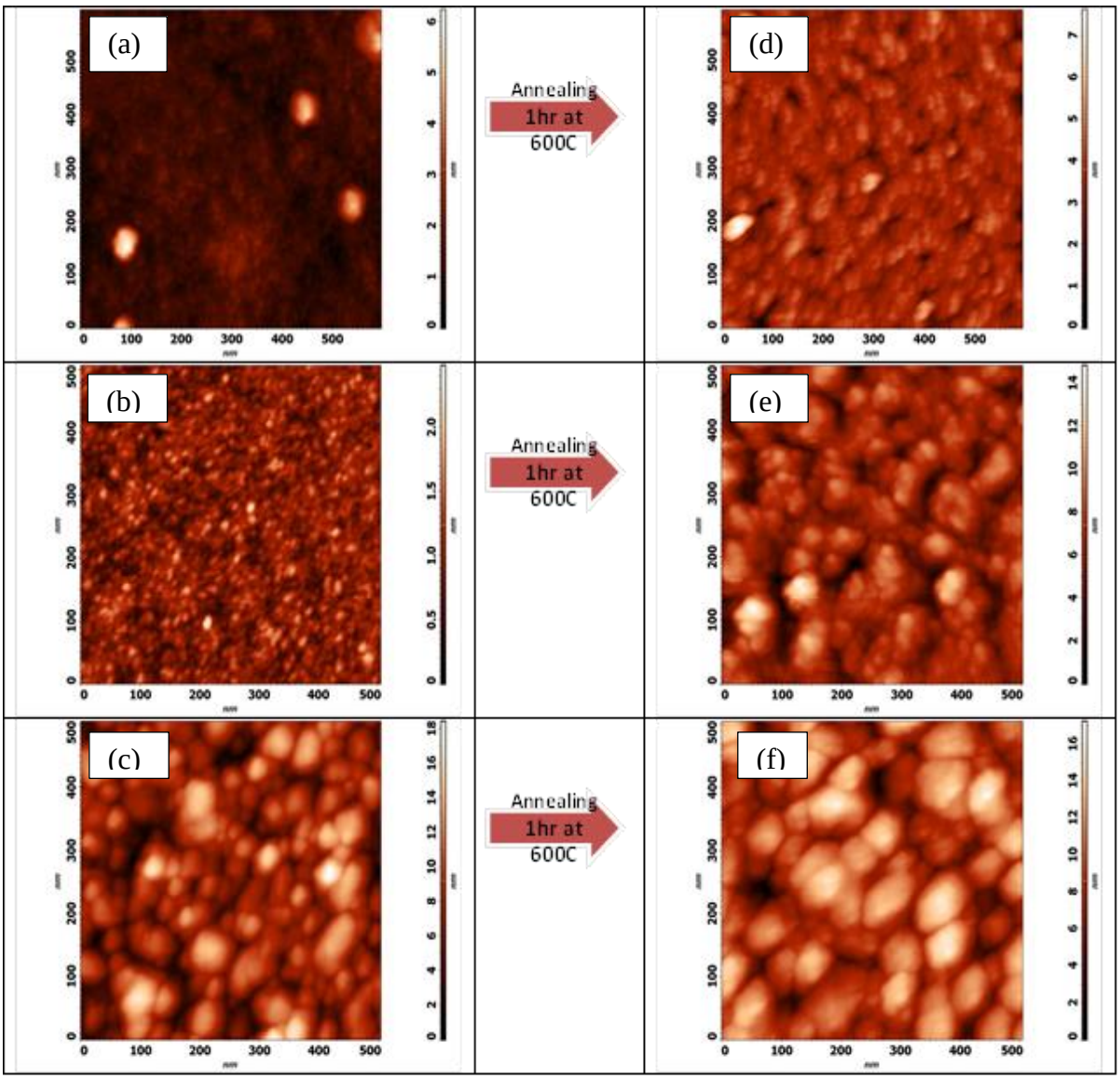

Figure 6.3. Samples topography a) deposited at N_2, b)-RT, c)-600 C, and after annealing: d), e) and f).

Table 6.1

Particle height measurement

Sample	1μm		500nm		1μm		500nm	
	Particles Height (nm)	St. Dev.	Particles Height (nm)	St. Dev.	Particles Diameter (nm)	St. Dev.	Particles Diameter (nm)	St. Dev.
37-N2	2.382	1.514	1.471	0.465	49	17.1	38.6	12.1
37-N2 after annealing	6.553	0.438	3.789	0.39	22.5	10.3	23.8	7.5
32-RT	1.489	0.294	1.41	0.21	15.4	5.9	12.9	5.1
32-RT after annealing	17.275	9.201	7.25	1.065	51.4	23.6	46.2	18.4
35-600°C	18.676	3.152	9.046	1.951	72.5	19.8	59.7	18.4
35-600°C after annealing	18.071	2.842	9.979	1.866	82.3	18.5	71.6	23.3

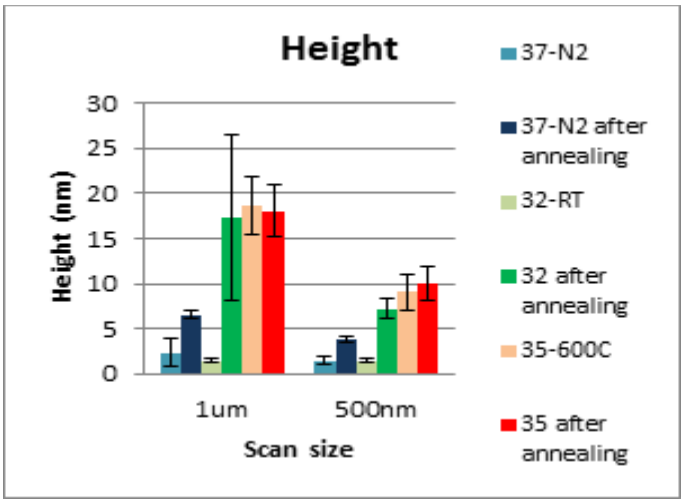

Figure 6.4. AFM measured values of particle height at 1 µm and 500 nm scan sizes

6.3 Magnetic Results

The M-H curves of the as-deposited films obtained by PPMS are shown in Figure 6.5 (a), 6.6 (a) and 6.6 (a). The narrow loops and low coercivities are the known properties of soft magnetic materials. The coercivity of sample 35 deposited at 600˚C is 44.76 Oe almost as twice as that of sample 32 deposited at room temperature which is found to be 25.86 Oe, this higher coercivity is due to the decreased number of defects on higher deposition temperatures and the thermal stability of the films also shown on the AFM results of the stable surface morphology after post annealing for this sample. Sample 35 also show formation of crystal structures. For high deposition temperature the substrate surface have high energy as well as the deposited particles which bounce back when it come into contact with the surface allowing for the formation of a very small numbers of seeds to adhere to substrates and eventually the particles mobility allow them to create large crystals at these seeds. Sample 37 deposited at liquid N_2 temperature is the most interesting since its hysteresis loop show superparamagnetic behavior. The nature of this deposition allows for the quick adhesion of very fine particles which explain the behavior of the hysteresis loop. The M-H curves for the post annealed films are shown in

Figure 6.5 (b), 6.6 (b) and 6.7 (b). The coercivities are increased significantly post annealing. Coercivity of sample 32 post annealing increased from 25.86Oe to 173.54Oe at 10K which is a 571% increase. This is mostly due to the formation of crystal like structures on the sample. Sample 35 post annealing coercivity increased from 44.76Oe to 208.79Oe at 10K which is an increase of 4 %; this assumed to be caused by a sort of adjustment of the crystal orientation. Sample 37 as deposited magnet behavior changed from superparamagnetic to ferromagnetic exhibiting a hard magnetic material wide hysteresis loop.

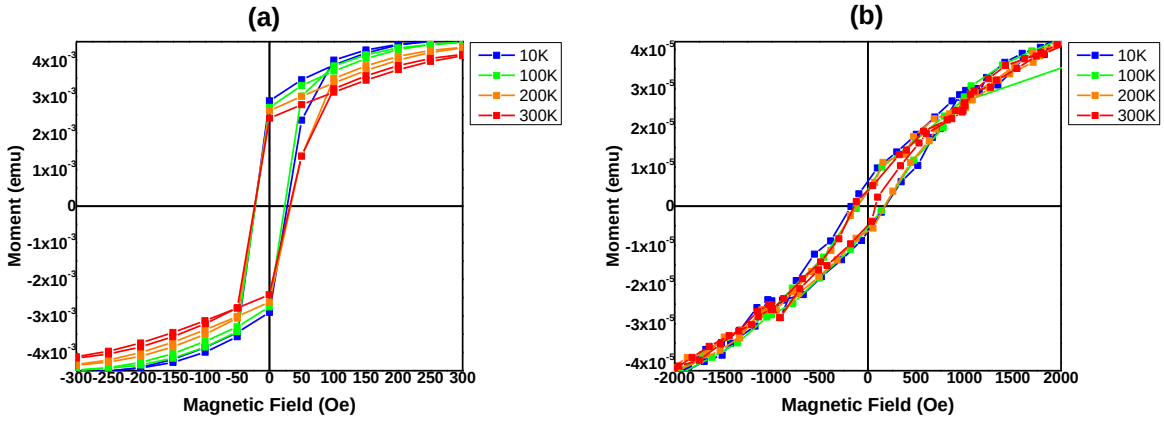

Figure 6.5. Hysteresis loops a) as deposited at room temperature, and b) after annealed.

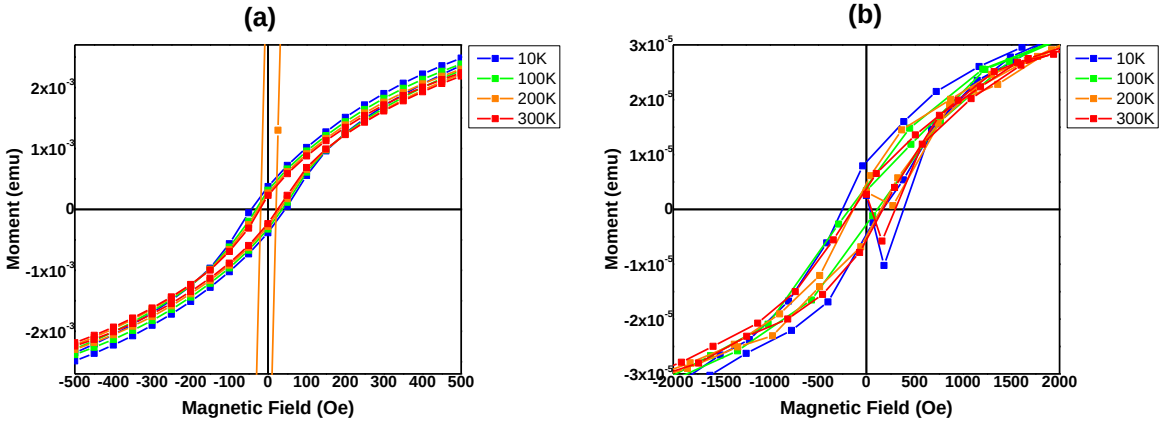

Figure 6.6. Hysteresis loops a) as deposited at 600˚C, and b) after annealed.

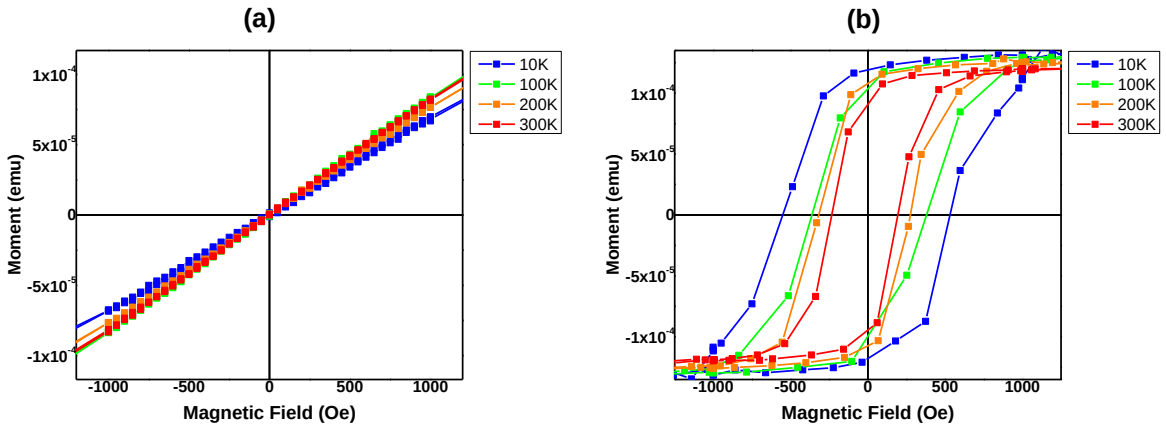

Figure 6.7. Hysteresis loops a) as deposited at liquid N_2 temperature, and b) after annealed.

This change indicates formation of an $L1_0$ structure of the FeNi. The $L1_0$ FeNi has high coercivities in the range of 500Oe to 3KOe [69] because of its high uniaxial magnetic anisotropy and good thermal stability of magnetization. Figure 6.8 shows the significant increase in the coercivities of the as deposited films and post annealed films.

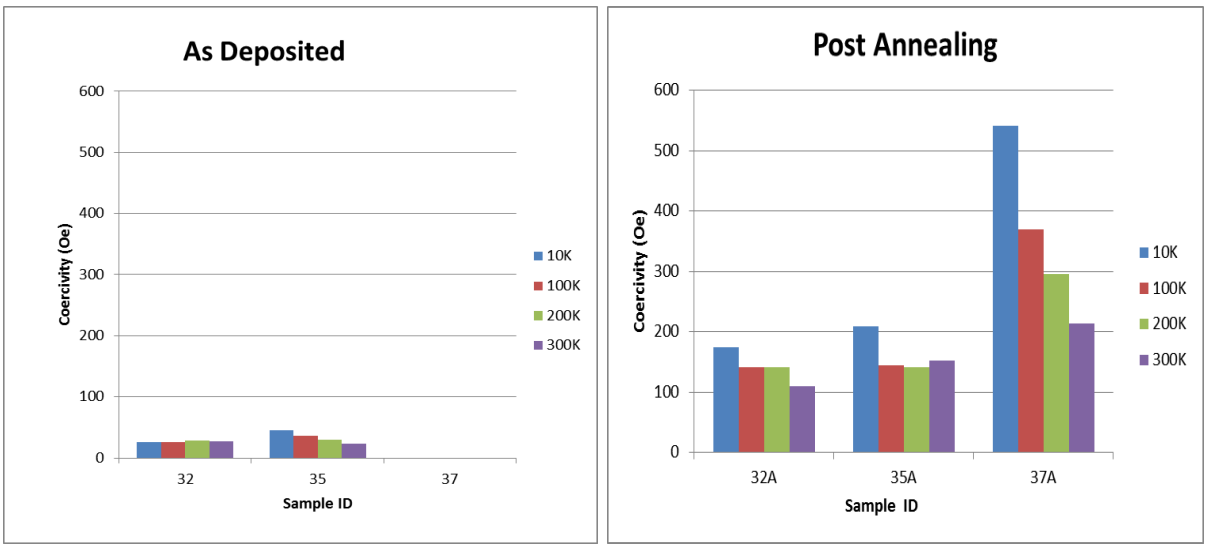

Figure 6.8. Coercivity comparison of the (a) as deposited and (b) post annealed films at measurement temperatures of 10K, 100K, 200K and 300K.

CHAPTER 7

Conclusions and Future Work

This dissertation reports a detailed study on the magnetic and structural properties of FeNi thin films. Pulsed laser deposition method has been used for the first time to fabricate FeNi thin films with $L1_0$ phase. Due to high anisotropy of $L1_0$ structure, which in turn arises due to its twelve different magnetic orientations of $L1_0$ structure, FeNi can efficiently be used in recording media in data storage devices. Since $L1_0$ structure exists only with 50-50 composition of the constituent elements, $Fe_{50}Ni_{50}$ was the sole composition of the research carried out under this dissertation work. However, $Fe_{50}Ni_{50}$ thin films were deposited in three different ways: FeNi thin films fabrication using a composite target, FeNi thin films fabrication using sequential ablation of Fe and Ni targets, FeNi in nano-particulate form embedded in Al_2O_3. Many samples of each category were deposited at a very wide range of temperatures (from -196 ºC to 600˚C).

The microstructural studies of FeNi films have revealed that films deposited at elevated temperatures exhibited much more uniform grain distribution than films deposited at lower temperatures. The magnetic properties of FeNi nanoparticles in AL_2O_3 thin film matrix were found to be inferior to the magnetic properties of FeNi thin films. This is attributed to lack of $L1_0$ phase in FeNi nanoparticles, which is caused by amorphous alumina layer that prevented the growth of FeNi materials in crystalline form. In the second part of the research, a gold layer was used as a catalyst to promote the crystalline growth of $L1_0$ FeNi thin films. Gold films which convert to nano-dots after heating at elevated temperatures have been found to yield FeNi films with very uniform grain size distribution.

Finally, a post deposition heat treatment were carried out on $Fe_{50}Ni_{50}$ thin films deposited at temperature close to the boiling temperature of liquid N_2, room temperature, and 600°C. To

perform post deposition heat treatment, the FeNi samples were heated in the deposition chamber at 600°C for 1 hour. Surface roughness obtained by AFM has shown that annealing increased the surface roughness of the samples deposited at RT and Liquid N_2, but not for the samples deposited at 600 ºC. Results acquired from the magnetization versus field hysteresis loops have shown that post annealing had a significant effect on magnetic properties. The film deposited at Liquid Nitrogen temperature exhibited perfect superparamagnetic behavior, indicating very small particles of the order 1-2 nm. Post annealing changed this to a hard ferromagnetic behavior. The hysteresis loop of the annealed liquid N_2 sample is a wide square loop indicating the presence of an $L1_0$ ordered structure in the film. The presence of $L1_0$ phase is also manifested with realization of higher values of coercivity. The realization of higher values of coercivity is in accordance with Stoner-Wohlfarth model which suggests that the reversal of magnetic spins occur by in-phase rotation of all moments.

7.1 Future Work

In this section, some recommendations for future work are presented. Since substrate texture influences the grain distribution of thin films, it would be interesting to use different materials such as $LaAlO_3$, and $SrTiO_3$, and see their effect on the formation of $L1_0$ phase and associated magnetic properties. In this work, gold was employed as catalyst to promote $L1_0$ structure growth. Another good catalyst known to improve the $L1_0$ growth is CuAu which would obviously be much cheaper than pure gold. Since FeNi deposited at temperatures in the vicinity at liquid nitrogen temperature shows perfect superparamagnetic behavior making them suitable for biomedical applications, efforts could be made in the direction of fabricating some actual prototype biomedical devices. A more detailed study is needed to optimize the annealing

temperature and duration to produce FeNi ordered films with exclusive $L1_0$ phase. Reflection high energy electron diffraction (RHEED) is important when catalyst layers are embedded to help observe the epitaxial growth of subsequent layers. Transmission electron microscopy should be employed as a more definitive method to verify the existence of the $L1_0$ structure.

References

1. Eleftheriou, E., et al. *A nanotechnology-based approach to data storage*. in *Proceedings of the 29th international conference on Very large data bases-Volume 29*. 2003. VLDB Endowment.
2. contributors, W., *Data storage device* Wikipedia, The Free Encyclopedia. p. 608665753
3. Jorgensen, F., *The complete handbook of magnetic recording*. 1988: Tab Books.
4. Frey, N.A. and S. Sun, *Magnetic Nanoparticle for Information Storage Applications.* Inorganic Materials, 2010: p. 33-68.
5. Prasad, S.a.P., S. N., *Developments in Data Storage: Materials Perspective* (2011), Hoboken, NJ, USA: John Wiley & Sons, Inc.
6. Torrejón, J., G. Badini-Confalonieri, and M. Vázquez, *Fabrication and magnetic properties of hard/soft magnetostatically coupled FePt/ FeNi multilayer microwires.* Journal of Applied Physics, 2008. **103**(7): p. 07E712.
7. Guo, H., et al., *L10-FePt based exchange coupled composite films with soft [Co/Ni] N multilayers.* Journal of Applied Physics, 2012. **111**(10): p. 103916.
8. Goll, D., et al., *Experimental realization of graded L10-FePt/Fe composite media with perpendicular magnetization.* Journal of Applied Physics, 2008. **104**(8): p. 083903.
9. Lyubina, J., et al., *Structure and magnetic properties of L10-ordered Fe–Pt alloys and nanoparticles.* Handbook of magnetic materials, 2011. **19**: p. 291-395.
10. Ristau, R., et al., *On the relationship of high coercivity and L10 ordered phase in CoPt and FePt thin films.* Journal of applied physics, 1999. **86**(8): p. 4527-4533.
11. Laughlin, D.E., et al., *Crystallographic aspects of L1< sub> 0</sub> magnetic materials.* Scripta materialia, 2005. **53**(4): p. 383-388.

12. De Graef, M. and M.E. McHenry, *Structure of Materials: An Introduction to Crystallography, Diffraction and Symmetry*. 2007: Cambridge University Press.

13. William D. Callister, D.G.R., *Materials Science and Engineering: An Introduction*. 8th Edition ed. 2009: John Wiley & Sons, Inc.

14. Lenz, J. and A.S. Edelstein, *Magnetic sensors and their applications.* Sensors Journal, IEEE, 2006. **6**(3): p. 631-649.

15. Brauer, J.R., *Magnetic Actuators and Sensors*. Wiley - IEEE Press.

16. Cullity, B.D. and C.D. Graham, *Introduction to magnetic materials*. 2011: John Wiley & Sons.

17. contributors, W. *Magnetism* 17 June 2014 23:06 UTC Available from: http://en.wikipedia.org/w/index.php?title=Magnetism&oldid=613349329.

18. Chrisey, D.B. and G.K. Hubler, *Pulsed laser deposition of thin films*. 1994, New York: J. Wiley.

19. Lowndes, D.H., et al., *Synthesis of novel thin-film materials by pulsed laser deposition.* Science, 1996. **273**(5277): p. 898-903.

20. Caricato, A., et al., *Pulsed laser deposition of magnetic films by ablation of Co-and Fe-based amorphous alloys.* Applied Physics A, 2004. **79**(4-6): p. 1251-1254.

21. Acquaviva, S., et al., *Pulsed laser deposition of Co-and Fe-based amorphous magnetic films and multilayers.* Thin Solid Films, 2003. **433**(1): p. 252-258.

22. Shen, J., Z. Gai, and J. Kirschner, *Growth and magnetism of metallic thin films and multilayers by pulsed-laser deposition.* Surface science reports, 2004. **52**(5): p. 163-218.

23. Williams, C., et al., *The magnetic and structural properties of pulsed laser deposited epitaxial MnZn–ferrite films.* Journal of applied physics, 1994. **75**(3): p. 1676-1680.

24. Mozhaev, P., et al., *Comparison of high-pressure dc-sputtering and pulsed laser deposition of superconducting YBa2Cu3O x thin films.* Journal of superconductivity, 1997. **10**(3): p. 221-226.

25. Collier, C.P., et al., *Molecular-based electronically switchable tunnel junction devices.* Journal of the American Chemical Society, 2001. **123**(50): p. 12632-12641.

26. Cui, T., F. Hua, and Y. Lvov, *FET fabricated by layer-by-layer nanoassembly.* Electron Devices, IEEE Transactions on, 2004. **51**(3): p. 503-506.

27. Kumar, D., et al., *High coercivity and superparamagnetic behavior of nanocrystalline iron particles in alumina matrix.* Journal of magnetism and magnetic materials, 2001. **232**(3): p. 161-167.

28. Zhao, F., et al., *Formation of monodisperse FePt alloy nanocrystals using air-stable precursors: fatty acids as alloying mediator and reductant for Fe3+ precursors.* Journal of the American Chemical Society, 2009. **131**(14): p. 5350-5358.

29. Carpenter, E., et al., *Magnetic properties of iron and iron platinum alloys synthesized via microemulsion techniques.* Journal of Applied Physics, 2000. **87**(9): p. 5615-5617.

30. Momose, S., et al., *Fine tuning of the sizes of FePt nanoparticles.* Japanese journal of applied physics, 2005. **44**(2R): p. 1147.

31. Srivastava, C., D.E. Nikles, and G.B. Thompson, *Compositional evolution during the synthesis of FePt nanoparticles.* Journal of Applied Physics, 2008. **104**(6): p. 064315.

32. Sun, S., et al., *Monodisperse FePt nanoparticles and ferromagnetic FePt nanocrystal superlattices.* Science, 2000. **287**(5460): p. 1989-1992.

33. Hannemann, U., et al., *Intrinsic and extrinsic properties of epitaxial Nd 2 Fe 14 B films.* Applied physics letters, 2003. **82**(21): p. 3710-3712.

34. Cadieu, F., T. Cheung, and L. Wickramasekara, *Magnetic properties of sputtered Nd-Fe-B films.* Journal of magnetism and magnetic materials, 1986. **54**: p. 535-536.

35. Leslie-Pelecky, D.L. and R.D. Rieke, *Magnetic properties of nanostructured materials.* Chemistry of materials, 1996. **8**(8): p. 1770-1783.

36. Bonder, M.J., Y. Huang, and G.C. Hadjipanayis, *Magnetic Nanoparticles*. 2006, Springer US: Boston, MA. p. 183-206.

37. Rowlands, G., *The variation of coercivity with particle size.* Journal of Physics D: Applied Physics, 1976. **9**: p. 1267.

38. Lin, X., et al., *Temperature dependence of morphology and magnetic properties of cobalt nanoparticles prepared by an inverse micelle technique.* Langmuir, 1998. **14**(25): p. 7140-7146.

39. Rivoirard, S. and D. Givord, *Hard-Magnetic Nanostructures*, in *Advanced Magnetic Nanostructures*. 2006, Springer. p. 325-363.

40. Stoner, E.C. and E. Wohlfarth, *A mechanism of magnetic hysteresis in heterogeneous alloys.* Philosophical Transactions of the Royal Society of London. Series A. Mathematical and Physical Sciences, 1948: p. 599-642.

41. Chen, S.-C., et al., *Granular FePt–Ag thin films with uniform FePt particle size for high-density magnetic recording.* Materials Science and Engineering: B, 2002. **88**(1): p. 91-97.

42. Christodoulides, J., et al., *CoPt and FePt thin films for high density recording media.* Journal of Applied Physics, 2000. **87**(9): p. 6938-6940.

43. Daniil, M., et al., *FePt/BN granular films for high-density recording media.* Journal of magnetism and magnetic materials, 2002. **246**(1): p. 297-302.

44. Luo, C. and D. Sellmyer, *Structural and magnetic properties of FePt: SiO 2 granular thin films.* Applied physics letters, 1999. **75**(20): p. 3162-3164.

45. Kuo, C.-M. and P. Kuo, *Magnetic properties and microstructure of FePt–Si 3 N 4 nanocomposite thin films.* Journal of Applied Physics, 2000. **87**(1): p. 419-426.

46. Shima, T., et al., *Preparation and magnetic properties of highly coercive FePt films.* Applied physics letters, 2002. **81**(6): p. 1050-1052.

47. Weisheit, M., L. Schultz, and S. Fähler, *On the influence of composition on laser-deposited Fe–Pt films.* Journal of magnetism and magnetic materials, 2005. **290**: p. 570-572.

48. Stoyanov, S., et al., *Fabrication of ordered FePt nanoparticles with a cluster gun.* Journal of applied physics, 2003. **93**(10): p. 7190-7192.

49. Bao, Y., et al., *Controlled crystalline structure and surface stability of cobalt nanocrystals.* The Journal of Physical Chemistry B, 2005. **109**(15): p. 7220-7222.

50. Stavroyiannis, S., et al., *CoPt/Ag nanocomposites for high density recording media.* Applied physics letters, 1998. **73**(23): p. 3453-3455.

51. Wood, R., *The feasibility of magnetic recording at 1 terabit per square inch.* Magnetics, IEEE Transactions on, 2000. **36**(1): p. 36-42.

52. Yu, M., et al., *Nanocomposite CoPt: C films for extremely high-density recording.* Applied Physics Letters, 1999. **75**(25): p. 3992-3994.

53. Bian, B., et al., *Ordering of island-like FePt crystallites with orientations.* Applied Physics Letters, 1999. **75**(23): p. 3686-3688.

54. Zhang, B. and W. Soffa, *Structure and properties of rapidly-solidified iron-platinum and iron-palladium alloys.* Magnetics, IEEE Transactions on, 1990. **26**(5): p. 1388-1390.

55. Xu, Y., et al., *Magnetic properties of L10 FePt and FePt: Ag nanocluster films.* Journal of applied physics, 2003. **93**(10): p. 8289-8291.

56. Xu, Y., et al., *Preparation and magnetic properties of CoPt and CoPt: Ag nanocluster films.* Journal of magnetism and magnetic materials, 2003. **266**(1): p. 164-170.

57. Xu, Y., M. Yan, and D.J. Sellmyer, *Cluster-assembled nanocomposites*, in *Advanced magnetic nanostructures*. 2006, Springer. p. 207-238.

58. Shima, T., et al., *Structure and magnetic properties for L1< sub> 0</sub>-ordered FeNi films prepared by alternate monatomic layer deposition.* Journal of Magnetism and Magnetic Materials, 2007. **310**(2): p. 2213-2214.

59. Mizuguchi, M., S. Sekiya, and K. Takanashi, *Characterization of Cu buffer layers for growth of L1 0-FeNi thin films.* Journal of Applied Physics, 2010. **107**(9): p. 09A716-09A716-3.

60. Scorzelli, R. and J. Danon, *Mössbauer Spectroscopy and X-Ray Diffraction Studies of Fe-Ni Order-Disorder Processes in a 35% Ni Meteorite (Santa Catharina).* Physica Scripta, 1985. **32**(2): p. 143.

61. Takanashi, K., et al., *Artificial fabrication of an L10-type ordered FeAu alloy by alternate monatomic deposition.* Applied physics letters, 1995. **67**(7): p. 1016-1018.

62. Gehanno, V., et al., *Magnetic domains in epitaxial ordered FePd (001) thin films with perpendicular magnetic anisotropy.* Physical Review B, 1997. **55**(18): p. 12552.

63. Dynna, M., et al., *On the nature of L1< sub> 0</sub> ordering in equiatomic AuNi and AuCu thin films grown on Au (001).* Acta materialia, 1997. **45**(1): p. 257-272.

64. Shima, T., et al., *Low-temperature fabrication of L10 ordered FePt alloy by alternate monatomic layer deposition.* Applied physics letters, 2002. **80**(2): p. 288-290.

65. Néel, L., et al., *Magnetic Properties of an Iron—Nickel Single Crystal Ordered by Neutron Bombardment.* Journal of Applied Physics, 1964. **35**(3): p. 873-876.

66. Paulevé, J., et al., *Magnetization Curves of Fe–Ni (50–50) Single Crystals Ordered by Neutron Irradiation with an Applied Magnetic Field.* Journal of Applied Physics, 1968. **39**(2): p. 989-990.

67. Kojima, T., et al., *Fe–Ni composition dependence of magnetic anisotropy in artificially fabricated L1 0-ordered FeNi films.* Journal of Physics: Condensed Matter, 2014. **26**(6): p. 064207.

68. Kojima, T., M. Mizuguchi, and K. Takanashi. *L10-ordered FeNi film grown on Cu-Ni binary buffer layer*. in *Journal of Physics: Conference Series*. 2011. IOP Publishing.

69. Kotsugi, M., et al., *Structural, magnetic and electronic state characterization of L1 0-type ordered FeNi alloy extracted from a natural meteorite.* Journal of Physics: Condensed Matter, 2014. **26**(6): p. 064206.

70. Albertsen, J., J. Knudsen, and G. Jensen, *Structure of taenite in two iron meteorites.* Nature, 1978. **273**: p. 453.

71. Clarke, R.S. and E.R. Scott, *Tetrataenite; ordered FeNi, a new mineral in meteorites.* American Mineralogist, 1980. **65**(7-8): p. 624-630.

72. Chikazumi, S., et al., *Handbook of Magnetic Materials.* Asakura Shoten, Tokyo, 1975. **341**.

73. Anisimov, S., D. Bäuerle, and B. Luk'Yanchuk, *Gas dynamics and film profiles in pulsed-laser deposition of materials.* Physical Review B, 1993. **48**(16): p. 12076.

74. Kumar, N., et al. *Dynamics of plasma expansion in the pulsed laser material interaction*. in *Sadhana (Academy Proceedings in Engineering Sciences)*. 2010. Indian Academy of Sciences.

75. Ho, J., C. Grigoropoulos, and J. Humphrey, *Computational study of heat transfer and gas dynamics in the pulsed laser evaporation of metals.* Journal of Applied Physics, 1995. **78**(7): p. 4696-4709.

76. Eason, R., *Pulsed laser deposition of thin films: applications-led growth of functional materials*. 2007, Hoboken, N.J: Wiley-Interscience.

77. Smith, D.L., *Thin-film deposition: principles and practice*. 1995, New York: McGraw-Hill.

78. Quate, C. and C. Gerber, *Atomic Force Microscopy.* 1986.

79. Amer, N.M. and G. Meyer, *Atomic force microscopy*. 1992, Google Patents.

80. Binnig, G., C.F. Quate, and C. Gerber, *Atomic force microscope.* Physical review letters, 1986. **56**(9): p. 930.

81. Blanchard, C.R., *Atomic force microscopy.* The chemical educator, 1996. **1**(5): p. 1-8.

82. Ryland, A.L., *X-ray diffraction.* Journal of Chemical Education, 1958. **35**(2): p. 80.

83. Warren, B.E., *X-ray Diffraction*. 1969: Courier Dover Publications.

84. Guinier, A., *X-ray diffraction: in crystals, imperfect crystals, and amorphous bodies*. 2013: Courier Dover Publications.

85. Pecharsky, V. and P. Zavalij, *Fundamentals of powder diffraction and structural characterization of materials*. 2008: Springer.

86. Reichelt, R., *Scanning Electron Microscopy*. 2007, Springer New York: New York, NY. p. 133-272.

87. Ohring, M., *The materials science of thin films*. 1992, Boston: Academic Press.

88. Kearsley, A., *KRINSLEY, D. H., PYE, K., BOGGS, S., JR & TOVEY, N. K. 1998. Backscattered Scanning Electron Microscopy and Image Analysis of Sediments and Sedimentary Rocks. ix+193 pp. Cambridge, New York, Melbourne: Cambridge University Press. Price £50.00, US $80.00 (hard covers). ISBN 0 521 45346 1.* Geological Magazine, 2001. **138**(4): p. 499-508.

89. Goldstein, J., et al., *Scanning electron microscopy and X-ray microanalysis*. 2003: Springer.

90. Chrisey, D.B. and G.K. Hubler, *Pulsed laser deposition of thin films.* Pulsed Laser Deposition of Thin Films, by Douglas B. Chrisey (Editor), Graham K. Hubler (Editor), pp. 648. ISBN 0-471-59218-8. Wiley-VCH, May 2003., 2003. **1**.

Appendix A

Pattern : 00-004-0850 ***Radiation =*** 1.540598 ***Quality :*** High

Ni

Nickel
Nickel, syn

Lattice : Face-centered cubic
S.G. : Fm-3m (225)

a = 3.52380

Z = 4

Mol. weight = 58.70
Volume [CD] = 43.76
Dx = 8.911

Color: White
Sample source or locality: Sample obtained from Johnson Matthey Company, Ltd.
Analysis: Spectrographic analysis show <0.01% each of Mg, Si and Ca.
Temperature of data collection: Pattern taken at 26 C.
Additional pattern: See ICSD 64989 (PDF 01-087-0712).
Data collection flag: Ambient.

Swanson, Tatge., Natl. Bur. Stand. (U.S.), Circ. 539, volume I, page 13 (1953)

CAS Number: 7440-02-0

Radiation : CuKa1
Lambda : 1.54050
SS/FOM : F8= 88(0.0114,8)

Filter : Beta
d-sp : Not given

2th	*i*	*h*	*k*	*l*
44.508	100	1	1	1
51.847	42	2	0	0
76.372	21	2	2	0
92.947	20	3	1	1
98.449	7	2	2	2
121.935	4	4	0	0
144.678	14	3	3	1
155.666	15	4	2	0

Pattern : 03-065-5131 ***Radiation =*** 1.540598 ***Quality :*** Calculated

Fe_3Ni_2

Iron Nickel

Lattice : Face-centered cubic

S.G. : Fm-3m (225)

a = 3.59800

Mol. weight = 284.94

Volume [CD] = 46.58

Dx = 8.127

I/Icor = 7.71

NIST M&A collection code: L 28729 14387 0
Temperature factor: TF was not given, B set to 1.000 for calc.
Sample preparation: Ni(x)Fe(1-x) films with various compositions were vacuum deposited onto quartz-crystal substrates at room temperature by electron beam evaporating pellets of bulk Ni(y)Fe(1-y) alloys.
Remarks from ICSD/CSD: thin films; unit cell dimension taken from figure.
Data collection flag: Ambient.

Dumpich, G., Wassermann, E. F., Manns, V., Keune, W., Murayama, S., Miyako, Y., J. Magn. Magn. Mater., volume 67, page 55 (1987)
Calculated from NIST using POWD-12++

Radiation : CuKa1

Lambda : 1.54060

SS/FOM : F8=1000(0.0004,8)

Filter : Not specified

d-sp : Calculated spacings

2th	*i*	*h*	*k*	*l*
43.532	999	1	1	1
50.704	420	2	0	0
74.535	170	2	2	0
90.479	157	3	1	1
95.742	43	2	2	2
117.821	19	4	0	0
137.879	60	3	3	1
146.449	58	4	2	0

Pattern : 00-006-0696 ***Radiation =*** 1.540598 ***Quality :*** High

Fe

Iron
Iron, syn
Also called: ferrite, bainite, ledkunite

Lattice : Body-centered cubic
S.G. : Im-3m (229)

a = 2.86640
Z = 2

Mol. weight = 55.85
Volume [CD] = 23.55
Dx = 7.875

Color: Gray, light gray metallic
General comments: Total impurities of sample <0.0013% each metals and non-metals.
Additional pattern: See ICSD 64795 (PDF 01-085-1410).
Temperature of data collection: Pattern taken at 25 C.
Sample preparation: The iron used was an exceptionally pure rolled sheet prepared at the NBS, Gaithersburg, Maryland, USA., [Moore, G., *J. Met.*, **5** 1443 (1953)]. It was annealed in an H2 atmosphere for 3 days at 1100 C and slowly cooled in a He atmosphere.
General comments: γ-Fe (fcc)=(1390 C) δ-Fe (bcc).
General comments: Opaque mineral optical data on specimen from Meteorite: RR_2R_e= 57.7, Disp.=16, VHN=158 (mean at 100, 200, 300), Color values=.311, .316, 57.9, Ref.: IMA Commisssion on Ore Microscopy QDF.
Data collection flag: Ambient.

Swanson et al., Natl. Bur. Stand. (U.S.), Circ. 539, volume IV, page 3 (1955)

CAS Number: 7439-89-6

Radiation : CuKa1
Lambda : 1.54050
SS/FOM : F6=222(0.0045,6)

Filter : Beta
d-sp : Not given

2th	*i*	*h*	*k*	*l*
44.674	100	1	1	0
65.023	20	2	0	0
82.335	30	2	1	1
98.948	10	2	2	0
116.390	12	3	1	0
137.143	6	2	2	2

Pattern : 00-037-0474 ***Radiation =*** 1.540598 ***Quality :*** High

(Fe,Ni)

Iron Nickel
Kamacite

Lattice : Body-centered cubic
S.G. : Im-3m (229)

a = 2.86810

Z = 2

Mol. weight = 56.02
Volume [CD] = 23.59
Dx = 7.885

Sample source or locality: Specimen from Hexahedrite meteorite, Bennet County, South Dakota, USA.
Color: Gray metallic
Analysis: Analysis: Fe0.938 Ni0.056 Co0.004.
Additional pattern: To replace 00-018-0645.
Data collection flag: Ambient.

Keller, L., Rask, J., Buseck, P., Arizona State University, Tempe, Arizona, USA., ICDD Grant-in-Aid (1986)

Radiation : CuKa
Lambda : 1.54178
SS/FOM : F6=111(0.0090,6)

Filter : Monochromator crystal
d-sp : Diffractometer
Internal standard : Si

2th	*i*	*h*	*k*	*l*
44.647	100	1	1	0
64.982	12	2	0	0
82.284	18	2	1	1
98.882	5	2	2	0
116.267	5	3	1	0
137.002	7	2	2	2

Pattern : 03-065-3244 ***Radiation =*** 1.540598 ***Quality :*** Calculated

$FeNi_3$

Iron Nickel

Lattice : Cubic
S.G. : Pm-3m (221)

a = 3.55230

Z = 1

Mol. weight = 231.95
Volume [CD] = 44.83
Dx = 8.592
I/Icor = 7.99

NIST M&A collection code: N AL4443 4140
Temperature factor: IB=Fe,Ni
Data collection flag: Ambient.

R.J.Wakelin & E.L.Yates, Proc. Phys. Soc., London, Sect. B, volume B66, page 221 (1953)
Calculated from NIST using POWD-12++

Radiation : CuKa1
Lambda : 1.54060
SS/FOM : F17=1000(0.0003,17)

Filter : Not specified
d-sp : Calculated spacings

2th	*i*	*h*	*k*	*l*
25.048	4	1	0	0
35.717	4	1	1	0
44.121	999	1	1	1
51.404	426	2	0	0
58.009	2	2	1	0
64.168	2	2	1	1
75.661	182	2	2	0
81.164	1	2	2	1
86.585	1	3	1	0
91.976	173	3	1	1
97.384	48	2	2	2
102.860	1	3	2	0
108.458	1	3	2	1
120.311	23	4	0	0
126.780	1	4	1	0
133.851	1	4	1	1
141.890	77	3	3	1

Pattern : 00-004-0784 ***Radiation =*** 1.540598 ***Quality :*** High

Au

Gold
Gold, syn

Lattice : Face-centered cubic
S.G. : Fm-3m (225)

a = 4.07860

Z = 4

Mol. weight = 196.97
Volume [CD] = 67.85
Dx = 19.283
Dm = 19.300

Color: Yellow metallic
Melting point: 1061.6-1063.2
Sample source or locality: Sample purified at NBS, Gaithersburg, Maryland, USA and is about 99.997% Au.
Temperature of data collection: Pattern taken at 26 C.
Analysis: Spectrographic analysis (%): Si 0.001, Ca 0.001, Ag 0.001(?).
General comments: Opaque mineral optical data on specimen from unspecified locality: RR_2Re=71.6, Disp.=16, VHN_{100}=53-58, Color values=.384, .391, 72.7, Ref.: IMA Commission on Ore Microscopy QDF.
Optical data: B=0.366
Data collection flag: Ambient.

Swanson, Tatge., Natl. Bur. Stand. (U.S.), Circ. 539, volume I, page 33 (1953)

CAS Number: 7440-57-5

Radiation : CuKa1
Lambda : 1.54056
SS/FOM : F9=129(0.0078,9)

Filter : Beta
d-sp : Not given

2th	*i*	*h*	*k*	*l*
38.185	100	1	1	1
44.393	52	2	0	0
64.578	32	2	2	0
77.549	36	3	1	1
81.724	12	2	2	2
98.137	6	4	0	0
110.802	23	3	3	1
115.264	22	4	2	0
135.422	23	4	2	2

Appendix B

Table B-1

Coercivity of as deposited and annealed samples

Sample #	Composition	Substrate	T (°C)	Coercivity (Oe)			
				10K	100K	200K	300K
32	Fe50Ni50	Si/Sa	25°	25.34	23.1	27.92	28.29
35	Fe50Ni50	Si/Sa	600°	43.83	33.98	20	23.31
37	Fe50Ni50	Si/Sa	-196°	0	0	0	0
32A	Fe50Ni50	Si/Sa	25°	178.74	139.17	146.36	110.53
35A	Fe50Ni50	Si/Sa	600°	207.87	145.10	143.15	154.68
37A	Fe50Ni50	Si/Sa	-196°	542.65	370.38	298.21	216.12
70	Au/Fe50Ni50	Si/Sa	25°	96.46	49.93	74.52	66.1
73	Au/Fe50Ni50	Si/Sa	600°	393.76	260.71	284.49	289.61
74	Au/Fe/Ni	Si/Sa	25°	69.64	48.09	42.09	87.41
75	Au/Fe/Ni	Si/Sa	600°	163.63	18.81	83.14	78.79
70A	Au/Fe50Ni50	Si/Sa	25°	96.46	49.93	74.52	66.1
73A	Au/Fe50Ni50	Si/Sa	600°	393.76	260.71	284.49	289.61
74A	Au/Fe/Ni	Si/Sa	25°	69.64	48.09	42.09	87.41
75A	Au/Fe/Ni	Si/Al_2O_3	600°	163.63	18.81	83.14	78.79

Table B-2

Coercivity of all as deposited samples

Sample #	Composition	Substrate	T (°C)	Coercivity (Oe)			
				10K	100K	200K	300K
32	$Fe_{50}Ni_{50}$	Si/Sa	25°	25.34	23.1	27.92	28.29
35	$Fe_{50}Ni_{50}$	Si/Sa	600°	43.83	33.98	20	23.31
37	$Fe_{50}Ni_{50}$	Si/Sa	-196°	0	0	0	0
47	$Fe_{50}Ni_{50}$	Si/Sa	25°	25.33	23.1	27.92	28.29
48	$Fe_{50}Ni_{50}$	Si/Sa	200°	22.25	21.98	22.88	23.08
49	$Fe_{50}Ni_{50}$	Si/Sa	400°	24.64	24.72	24.62	24.75
50	$Fe_{50}Ni_{50}$	Si/Sa	600°	43.83	33.97	20	23.31
51	$Fe_{50}Ni_{50}$	Si/Sa	-196°	0	0	0	0
52	Fe/Ni	Si/Sa	25°	24.49	24.74	24.94	25.04
53	Fe/Ni	Si/Sa	200°	10.92	23.56	24.80	24.44
54	Fe/Ni	Si/Sa	400°	17.11	18.98	20.33	22.49
55	Fe/Ni	Si/Sa	600°	59.15	51.50	39.19	29.93
56	Fe/Ni	Si/Sa	-196°	24.03	24.56	24.48	24.59
57	$Fe_{50}Ni_{50}$ Al_2O_3	Si/Sa	25°	121.31	14.67	12.47	13.09
58	$Fe_{50}Ni_{50}$ Al_2O_3	Si/Sa	200°	10.69	10.55	18.71	21.43
59	$Fe_{50}Ni_{50}$ Al_2O_3	Si/Sa	400°	220.44	9.19	17.17	16.74
60	$Fe_{50}Ni_{50}$ Al_2O_3	Si/Sa	600°	0	0	0	0
61	$Fe_{50}Ni_{50}$ Al_2O_3	Si/Sa	-196°	0	0	0	0
70	Au/$Fe_{50}Ni_{50}$	Si/Sa	25°	96.46	49.96	74.52	66.1
73	Au/$Fe_{50}Ni_{50}$	Si/Sa	600°	393.76	260.71	284.48	289.6
74	Au/Fe/Ni	Si/Sa	25°	69.64	48.09	42.09	87.40
75	Au/Fe/Ni	Si/Sa	600°	163.63	18.85	83.14	78.79